THÈSE DE DOCTORAT DE L'UNIVERSITÉ PARIS 7

Spécialité :

Astronomie et Astrophysique

Présentée par

Damien CHAPON

Pour obtenir le grade de Docteur ès sciences de l'UNIVERSITÉ PARIS 7

Simulations of binary galaxy mergers
the effect of gas physics on small scales

Soutenue le 28 Novembre 2011

devant le jury composé de :

SIMONA MEI	Présidente du jury
ROMAIN TEYSSIER	Directeur de thèse
JULIEN DEVRIENDT	Rapporteur
GARY MAMON	Examinateur
FRÉDÉRIC BOURNAUD	Examinateur
JÉRÔME PEREZ	Invité

Thanks/Remerciements

Avant tout, un grand merci à Romain Teyssier qui, malgré la distance, m'a soutenu durant ces 3 années de thèse, merci pour tout le temps qu'il a consacré à me transmettre tant son goût pour le numérique que sa passion pour l'astrophysique. Merci pour cette liberté d'action dont j'ai allègrement profité, j'ai conscience de ma chance et du fait que peu de thèses de doctorat ont pu se dérouler dans des conditions aussi "libérales". Merci pour ces invitations à Zürich, même s'il semble qu'il y ait là-bas un bon cadre de vie, j'ignore toujours comment tu t'es habitué à la gastronomie locale.

Un immense merci à Frédéric Bournaud qui, bien qu'il n'ait pu diriger mes travaux de thèse, s'est avéré tout simplement indispensable pendant ma thèse. Merci pour ses conseils, son expertise, sa disponibilité et sa prodigieuse réactivité électronique.

I would like to thank Julien Devriendt and Eric Emsellem for reviewing my work, for their time and patience. Many thanks to the members of the comitee.

Many thanks to Lucio for inviting me in Zürich, for his time and patience and his enthusiasm during our scientific collaboration on the black hole pairing simulations.

I don't forget to thank Oscar Agertz, Allan-Sacha Brun, Avishai Dekel, Clare Dobbs, Richard Klein, Telemachos Mouschovias and Stéphane Colombi, without whom the astrophysical community would be much less funny.

Je tiens à remercier tout particulièrement Thomas, Frédéric, Marie, Neil, Katarina, Florent et Leila: La fine équipe de numériciens qui a été pour moi ces 3 dernières années comme une seconde famille.

Merci à tous les professeurs du module d'astrophysique du Master Modélisation et Simulation: Sacha, Laurène, Stéphane et Edouard qui m'ont incité à venir, au SAP, poursuivre en thèse ces travaux numériques de modélisation de notre univers.

Un très grand merci à Jérome Perez qui m'a initié non seulement à la recherche, mais aussi à l'astrophysique. Merci pour cette passion de l'astrophysique qu'il sait communiquer avec tant d'enthousiasme, merci pour ses encouragements, sa vision lucide et ses conseils avisés.

Je tiens à remercier Marie Gay, Nicolas Pailley pour le support informatique. Même si nous avons tous la tête dans les étoiles au sein du SAP, j'estime que

Marie est un des pilliers de ce service, ne serait-ce que pour son efficacité et sa réactivité face à tous nos problèmes bassement matériels, Marie merci pour tout ! Un grand merci aussi à Dominique Monvoisin, dont la rapidité et l'efficacité avec lesquelles elle nous rend tous service relève du super-pouvoir.

Merci à Sébastien Fromang, Edouard Audit, Jean-Pierre Chièze, Franck Delahaye (quelle régate !), pour leur accueil et la bonne ambiance qui règne au 2e étage du SAP.

Merci surtout à Thomas pour cette incroyable fraction de nos thèses que l'on a consacrée à des geekeries en tous genres, si seulement ~~le colonel~~ Romain savait... Je me console en me disant qu'une partie des ces développements servira à d'autres utilsateurs de `RAMSES` . Merci aussi pour ces inoubliables imitations, pour lesquelles tu as un talent incontestable.

Un grand merci à Mimi aussi qui a été là dans les bons mais aussi les mauvais moments et parce que sans elle, je ne serais peut-être pas allé jusqu'au bout...

Enfin, je tiens surtout à remercier ma maman, qui m'a soutenu pendant toutes mes études et qui caressait depuis tant d'années l'espoir de voir son fils devenir un jour docteur en astrophysique... voilà qui est reglé.

Abstract

Galaxy interactions and mergers are key events in the history of our Universe. Each one of them impacts the fragile equilibrium state of the galaxies, their morphology, their mass and star formation rate in a drastic way. Small scale physical processes play a major role during galaxy mergers: the complex interplay between turbulence, gas instabilities, star formation, magnetic field, stellar feedback, cooling processes, chemistry of the interstellar medium, supermassive black holes, active galactic nuclei and supernovæ explosions leads to high level of complexity and is far from being completely understood. In past numerical studies, the lack of resolution and of a consistent thermodynamical model for a multi-phase turbulent interstellar medium was one of the main caveat of galactic scale simulations.

The aim of this thesis if to study the effect of galaxy collision and mergers on the small scale physical processes by using high-resolution numerical simulations. It will focus on the (in)stability of the gas, the associated burst of star formation and the black hole pairing process occuring during these violent events. The AMR hydrodynamical code `RAMSES` used in this work is described in chapter 3, as well as the additional modules I developed for this specific purpose : galaxy binary merger hydrodynamical setup and ISM thermodynamical models.

In chapter 4, I will present a high-resolution Antennæ galaxy (NGC4038/39) merger simulation. In this numerical study, I showed that the use of 12 pc resolution together with a "pseudo-cooling" thermodynamical model leads to a merger-induced clustered starburst, in fair agreement with the star formation properties in observed galaxies. The star formation burst appears less nuclear and more radially extended than suggested by previous numerical study. What is more, these simulated galaxies show a clear shift between two star formation laws during the interaction, in good agreement with the observed disk versus starburst sequences highlighted by recent observations.

Chapter 5 will focus on the formation of a super-massive black hole binary after an equal-mass galaxy merger. The formation of a 60 pc thick $10^9\ M_\odot$ nuclear disk, properties consistent with observed nuclear regions in ULIRGs, and the rapid ($< 10\ Myr$) sinking of the two black holes in its center confirm previous numerical results obtained with SPH simulations. More robust, my AMR simulation uses a 0.1 pc max. resolution and resolve properly the formation of a front shock and a trailing hydrodynamical wake. The effect of dynamical friction by a gaseous medium on the SMBHs pairing process is resolved down to sub-parsec scales and show very good agreement with analytical predictions. The adopted thermodynamical model makes the dynamical friction inefficient near the center, preventing the black hole binary from hardening further down to the gravitational wave emission regime.

Finally, a new data processing and visualization module called PyMSES I co-developed specifically for the `RAMSES` data structure is introduced in chapter 6.

Résumé

Les interactions et les fusions de galaxies sont des événements clés dans l'histoire de notre Univers. Chacun d'eux affecte notamment la morphologie des galaxies, leur masse et leur taux de formation stellaire de manière drastique. Les processus physique qui interviennent à petite échelle jouent un rôle crucial lors des ces événements violents. Par le passé, le manque de résolution et d'un modèle thermodynamique réaliste pour le gaz du milieu interstellaire constituait le principal défaut des simulations.

Le but de cette thèse est d'étudier l'effet des collisions de galaxies sur les processus physiques à petites échelles par le biais de simulations numériques à haute-résolution. Ces simulations numériques ont été réalisées avec le code AMR hydrodynamique `RAMSES` pour lequel j'ai développé des modules additionnels spécifiques à la modélisation de galaxies en interactions. Tous ces outils seront présentés en détails dans le chapitre 3.

Dans le chapitre 4, je présenterai un modèle numérique reproduisant le système des Antennes (NGC4038/39) dans lequel une résolution spatiale poussée et l'utilisation d'un modèle thermodynamique dit de "pseudo-refroidissement" a mené a une flambée de formation stellaire en amas induite par la fusion des deux galaxies. Les conséquence sont une formation stellaire plus inhomogène, plus efficace et plus radialement étendue que dans de précédentes études à faible résolution. Ces résultats numériques sont en très bon accord avec le scénario de double loi de Kennicutt-Schmidt pour les galaxies isolées/à flambe de formation stellaire mis en évidence par de récentes observations.

Le chapitre 5 se focalisera sur la formation d'un système binaire de trous noirs supermassifs consécutif à la fusion de deux galaxies. La formation d'un disque nucléaire aux propriétés similaires à celles observées dans des ULIRGs, de masse $10^9\ M_\odot$ et de 60 pc d'épaisseur dans lequel la décroissance orbitale des deux trous noirs s'effectue en moins de 10 Ma confirme des résultats numériques obtenues à l'aide de simulations SPH antérieures. Plus robustes, mes simulations AMR ont une résolution de 0.1 pc et résolvent correctement la formation d'une onde de choc frontal ainsi qu'un sursaut hydrodynamique dans le sillage des trous noirs. L'effet de la friction dynamique dûe au gaz sur les trous noirs est correctement résolu jusqu'aux échelles sub-parsec dans cette simulation et sont en excellent accord avec de précédentes prédictions analytiques. Le modèle thermodynamique employé dans cette étude rend la friction dynamique inefficace dans les quelques parsecs centraux, ce qui empêche le système binaire d'atteindre des séparations sous-parsec, régime caractérisé par l'émission d'onde gravitationnelle dans le domaine de détectabilité du satellite LISA.

Enfin, un nouveau module de traitement de données et de visualisation (PyMSES) que j'ai co-développé spécifiquement pour les données de `RAMSES` est présenté dans le chapitre 6.

Contents

List of Figures

List of Tables

Introduction

In the last two decades, the complexity and accuracy of the astrophysical codes have flourished and numerical simulations have become the third major approach in astrophysics. Being the closest equivalents of controlled experiments, simulations are complementary to theory and observations. They were initially limited to simple N-body calculations containing hundreds of particles, but nowadays, recent cosmological simulations of structure formation have taken advantage of the more and more powerful and accessible computational power and are in fair agreement with large scale structure surveys, strengthening the ΛCDM paradigm.

At galactic scales, astrophysicists still struggle to explain a lot of aspects of galaxy formation and evolution. The complex interplay between turbulence, gas instabilities, star formation, magnetic field, stellar feedback, cooling processes, chemistry of the interstellar medium, supermassive black holes and supernovæ explosions leads to high level of complexity for which the power of analytical studies is limited. Galaxy interactions and mergers are thought to be the key events in any galaxy history, perturbing these systems in a fragile equilibrium state, impacting their morphology, their mass and their star formation rate. The lack of resolution and of a consistent thermodynamical model for a multi-phase turbulent interstellar medium is one of the main issue of galactic scale numerical simulations.

The aim of this thesis if to study the effect of galaxy collision and mergers on the small scale physical processes by using high-resolution numerical simulations. It will focus on the (in)stability of the gas, the associated burst of star formation and the black hole pairing process occuring during these violent events. In chapter 1, we will briefly introduce the cosmological context of galaxy interaction and evolution. In chapter 2, the galaxy content, the major processes of galactic dynamics and galaxy interactions will be reviewed. The AMR hydrodynamical code `RAMSES` used in this work will be described in chapter 3, as well as the additional modules developed in the course of this PhD work for the specific purpose of galaxy merger simulations. In chapter 4, we will present some results on the impact of a galaxy merger on the gas fragmentation and associated star formation, based on a high-resolution Antennæ galaxy (NGC4038/39) merger simulation. Chapter 5 will focus on the formation of a super-massive black hole binary at the center of a nuclear disk resulting from an equal-mass galaxy merger simulation. Finally, a new data processing and visualization module called PyMSES designed specifically for the `RAMSES` data structure will be introduced in chapter 6.

Chapter 1

Cosmological context of galaxy formation

In this chapter, we will present the cosmological context of galaxy formation and evolution. The standard cosmological model, the hierarchical scenario of structure growth and the formation of first stars and galaxies will be presented. We will also discuss the main processes of galaxy mass growth: gas accretion and galaxy mergers.

1.1 Content of our universe

The current concordance cosmological model (the ΛCDM paradigm) accounts for the relative abundances of the constituting ingredients of our universe. Constrained by Cosmic Microwave Background (CMB) observations, large scale structures surveys and "standard candles" Type Ia supernovæ distance measurements, it indicates that our universe is made of:

Dark energy whose precise nature and even properties remain unknown to this day, dominates the energy budget of the universe (73.5%). The behavior of this mysterious energy is the same as a constant density and negative pressure fluid. Acting like a cosmological constant Λ in the Friedmann equation, dark energy is believed to be responsible for the recent acceleration of the universe expansion, as suggested by recent observations of Type Ia supernovæ explosions (Riess et al., 1998; Perlmutter et al., 1999, Physics Nobel Prize 2011 !).

Cold Dark matter is the dominant matter component in our universe. Zwicky (1933) first measured missing gravitational mass in the Coma galaxy cluster by measuring velocity dispersions of the galaxies. Another solid evidence of "unseen" mass is the flatness of the rotation curve of observed galaxies that can't be explained by the visible mass of the galaxies alone (Rubin et al., 1978). This invisible matter component, called *dark matter*, accounts for about 83% of the gravitational mass of the universe, 22% of its energy budget and is believed to interact almost only gravitationally with traditional matter. Although its nature is still unknown, the favored model describes dark matter as a *cold* (made of non-relativistic particles, e.g. Blumenthal et al. 1984) pressureless fluid insensitive to radiative processes. Fig. 1.1 shows one of the major evidence of the existence of dark matter: weak lensing reconstruction of the gravitational mass distribution combined with hot gas distribution obtained from Chandra X-ray observations show offsets of the lensing mass peaks from the peaks of the dominant visible mass component, which demonstrates the presence, and dominance, of dark matter in the Bullet cluster (Clowe et al., 2004).

Baryons are found in stars and gas in galaxies as well as in intergalactic medium. At the opposite of dark matter, this "ordinary" matter is sensitive to electromagnetic interactions. It accounts for 4.5% of the energy content of the universe, about 17% of the total matter component and is mostly made of free hydrogen and helium, while heavier elements only represent about 0.03% of the total energy budget.

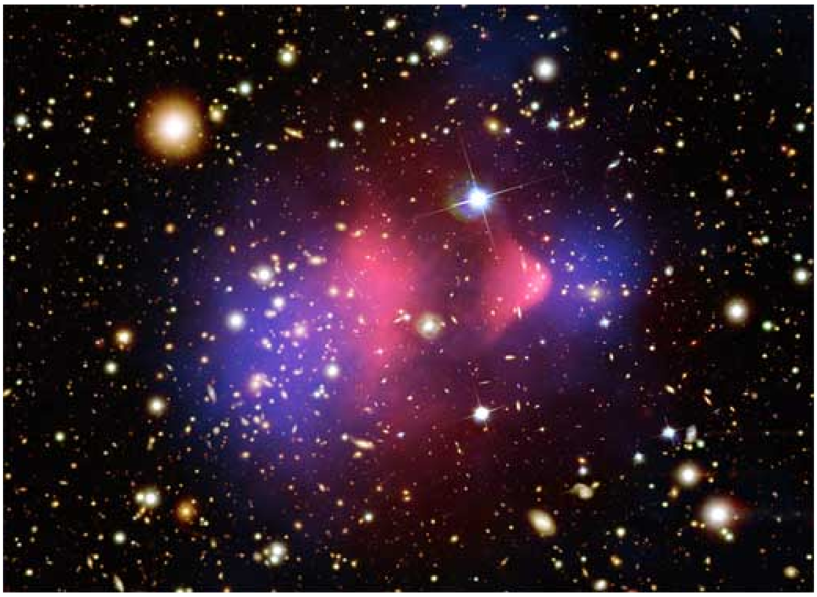

Figure 1.1: Dark matter direct evidence: image of the "Bullet" galaxy cluster. The hot gas distribution, from Chandra X-ray observations, is shown in red while the dark matter distribution, obtained from weak-lensing reconstruction, is shown in blue (Clowe et al., 2004).

1.2 The hierarchical structure growth

In this ΛCDM paradigm, structures grow according to the so-called *hierarchical* scenario: from initial small-scale perturbations in the density field, gravity drives the condensation of matter that finally collapses into small halos (see fig. 1.2), hosting the formation of stars and galaxies.

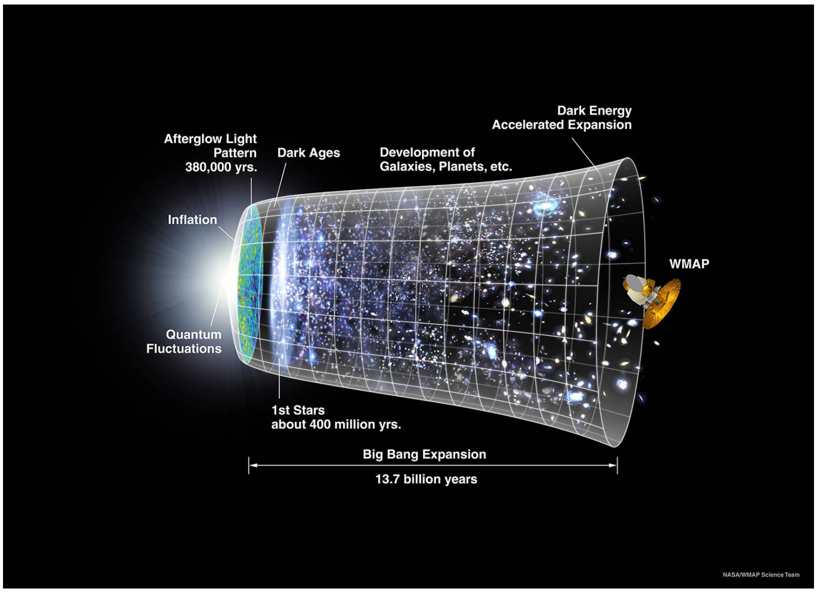

Figure 1.2: Timeline of the Universe (credit: NASA/WMAP Science Team). Small initial density perturbations as seen in the CMB are amplified through gravitational instability. Baryons follow the collapse of the dark matter halos to form the first stars and the first galaxies in their midst.

1.2.1 Dark matter halo : virialisation and profiles

Primordial halos form when dark matter undergoes phase mixing and violent relaxation before it settles into a *virial* equilibrium configuration:

$$2K + W = 0 \tag{1.1}$$

where K is the kinetic energy and W is the total potential energy of the halo. Navarro et al. (1997) first proposed, for these *virialized halos*, a spherical density profile with a steep inner slope that fits on a wide range of masses and radii halos obtained from hierarchical processes in numerical simulations:

$$\rho_{\mathrm{NFW}}(r) = \frac{\rho_0}{r(1 + r/r_0)^2} \tag{1.2}$$

The slope of the density profiles in the inner region is still debated since cosmological simulations tends to produce halos with a steep inner profile (*cusp*) while rotation curves of observed galaxies tends to indicate a constant inner density profile (*core*). This is referred to as the "core/cusp problem" (see de Blok 2010).

Although (Diemand et al., 2007) prove the NFW (cuspy) profile to be a good fit for dark matter halos from high resolution simulations, recent numerical studies showed that the Einasto (Einasto, 1965) (cored) profile was an even better match (Navarro et al., 2004; Stadel et al., 2009; Navarro et al., 2010).

$$\rho_{\mathrm{E}}(r) = \rho_0 \exp\left\{-\frac{2}{\alpha}\left[\left(\frac{r}{r_0}\right)^{\alpha} - 1\right]\right\} \tag{1.3}$$

The difference between cored and cuspy profiles is, for both observations and numerical simulations, hard to distinguish since it only appears at small scales. These scales are not yet resolved due to limited resolution in numerical simulations or observational uncertainties in the mass distribution reconstruction methods.

1.2.2 "Bottom-up" structure build-up and large scale structures

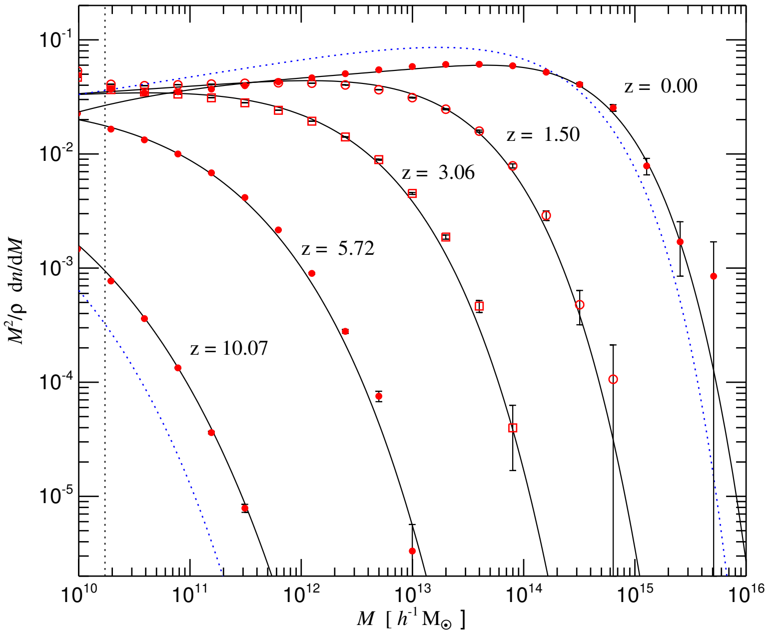

Figure 1.3: From Springel et al. (2005). Mass distribution of the dark matter halos at different redshifts in the Millennium simulation. The evolution of the mass distribution illustrates the bottom-up hierarchical growth of structure: at high redshift (early universe), the halo distribution is confined to the small masses, and evolves towards the higher masses as small halos merge to form more massive ones.

The first halos merge with each other to form more and more massive ones. Cosmological simulations easily reproduce this scenario: fig. 1.3 shows the evolution of the halo mass distribution with redshift in the Millennium simulation (Springel et al., 2005). While only low-mass halos were present in the early universe, halos with higher and higher mass appeared progressively with time.

As the density contrast increases over time in our universe and more and more massive structures appear, the distribution of these halos forms a "cosmic web" structure where large void bubbles are separated by filaments and walls. Fig. 1.4 shows the good agreement between large scale structures observations from the Sloan Sky Digital Survey (SDSS) and the 2-degree Field Galaxy Redshift Survey (2dFGRS) on one hand and the Millenium simulation (Springel et al., 2006) on the other hand.

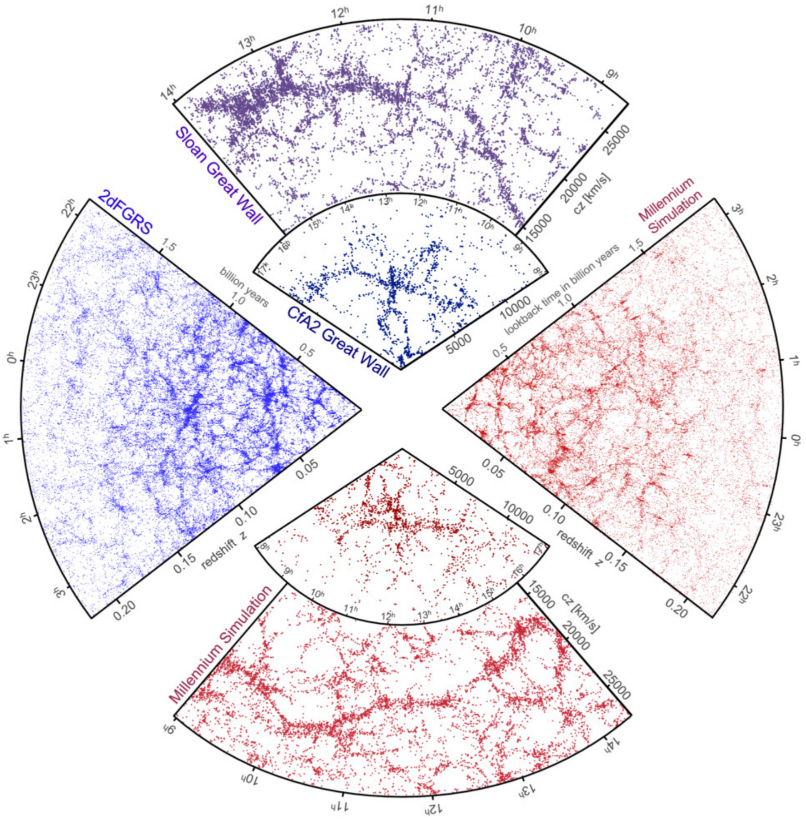

Figure 1.4: From Springel et al. (2006). The galaxy distribution obtained from spectroscopic redshift surveys and from mock catalogs constructed from the Millenium cosmological simulation.

1.3 First stars and first galaxies

1.3.1 Primordial spin and gas response to dark matter collapse

When dark matter condenses and finally collapses into halos in the early universe, it is believed that halos acquire initial angular momentum via tidal interactions (White, 1984) or mergers (Maller and Dekel, 2002) with neighboring halos. During this phase, the cosmological gas, whose density is dominated by the dark matter density, "falls" into the potential well of the halos and settles at virial equilibrium.

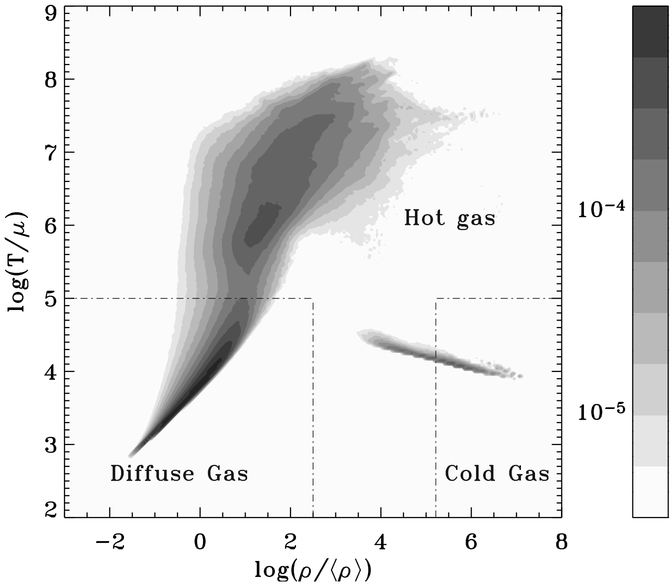

Figure 1.5: From Rasera and Teyssier 2006. $\rho - T$ phase diagram of the gas from a cosmological simulation with star formation and cooling. The phase diagram clearly shows the diffuse cosmological component, the hot gas in hydrostatic equilibrium within dark matter halos, and the dense and cold gas that constitutes the galaxies in the simulation. Note that feedback from supernovæ is not taken into account, and that the cold interstellar medium is not resolved.

Due to the collisional nature of the gas, kinetic energy from this gravitational collapse is converted into pressure. The gas is heated up (hot gas in fig. 1.5) to temperature of $\sim 10^6$ K. At the opposite of dark matter, baryons are sensitive to electromagnetic interactions and can radiate away their thermal energy (see fig. 1.6) via *radiative cooling* (White and Rees, 1978). Consequently, part of the halo gas cools down and, as it is no longer supported by pressure, falls to the center of the halo. The conservation of its initial angular momentum leads to the formation of a rotationally supported disk (Fall and Efstathiou, 1980).

1.3.2 First generation of stars and reionization of the Universe

The cooling of this primordial gas only made of light elements into a dense gaseous disk lead to the formation of H_2 molecules (Galli and Palla, 1998). The density and temperature ranges in these H_2 regions were appropriate for the formation of the first stars. Although never directly observed , these first stars (Pop. III) are thought to be short-lived, massive and metal-poor. The intense radiation feedback from these massive stars played a major role in the complete reionization of the gas in the Universe at $z \sim 7$ (Spergel et al., 2007). Their mass, probably over 100 $M_{\odot}$ prevents them to live for a period longer than a few Myrs, after which they collapsed into black holes or exploded into supernovæ. These supernova explosions produced heavy elements, enriching the interstellar medium with metals. Fig. 1.6 shows the increase of the radiative cooling efficiency due to the metal enrichment of the interstellar medium in a primordial gas. Finally, the cooling of the gas lead to the formation of the next generations of stars in these newborn galaxies.

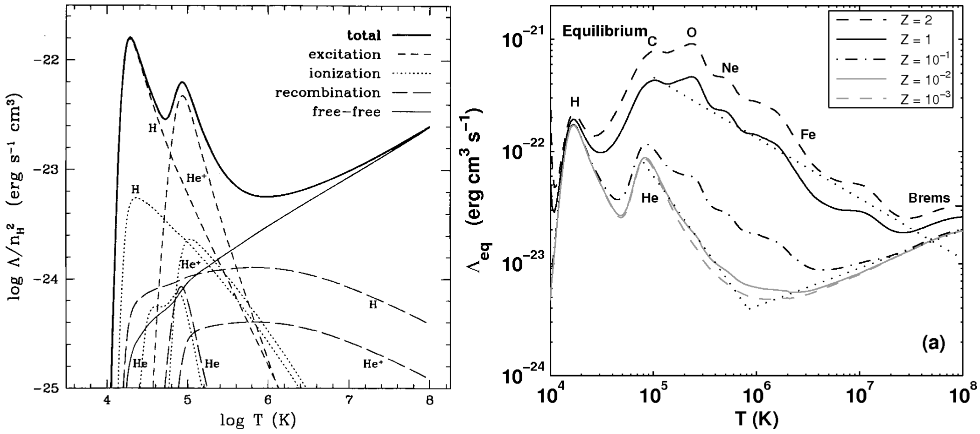

Figure 1.6: **(left)** from Katz et al. 1996. Cooling rates as a function of temperature for a primordial gas at virial equilibrium. **(right)** from Gnat and Sternberg 2007. Equilibrium cooling efficiency vs. temperature for metallicity Z from 10^{-3} $Z_{\odot}$ to 2 $Z_{\odot}$. The dominant cooling elements at various temperatures are indicated near the curves.

1.4 Galaxy mass growth

In the hierarchical model of structure formation, the evolution of every galaxy is linked to its dark matter halo history. The environment of a galaxy plays a major role in the evolution of its mass, its morphology and its inner dynamics. In this section, we review the different processes of galaxy growth.

1.4.1 Gas accretion

How galaxies get their gas is a key point in our understanding of galaxy formation since the parameters of the galactic gas reservoir determines the way they form stars during their evolution. Diffuse and cold cosmological gas, structured into large scale filaments, dragged into the potential well created by the dark matter halo, can fall toward its center at supersonic speed. In this case, an accretion shock can form nearly at virial radius and heat the infalling gas. Birnboim and Dekel (2003) and Dekel and Birnboim (2006) showed that such an accretion shock could not be stable for dark matter halos of mass below a critical mass $M_{\rm crit} \sim 10^{12}~M_{\odot}$. Consequently, two different modes of gas accretion were distinguished (see fig. 1.7):

- **Cold accretion mode**: in dark matter halos of mass $M_{\rm DM} < 10^{12}~M_{\odot}$, cosmological gas is accreted and falls into the center of the halo within a free-fall time ($T \sim 10^4 - 10^5$ K).

- **Hot accretion mode**: for $M_{\rm DM} > 10^{12}~M_{\odot}$ halos, the infalling gas is shock-heated (at typical temperature $T \sim 10^6$ K) and cools radiatively before it falls toward the center of the halo.

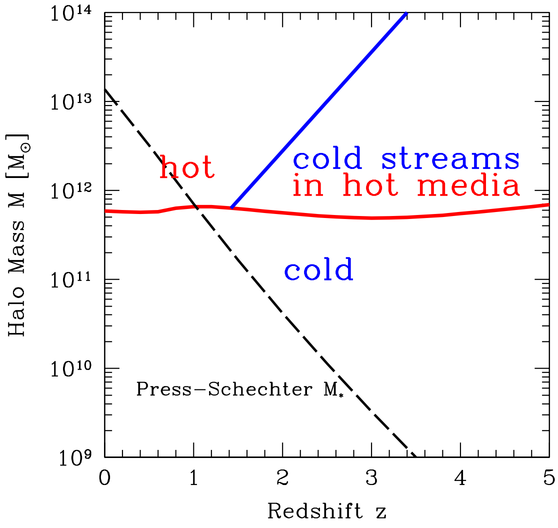

Figure 1.7: From Dekel et al. (2009). Gas accretion mode vs. redshift and halo mass. Below a critical halo mass of $\sim 10^{12}~M_{\odot}$, cold accretion mode occurs. Above, the gas is shock-heated and slowly cools down before it falls toward the center of the halo. However, at redshift $z \gtrsim 2$, dense cold streams can "worm their way in" and penetrate the hot gas halo.

They also predicted that gas feeding was also possible at high-redshift through cold flows made of dense gas where the cooling time was short enough to let the gas penetrate the halo. These results have been numerically confirmed by cosmological simulations (Kereš et al., 2005; Ocvirk et al., 2008; Kereš et al., 2009; Dekel et al., 2009). At redshift $z \gtrsim 2$, two different accretion modes are possible: cold accretion for low-mass ($M_{\rm DM} < 10^{12}\ M_\odot$) halos, and cold streams penetrating the hot gas halo for more massive ones (see fig. 1.8). Kereš et al. (2009) even argued that this last process dominates at high redshift.

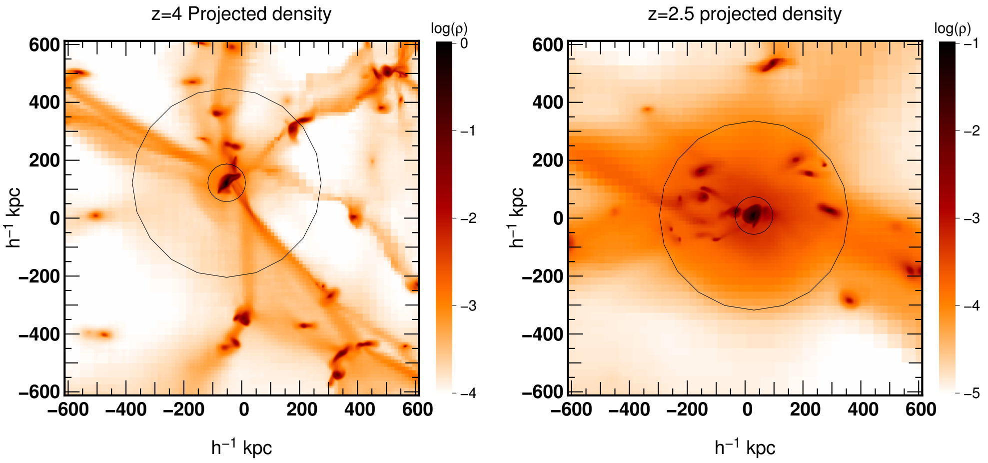

Figure 1.8: From Ocvirk et al. (2008). Gas density maps of a galactic halo illustrating accretion via cold streams in the MareNostrum simulation at redshift $z = 4$ (left) and $z = 2.5$ (right). The circle radii are $0.2R_{\rm vir}$ and $R_{\rm vir}$.

The numerical resolutions were not sufficient to determine whether these cold streams could replenish the gas content of the galactic disk until recent high-resolution simulations (Agertz et al., 2009b) showed evidence of the connection between these cold streams and the edges of the disk (see fig. 1.9). From numerical simulations, cold flows appear to be a very efficient process to feed the massive galaxies at high-redshift.

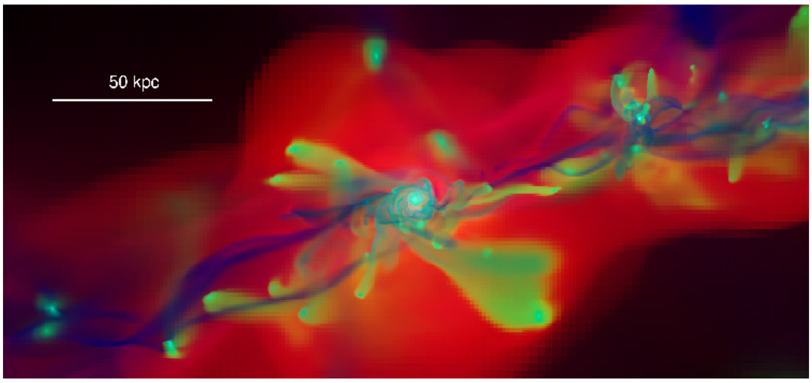

Figure 1.9: From Agertz et al. (2009b). RGB (R=temperature, G=metals and B=density) image of the gas showing the disk and accretion region at $z \sim 3$. The cold pristine gas streams in blue connecting directly onto the edge of the disk is clearly visible, as well as the shock heated gas in red surrounding the disk.

1.4.2 Galaxy merger history

In the bottom-up scenario of structure formation, dark matter halos merge with each other to form more and more massive ones. During the encounter of two halos, the galaxies they contain can interact and eventually merge together.

Galactic mergers are common events in the history of our Universe. Detection of close pairs of galaxies in sky surveys have lead to the temporal evolution of the galactic merger rate. Patton et al. (2002) found that the galaxy merger rates evolves with redshift as $(1+z)^{2.3\pm0.7}$. If the signature of a merger is quite difficult to detect in observations because of the lack of temporal information, it is far easier to detect in a large-scale cosmological simulation.

Dark matter halos can be detected numerically using algorithms such as *friend-of-friend* algorithms and merger rates are extracted from the simulations (Maller et al., 2006; Stewart et al., 2008; Genel et al., 2009; Fakhouri et al., 2010).

Stewart et al. (2008) showed that during the last 10 Gyr, 90% of Milky-way-sized dark matter halos ($M_0 \simeq 10^{12}\ M_\odot$) have accreted at least one satellite more massive than $5\times10^{10}\ M_\odot.\mathrm{h}^{-1}$, and 40% of them have accreted a halo more massive than $2\times10^{11} M_\odot.\mathrm{h}^{-1}$ (see fig. 1.10). At $z=0$, the mass accretion of such a halo is dominated by 1-4 mergers with objects of mass $m \simeq (0.03-0.3)M_0$ over its history.

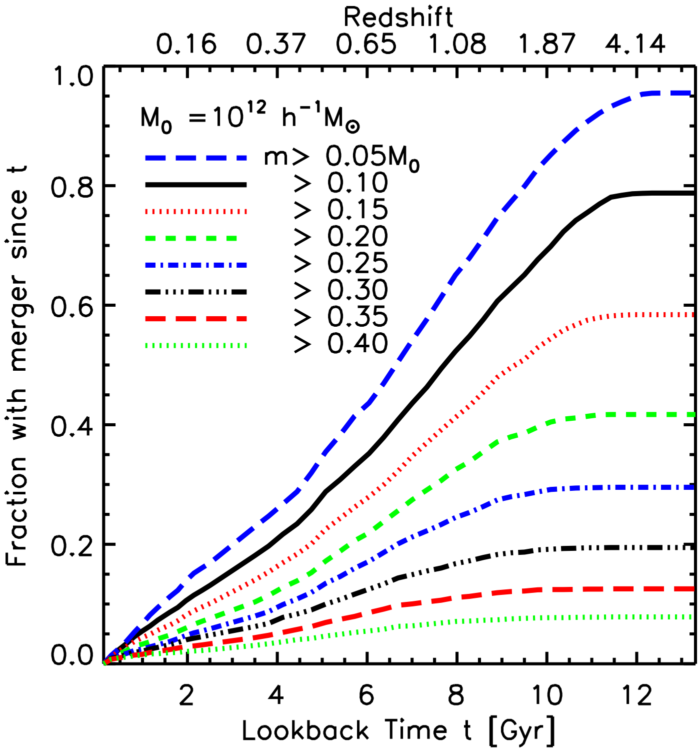

Figure 1.10: From Stewart et al. (2008). Fraction of Milky-Way-sized halos, $M_0 \simeq 10^{12}\ M_{\odot}.\mathrm{h}^{-1}$, that have experienced at least one merger larger than a given mass threshold m since look-back time t. 90% of them have accreted at least one satellite more massive than $5 \times 10^{10}\ M_{\odot}.\mathrm{h}^{-1}$ in the last 10 Gyr.

However, halo merger rate and galaxy merger rate are not directly correlated and Genel et al. (2009) even highlighted that dark matter halo detection and merger rates computation depended on the chosen algorithm. Since they don't model the baryonic component, dark matter only cosmological simulations can't provide useful information on the galactic merger rate. Only hydrodynamical cosmological simulations following the galaxies make it straightforward (Maller et al., 2006), although their computational cost is dramatically higher, particularly at low-redshift.

Most galaxies underwent a few mergers in their history. Even if they are not so frequent, galaxy mergers have a great impact on the dynamics, the morphology, the star formation and the evolution of galaxies. These processes will be discussed in details in the next chapter.

CHAPTER 2

Galaxies: dynamics, interactions and evolution

In this chapter, we will first introduce the different morphologies of observed galaxies. Then we will focus on the interstellar medium and briefly review some analytical considerations on disk instabilities. We will present the process of star formation, in molecular clouds and on galactic scales. Finally we will detail the impact of galaxy interactions and mergers on the different processses governing the evolution of galaxies: disk instabilities, star formation and formation of supermassive black hole binaries.

2.1 The Hubble sequence

Observed galaxies are found in not only a wide range of masses but also different morphologies. In the Local Universe, galaxies are classified into *early-type* galaxies (ellipticals and lenticulars) and *late-type* galaxies (spirals with or without bars), according to the so-called *Hubble sequence*, as shown in fig. 2.1.

Spiral galaxies are more common in our Universe ($\sim 2/3$ of massive galaxies). Usually, these extended disky structures supported by their rotation contains two different components:

- a thick ($\sim$ 1 kpc thickness) stellar disk made of old stars with velocity dispersion order of magnitude of ~ 50 km.s^{-1}.
- a thin gaseous disk (a few ~ 100 pc thickness) producing a thin and young stellar disk where the velocity dispersion is lower ($\sim 5-10$ km.s^{-1}).

The observed brightness of these galaxies can be approximated by an exponential profile $I(r) \propto \exp(-r/r_0)$. The 2 or 4 armed spiral structure found in $\sim 50\%$ of grand design spiral galaxies (Elmegreen and Elmegreen, 1982) is due to density wave (Lin and Shu, 1964) propagating in the gas and the stars where the pattern speed of the spiral is $\Omega(r) - \kappa(r)/2$.

The gas is shocked in the spiral arms, inducing an enhanced star formation in these regions. This is why the spiral arms are more clearly visible through interstellar gas or young star distribution observations.

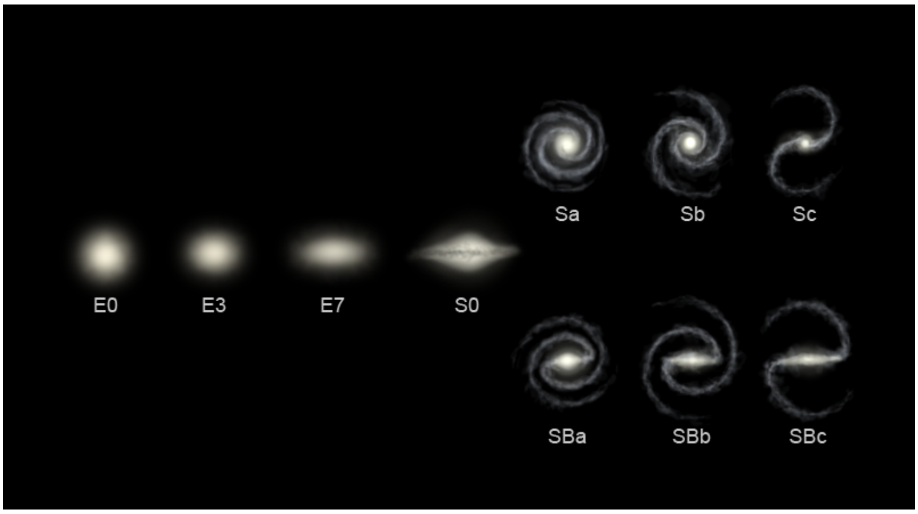

Figure 2.1: Hubble sequence (image credit: Ville Koistinen). Observed galaxies are classified according to their morphology: ellipticals (E0-E7) and lenticulars (S0) are early-type galaxies. Spiral galaxies (Sa-Sc and Sba-Sbc) constitute the late-type galaxies.

A symmetry break of the gravitational potential can occur at the center of spiral galaxies, leading to the formation of *bars*. Bars are very common structures since they can be found in $\sim 80\%$ of the galaxies in the Local Universe (Block et al., 2004). They are easily destroyed but can reform after a sufficient gas infall makes the disk prone to bar instability again (Combes, 2000; Bournaud and Combes, 2002). These structures are mostly made of stars the orbit of which are precessing at a given circular frequency Ω_b, independant of radius. The gas usually concentrates on the leading side of the bar, undergoes negative gravity torques and falls toward the center of the galaxy. This modification of the angular momentum distribution is a very efficient process to feed the central bulge of the galaxy.

Spiral galaxies are classified according to the presence of a bar (S or SB) and the size of their bulge. Sc and SBc galaxies have a small bulge and loosely wound arms whereas Sa and SBa have a massive bulge and tighlty wound arms. However, no bulge is detected in $\sim 16\%$ of spiral galaxies in the Local Universe (Kautsch et al., 2006).

Elliptical galaxies account for about one third of massive galaxies. These galaxies have a spheroidal shape, are usually gas-poor and are supported by the velocity dispersion of the stars. Their brightness usually follow a Sérsic profile $I(r) \propto \exp(-b_n(r/r_{1/2})^{1/n})$ where $r_{1/2}$ is the half-light radius. A typical value of Sérsic index $n = 4$ was first introduced by de Vaucouleurs (1948), resulting in the so-called *de Vaucouleurs* profile. Elliptical galaxies can be classified according to their box-like or disk-like shape (Bender et al., 1988; Bender, 1988; Kormendy and Bender, 1996), depending on the predominance of their anisotropic velocity dispersion over their rotation.

However, Emsellem et al. (2007) introduced a kinematic classification of early-type galaxies based on stellar angular momentum per unit mass measurements. *Slow rotators* ($\sim$ 25%) are massive elliptical galaxies with a round shape and a high Sérsic index. They contain old stars and have very little gas. Their photometric and kinematic components are usually misaligned, at the opposite of *fast rotators*. Fast rotators ($\sim$ 75%) are relatively low-mass galaxies (ellipticals or lenticulars) with a more disky shape.

2.2 The interstellar medium (ISM)

The interstellar medium is made of neutral, ionized and molecular gas (mostly hydrogen and helium) and dust ($\sim$ 1% of the mass). It can be divided into several phases (Ferrière, 2001):

- Hot ionized medium ($T \sim 10^6$ K, $\rho \sim 10^{-3}$ H.cm^{-3}) can be found in the halos of the galaxies and is is generated by supernova explosions and, to a lesser extent, by the powerful stellar winds from supernova progenitors (see, e.g, McCray and Snow, 1979; Spitzer, 1990).
- Warm ionized medium ($T = 8 \times 10^3$ K, $\rho = 0.2 - 0.5$ H.cm^{-3}) can be found in HII regions around OB stars.
- Cold neutral medium ($T = 50 - 100$ K, $\rho = 20 - 50$ H.cm^{-3}) and Warm neutral medium ($T = 6 \times 10^3 - 10^4$ K, $\rho = 0.2 - 0.5$ H.cm^{-3}). Neutral atomic gas (HI) has two thermally stable phases: a cold dense phase, in which the primary cooling mechanism is the radiative deexcitation of collisionally excited fine structure lines of metals, and a warm rarefied phase, resulting from the onset of L_α cooling at $\sim$ 8000 K. Both phases can coexist in thermal pressure balance (see, e.g. McKee and Ostriker, 1977; Wolfire et al., 1995).
- Molecular medium ($T = 10 - 20$ K, $\rho = 10^2 - 10^6$ H.cm^{-3}) In very dense and cold regions, hydrogen atoms are thought to recombine to form H_2 molecules. This reaction is catalized by the presence of interstellar dust grains (Hollenbach and Salpeter, 1971) which concentrates half of the mass of metals in the ISM. H_2 molecules can only survive in the interiors of dark and optically thick clouds, which are cold enough to avoid collisional

dissociation and shielded from photons coming from external UV sources (Shull and Beckwith, 1982).

The interstellar medium is a complex, multi-phase and turbulent structure (see e.g. Yepes et al., 1997; Springel and Hernquist, 2003) where a lot of physical processes are involved. Here we review the radiative cooling/heating, star formation, supernovæ feedback and the various gas instabilities which play a major role in the dynamics of the interstellar medium.

2.2.1 Cooling function and heating sources

The amount of energy per unit time and volume radiated away via atomic processes by gas at density ρ, temperature T and metallicity Z is

$$\epsilon_{\mathrm{cool}} = n_{\mathrm{H}}^2 \Lambda(\rho, T, Z) \tag{2.1}$$

where n_{H} is the hydrogen number density. Fig. 1.6 highlights the fact the cooling function Λ strongly depends on the temperature and the metallicity of the gas. The radiative cooling involves different microscopic processes (Gnat and Sternberg, 2007):

- Bremsstrahlung dominates for temperature above 10^7 K.
- In the range $10^5 - 10^7$ K, in metallic gas, collisional ionization of different metals dominates the cooling process: $\sim 10^5$ K (carbon), $\sim 3 \times 10^5$ K (oxygen), $\sim 5 \times 10^5$ K (neon) and $\sim 3 \times 10^6$ K (iron). For $Z = 0.01\ Z_{\odot}$ gas, metal cooling becomes negligible in this temperature range and the cooling is dominated by He^+ Ly_α cooling.
- Hydrogen atoms Ly_α cooling peaks at $T \simeq 2 \times 10^4$ K and becomes less efficient at higher temperature where the neutral hydrogen fraction becomes small.
- Below 10^4 K, Wolfire et al. (1995) showed that CII and OI fine-structure lines enable the gas ($\rho > 1$ H.cm^{-3}) to cool down to $T \sim 40$ K. Molecular (CO and CS) line cooling can let the gas cool down even lower temperatures (Scoville and Solomon, 1974).

Young, hot and massive O and B stars emits a strong UV radiation which, below E=13.6eV, is sufficiently energetic to ionize the hydrogen atoms. They play the role of major heating source in HII regions of the warm ionized medium. In the neutral medium, the main source is due to photoelectric heating on dust grains and large molecules such as polycyclic aromatic hydrocarbons (PAHs). The hot ionized medium is heated by extreme UV and soft X-rays emitted by supernova remnants.

2.3 Molecular clouds, star formation and feedbacks

2.3.1 Formation of Molecular Clouds

Molecular clouds are the dense and cold gas clouds commonly found in the densest regions of galactic disks such as spiral arms (Heyer and Terebey, 1998). They host stellar formation sites (see fig. 2.3) and the most massive ones, where the star formation is more active, are called Giant Molecular Clouds (GMCs). They have typical masses in the range 10^4 – a few $10^6 M_\odot$, typical size of ~ 10 pc and their average density is of order $\sim 100\ \mathrm{cm}^{-3}$, which is thick and dense enough to shield the interior of the cloud from the background UV photons, preventing the photodissociation of molecules. This process is called *self-shielding*. That is why GMCs are very rich in molecular hydrogen (H_2) as well as CO and HCN molecules at temperature of order ~ 10 K.

Two different scenarios have been proposed to explain the formation of such structures (see e.g. McKee and Ostriker, 2007, and references therein). First, the top-down scenario: large-scale hydrodynamical or magnetorotational instabilities leading to the fragmentation of the ISM into a myriad of GMCs (see fig. 2.2). Second, small HI clouds coagulation due to turbulent colliding flows in the ISM, possibly induced by the passage of spiral arms or by SN explosions.

The second scenario is not captured by the limited resolution of galactic-scale numerical simulations. On the other hand, for the second scenario, a realistic multiphase ISM with cold dense clouds embedded in a warmer phase naturally arises in numerical simulations (see fig. 2.2) of marginally unstable disk galaxies ($Q \lesssim 1$) when the thermodynamical model allow the gas to cool down below $T \sim 10^4$ K (Tasker and Bryan, 2006; Agertz et al., 2009a; Kim et al., 2009; Tasker and Tan, 2009).

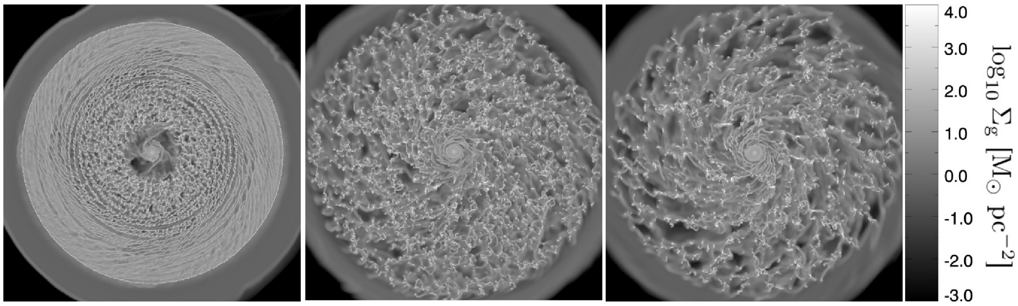

Figure 2.2: From Tasker and Tan (2009). Gas surface density maps of a galactic gaseous disk at $t = 100, 200, 300$ Myr after the beginning of the simulation. The gaseous disk is unstable and rapidly fragments into a myriad of GMCs.

2.3.2 Star formation in molecular clouds and feedback processes

Inside each cloud, the star formation proceed in a very structured way. New stars are formed inside *pre-stellar cores* of size ~ 0.05 pc and $n_{\mathrm{H}_2} \gtrsim 10^5\ \mathrm{cm}^{-3}$, embedded into *dense cores* of size of ~ 0.1 pc and $n_{\mathrm{H}_2} \sim 10^4\ \mathrm{cm}^{-3}$ (Bergin and Tafalla, 2007).

Figure 2.3: From Arzoumanian et al. (2011) Composite RGB image ($\sim 1.6\ \mathrm{deg}^2$) of the star forming regions in the IC5146 molecular cloud obtained with the PACS/SPIRE instruments of the Herschel space observatory (R=SPIRE 500 μm and 350 μm, G=SPIRE 250 μm and PACS 160 μm, B=PACS 70 μm).

The dense cores are embedded in a molecular cloud that can be part of a GMC. The equilibrium of a cloud is determined by the complex interplay of gravity, rotation, and thermal, turbulent and magnetic pressure. The two different scenarios proposed for the formation of dense cores and pre-stellar cores condensation are often discussed in (animated) debates. In the first scenario, the magnetic field is thought to play a major role in the equilibrium of molecular clouds. The cloud collapses when its mass reaches a critical value and the gravity overcomes its magnetic pressure (Mouschovias, 1976). The magnetic support is damped during the collapse through *ambipolar diffusion* (Basu and Mouschovias, 1994), resulting in the fragmentation of the cloud into dense cores and pre-stellar cores. The turbulence is the key process in the second scenario: the supersonic turbulence induces a log-normal distribution of the gas density PDF over a wide range of density (Elmegreen, 1997; Mac Low and Klessen, 2004) and pre-stellar cores form in the densest regions (Padoan et al., 2007) where the gas of the molecular cloud collapses after the turbulence is rapidly damped.

When their gas density reach is high enough, pre-stellar cores can form new stars of mass following the so-called *Initial Mass Function* (IMF, see e.g. Salpeter, 1955; Kroupa, 2001; Chabrier, 2003). Bright massive OB stars emit a strong UV radiation that efficiently dissociates molecules, preventing the formation of other stars in the nearby region. Among all the stars created in the pre-stellar cores, $\sim 10\%$ of them have masses $M > 10\ M_\odot$. These short-lived stars will explode in supernovæ within ~ 10 Myr, reinjecting metals and a dramatic amount of energy ($E \sim 10^{51}$ ergs) back into the ISM. Part of this energy is radiated away while a great amount of kinetic energy is released in the ISM, sustaining the level of turbulence (de Avillez and Breitschwerdt, 2007) and responsible for the galactic winds and formation of superbubbles (Springel and Hernquist, 2003; Dubois and Teyssier, 2008). The presence of metals in the ISM is of major importance for the ability of the gas to form new stars since it is a key parameter for the cooling efficiency (see fig. 1.6).

2.3.3 Star formation at galactic scale

Since the first observations of a scaling relation between the star formation rate and the gas density by Schmidt (1959), many star formation laws have been discussed. Kennicutt (1989, 1998) introduced the so-called *Schmidt-Kennicutt law* that links the total (atomic and molecular) gas surface density with the star formation surface density as follows

$$\Sigma_{\rm SFR} = (2.5 \pm 0.7) \times 10^{-4} \left(\frac{\Sigma_{\rm gas}}{1 M_\odot.{\rm pc}^{-2}} \right)^{(1.4 \pm 0.15)} \qquad M_\odot.{\rm yr}^{-1}.{\rm kpc}^{-2} \tag{2.2}$$

for a large sample of spiral and starburst galaxies. This relation have been confirmed in more recent studies based on larger galaxy samples (e.g. GALEX Boissier et al., 2007).

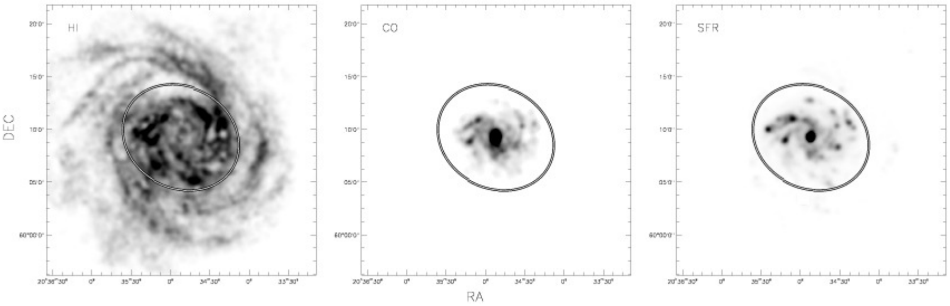

Figure 2.4: From Bigiel et al. (2008). Observed maps of the atomic gas (left), molecular gas (CO, middle) and star formation rate (right) surface density. Most stars form inside the optical radius (ellipses), within dense cores of molecular clouds while atomic gas often extends beyond the optical radius.

While a large scatter appears in this scaling relation, the star formation surface density seems more closely correlated to the molecular gas surface density (see e.g. Bigiel et al., 2008, and fig. 2.4) or even more to the HCN surface density (Gao and Solomon, 2004). Whatever the relation, the star formation process is only efficient above a gas surface density $\Sigma_{\mathrm{gas}} \sim 10\ M_{\odot}.\mathrm{pc}^{-2}$ corresponding to a volume density $\rho \sim 100\ \mathrm{cm}^{-3}$. In regions more diffuse than molecular clouds, the background UV radiation can penetrate and dissociate the molecules, preventing the gas from cooling further to form stars.

Daddi et al. (2010a); Genzel et al. (2010) have highlighted two distinct star formation sequences independent of redshift

$$\Sigma_{\mathrm{SFR}_{\mathrm{disk}}} = 10^{-3.83} \left(\frac{\Sigma_{\mathrm{gas}}}{1 M_{\odot}.\mathrm{pc}^{-2}} \right)^{1.42} \quad M_{\odot}.\mathrm{yr}^{-1}.\mathrm{kpc}^{-2} \qquad (2.3)$$

$$\Sigma_{\mathrm{SFR}_{\mathrm{starburst}}} = 8 \times \Sigma_{\mathrm{SFR}_{\mathrm{disk}}} \qquad (2.4)$$

where the star formation law for ultra-luminous infrared galaxies (ULIRGs) and sub-millimeter galaxies (SMGs) undergoing a strong burst of star formation (starburst sequence) is higher by 0.9 dex than the star formation law of isolated spiral and BzK galaxies (spiral sequence, see fig. 2.5). This sequence shift between isolated and starburst galaxies might be due to a different molecular gas fraction in dense clouds.

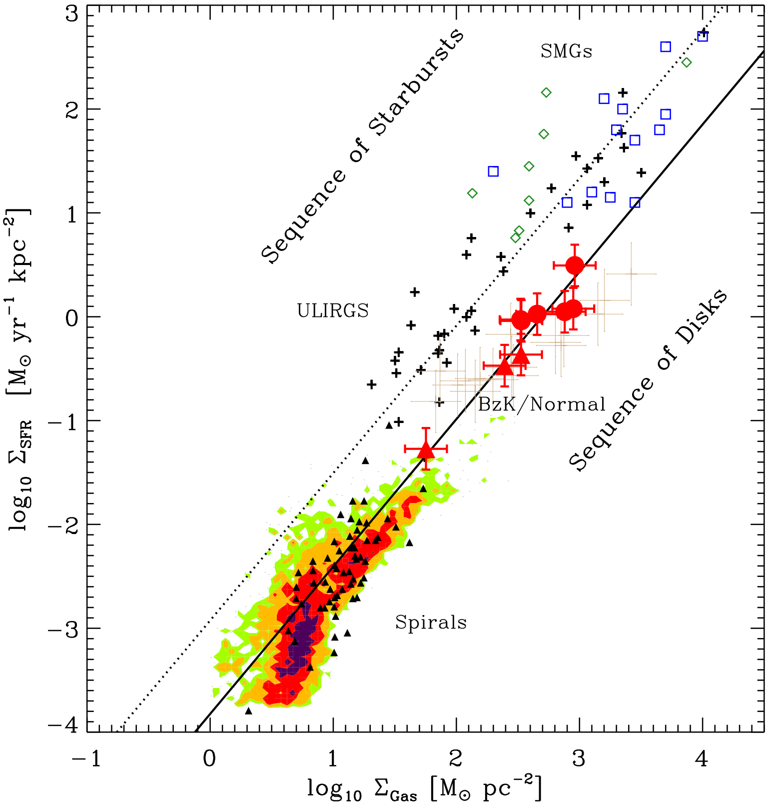

Figure 2.5: Star formation rate surface density as a function of the gas (atomic and molecular) surface density from Daddi et al. (2010a) for various galaxy samples (Daddi et al., 2010b; Tacconi et al., 2010; Bouché et al., 2007; Bothwell et al., 2009; Kennicutt, 1998; Bigiel et al., 2008). (lower solid line) local spirals and $z = 1.5$ BzK galaxies fit (eq. 2.3). (upper dotted line) local (U)LIRGs and SMGs fit (eq. 2.4).

2.4 Analytical considerations on disk instabilities

A galactic rotating disk is a near-equilibrium system where gravity counterbalances thermal and turbulent pressure as well as rotation. Traditionally, the *density wave theory* introduced by Lin and Shu (1964) explains the spiral patterns observed in disk galaxies. Here is an overview of the instabilities a galactic disk can undergo. If one only considers the gas, one can derive the Euler equations and the Poisson equation governing the dynamics of a thin self-gravitating rotating gaseous disk with surface density Σ:

$$\frac{\partial \mathbf{v}}{\partial t} + (\mathbf{v}\cdot\nabla)\mathbf{v} = -\frac{1}{\Sigma}\nabla p - \nabla\Phi \tag{2.5a}$$

$$\frac{\partial \rho}{\partial t} + \nabla\cdot(\rho\mathbf{v}) = 0 \tag{2.5b}$$

$$\Delta\Phi = 4\pi G\Sigma \tag{2.6}$$

A polytropic equation-of-state can be taken for the gas as $p = K\Sigma^\gamma$. Then, the sound speed writes

$$c_\mathrm{s}^2 = \left(\frac{\mathrm{d}p}{\mathrm{d}\Sigma}\right)_{|\Sigma_0} = \gamma K\Sigma_0^{\gamma-1} \tag{2.7}$$

Assuming an adiabatic gas ($\mathrm{d}s = 0$), one can replace the pressure by the *specific enthalpy* ($\mathrm{d}h = T\mathrm{d}s + \mathrm{d}p/\rho = \mathrm{d}p/\rho$)

$$h(\Sigma) = \int \frac{1}{\Sigma'}\frac{\mathrm{d}p(\Sigma')}{\mathrm{d}\Sigma'}\mathrm{d}\Sigma' = \frac{\gamma}{\gamma-1}K\Sigma^{\gamma-1} \tag{2.8}$$

In cylindrical coordinates, eq. 2.5 become

$$\frac{\partial V_\mathrm{r}}{\partial t} + V_\mathrm{r}\frac{\partial V_\mathrm{r}}{\partial r} + \frac{V_\phi}{r}\frac{\partial V_\mathrm{r}}{\partial \Phi} - \frac{V_\phi^2}{r} = -\frac{\partial(\Phi+h)}{\partial r} \tag{2.9a}$$

$$\frac{\partial V_\phi}{\partial t} + V_\mathrm{r}\frac{\partial V_\phi}{\partial r} + \frac{V_\phi}{r}\frac{\partial V_\phi}{\partial \Phi} + \frac{V_\phi V_\mathrm{r}}{r} = -\frac{1}{r}\frac{\partial(\Phi+h)}{\partial \phi} \tag{2.9b}$$

$$\frac{\partial \Sigma}{\partial t} + \frac{1}{r}\frac{\partial(r\Sigma V_\mathrm{r})}{\partial r} + \frac{1}{r}\frac{\partial(\Sigma V_\phi)}{\partial \phi} = 0 \tag{2.9c}$$

The Euler equations can be linearized (see Binney and Tremaine, 2008, p.488-496): the axisymmetric unperturbed disk is described by (order 0)

$$V_{\mathrm{r}_0} = 0 \;\; ; \;\; \partial/\partial\phi = \partial/\partial t = 0 \;\; ; \;\; V_{\phi_0} = \sqrt{r\frac{\partial(\Phi_0+h_0)}{\partial r}}) \simeq \sqrt{r\frac{\partial\Phi_0}{\partial r}} = r\Omega(r)$$

where Ω is the *circular frequency*. Here, the enthalpy term is negligible, it is about the same order of magnitude than the sound speed ($c_\mathrm{s} \sim 10$ km.s^{-1}) compared to the rotation velocity in a galaxy ($V_{\mathrm{circ}} \sim 200$ km.s^{-1}).

The first order linearization ($\epsilon \ll 1$, $V_{\mathrm{r}} = \epsilon V_{\mathrm{r}_1}$, $V_\phi = r\Omega + \epsilon V_{\phi_1}$, $h = h_0 + \epsilon h_1$, $\Sigma = \Sigma_0 + \epsilon \Sigma_1$, $\Phi = \Phi_0 + \epsilon \Phi_1$) of eq. 2.8 and eq. 2.9 writes

$$h_1 = \gamma K \Sigma_0^{\gamma-2} \Sigma_1 = c_{\mathrm{s}}^2 \frac{\Sigma_1}{\Sigma_0} \tag{2.10a}$$

$$\frac{\partial V_{\mathrm{r}_1}}{\partial t} + \Omega \frac{\partial V_{\mathrm{r}_1}}{\partial \Phi} - 2\Omega V_{\phi_1} = -\frac{\partial(\Phi_1 + h_1)}{\partial r} \tag{2.10b}$$

$$\frac{\partial V_{\phi_1}}{\partial t} + \left[\frac{\partial(\Omega r)}{\partial r} + \Omega\right] V_{\mathrm{r}_1} + \Omega \frac{\partial V_{\phi_1}}{\partial \Phi} = -\frac{1}{r} \frac{\partial(\Phi_1 + h_1)}{\partial \phi} \tag{2.10c}$$

$$\frac{\partial \Sigma_1}{\partial t} + \Omega \frac{\partial \Sigma_1}{\partial \phi} + \frac{1}{r} \frac{\partial(r \Sigma_0 V_{\mathrm{r}_1})}{\partial r} + \frac{\Sigma_0}{r} \frac{\partial V_{\phi_1}}{\partial \phi} = 0 \tag{2.10d}$$

We can define one of the so-called Oort constant[1] $B(r)$ as

$$-2B(r) = \frac{\partial(\Omega r)}{\partial r} + \Omega(r) \tag{2.11}$$

and the *epicyclic frequency* $\kappa(r)$ (Vandervoort, 1975) as

$$\kappa^2(r) = -4B(r)\Omega(r) \tag{2.12}$$

The first order quantities, solution of this system, vary like $\exp[\mathrm{i}(kr + m\phi - \omega t)]$ where ω is the angular frequency, $k = 2\pi/\lambda$ is the wave number and m is a positive integer (the perturbation has m-fold rotational symmetry). From eq. 2.10 come the amplitude relations:

$$V_{\mathrm{r}a}(r) = \frac{\mathrm{i}}{\Delta}\left[(\omega - m\Omega)\mathrm{i}k(\phi_a + h_a) - \frac{2m\Omega}{r}(\phi_a + h_a)\right] \tag{2.13a}$$

$$V_{\phi a}(r) = -\frac{1}{\Delta}\left[2B\mathrm{i}k(\phi_a + h_a) + \frac{m(\omega - m\Omega)}{r}(\phi_a + h_a)\right] \tag{2.13b}$$

$$-\mathrm{i}(\omega - m\Omega)\Sigma_{da} + \mathrm{i}k\Sigma_0 V_{\mathrm{r}a} + \frac{\mathrm{i}m\Sigma_0}{r} V_{\phi a} = 0 \tag{2.13c}$$

$$h_a = c_{\mathrm{s}}^2 \frac{\Sigma_{da}}{\Sigma_0} \tag{2.13d}$$

where

$$\Delta \equiv \kappa^2 - (\omega - m\phi)^2 \tag{2.14}$$

The perturbed volicities may diverge when $\Delta = 0$ at the *Linbald resonances* where a more careful treatment is required (Goldreich and Tremaine, 1979). The singularity arises when the *pattern speed* Ω_p satisfies

$$\Omega_p = \frac{\omega}{m} = \Omega \pm \frac{\kappa}{m} \tag{2.15}$$

---

[1] estimated at the solar radius in the Milky-way galaxy.

We employ the tight-winding approximation (or WKB approximation) which requires that $|kr| \gg 1$ ($|kr| \simeq 7 - 11$ in two-armed spiral galaxies).
As a consequence, the terms $\propto 1/r$ are negligible compared to those $\propto k$ in eq. 2.13:

$$V_{\mathrm{r}a} = -\frac{(\omega - m\Omega)}{\Delta} k(\phi_a + h_a) \tag{2.16a}$$

$$V_{\phi a} = -\frac{2\mathrm{i}B}{\Delta} k(\phi_a + h_a) \tag{2.16b}$$

$$-(\omega - m\Omega)\Sigma_{da} + k\Sigma_0 V_{\mathrm{r}a} = 0 \tag{2.16c}$$

The potential amplitude Φ_a is imposed by a surface density of amplitude Σ_a through the Poisson equation eq. 2.6. For a self-consistent density wave, Σ_a should be equal to Σ_{da}

$$\Phi_a = -\frac{2\pi G\Sigma_a}{|k|} = -\frac{2\pi G\Sigma_{da}}{|k|} \tag{2.17}$$

Finally, eq. 2.13d, eq. 2.16 and eq. 2.17 yield the *dispersion relation*

$$(\omega - m\Omega)^2 = \kappa^2 - 2\pi G\Sigma|k| + c_{\mathrm{s}}^2 k^2 \tag{2.18}$$

where the disk is stabilized (positive terms) by the shear of the flow ($\propto \kappa$) and the thermal pressure ($\propto c_{\mathrm{s}}^2$) and destabilized by the self-gravity of the disk (negative term $\propto -\Sigma$). The stability of the disk requires that $(\omega - m\Omega)^2 \geq 0$. Positive solutions of $|k|$ exists if the so-called *Toomre stability criterion* is satisfied

$$Q_g = \frac{\kappa c_{\mathrm{s}}}{\pi G\Sigma} > 1 \tag{2.19}$$

A similar criterion was first proposed for stellar disks by Toomre (1964)

$$Q_* = \frac{\kappa\sigma_*}{3.36 G\Sigma_*} > 1 \tag{2.20}$$

where the stellar velocity dispersion σ_* plays the same stabilizing role of turbulent pressure as the thermal pressure support (c_{s}) in the gas. In most cases, galactic disks contain both stars and gas. Two-component stability analysis have been done (Jog and Solomon, 1984; Elmegreen, 1995; Jog, 1996; Rafikov, 2001) and lead to an effective stability criterion

$$\frac{1}{Q_{\mathrm{tot}}} = \frac{2}{Q_*}\frac{q}{1+q^2} + \frac{2}{Q_g}\frac{Rq}{1+q^2R^2} > 1 \tag{2.21}$$

where $R = c_{\mathrm{s}}/\sigma_*$ and $q = k\sigma_*/\kappa$. This effective Toomre parameter proved to be more accurate to trace the unstable regions in observations (see, e.g. Corbelli 2003 for M33 and Yang et al. 2007 for the Large Magellanic Cloud).

From the dispersion relation eq. 2.18, two typical scale lengths can be derived for a gas-only disk. First, if we assume that the gas is not rotating ($\kappa = 0$), the *Jeans instability* can arise for

$$|k| < k_J = \frac{2\pi G\Sigma}{c_s^2} = \frac{2\pi}{\lambda_{\text{Jeans}}} \Rightarrow \lambda > \lambda_{\text{Jeans}} = \frac{c_s^2}{G\Sigma} \tag{2.22}$$

The small scales are stabilized when the thermal pressure dominates the self-gravity of the disk. At the opposite, large scales are stabilized when the rotation dominates the self-gravity of a cold disk ($c_s = 0$). The *Toomre instability* can occur when

$$|k| < k_{\text{Toomre}} = \frac{\kappa^2}{2\pi G\Sigma} = \frac{2\pi}{\lambda_{\text{Toomre}}} \Rightarrow \lambda < \lambda_{\text{Toomre}} = \frac{4\pi^2 G\Sigma}{\kappa^2} \tag{2.23}$$

When $Q_g = 1$, all perturbation scales are stable. For $Q_g < 1$, the fastest growing unstable mode corresponds to $|k| = 2\pi/\lambda$ where λ satisfies

$$2\lambda_{\text{Jeans}} = \lambda = \frac{Q_g^2}{2}\lambda_{\text{Toomre}} \tag{2.24}$$

2.5 Galaxy interactions and mergers

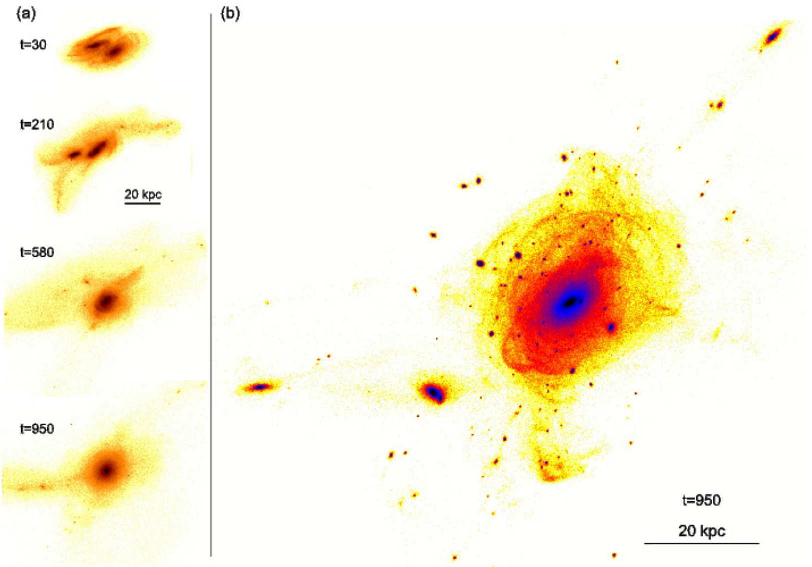

Figure 2.6: Elliptical galaxy resulting from the merger (a) of two equal-mass spiral galaxies, ~ 950 Myr after the first pericentric passage. This simulation shows compact Super Stellar Clusters (SSCs) all around the remnant galaxy, together with massive tidal dwarf galaxies (TDGs) along the tidal tails (Bournaud et al., 2008).

The interactions between galaxies are violent events that not only impact the mass evolution of a galaxy but also their morphology and inner dynamics. Galaxy mergers may occur when their dark matter halo interpenetrate and their orbital energy is dissipated via dynamical friction (Chandrasekhar, 1943). Part of this energy is evacuated through kinetic energy of escaping high velocity stars while the rest is converted into random motions. During the merger, the modification of the gravitational potential may result in the relaxation of the system, the randomization of the stellar orbits, the formation of tidal structures, modifications in the galaxy morphology and violent star formation episodes.

2.5.1 Tidal fields, gravity torques, spiral arms and dynamical friction

The tidal field partly drives the stellar and gas response during galaxy interactions. During the distant interaction between two galaxies, the tidal field is mostly disruptive and tends to tear apart the galactic disks.

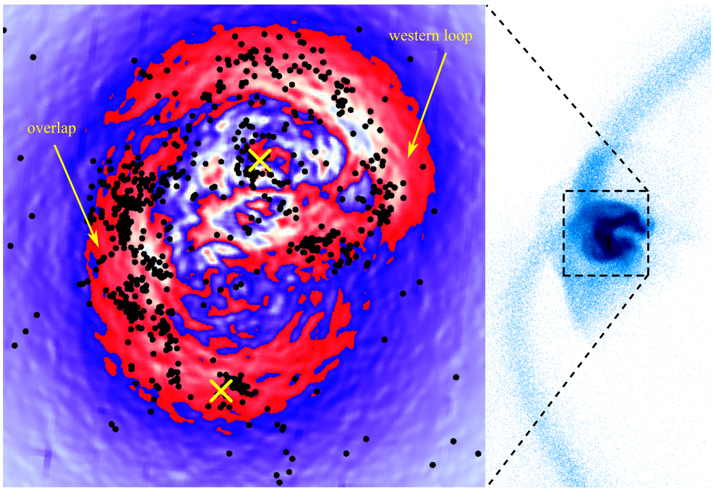

Figure 2.7: From Renaud et al. (2008). Compressive tides in an advanced stage of the Antennæ galaxy merger simulation. The blue to red colors label extensive to progressively more compressive mode. White corresponds to a neutral tidal field. The black dots indicate the positions of the young cluster candidates identified by Mengel et al. (2005).

Compressive modes of tidal fields can occur during a more advanced stage of a merger and trigger star formation bursts (see fig. 2.7 Renaud et al., 2008). But the interaction of a galaxy with a companion induces an asymmetry in the gravitational potential. Consequently, the material undergoes gravity torques which are more intense in the case of a *prograde* interaction (same orientation of the orbit and the disk rotations) than in the case of a *retrograde* (opposite orientations) interaction.

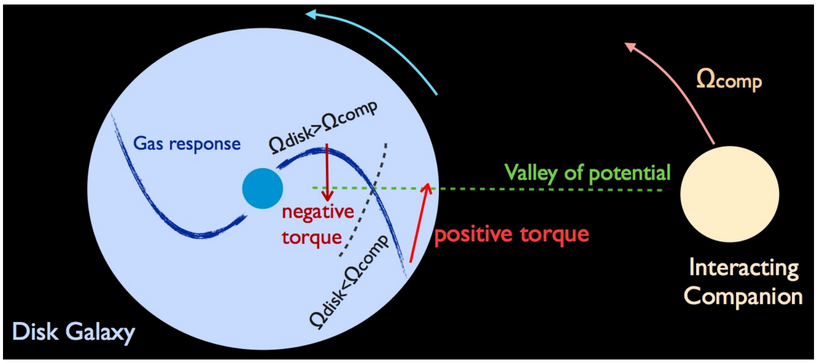

Figure 2.8: From Bournaud (2010). Gas response basic scenario during galaxy interaction. Outside the corotation radius, positive gravity torques drive the material from the outer in tidal tails. Inside the corotation radius, negative torques drive a central gas inflow.

Fig. 2.8 illustrates the gas response to such gravity torques. Inside the corotation radius (where $\Omega(r) = \Omega_{\text{companion}}$, $r \sim$ a few kpc), the material concentrates on the leading side of the potential valley and undergoes negative torques. The loss of angular momentum leads to an inflow of material toward the center of the galaxy. At the opposite, outside the corotation radius, it concentrates on the trailing side, undergoes positive torques and gain angular momentum . This additional angular momentum leads to the formation of the so-called *tidal tails*.

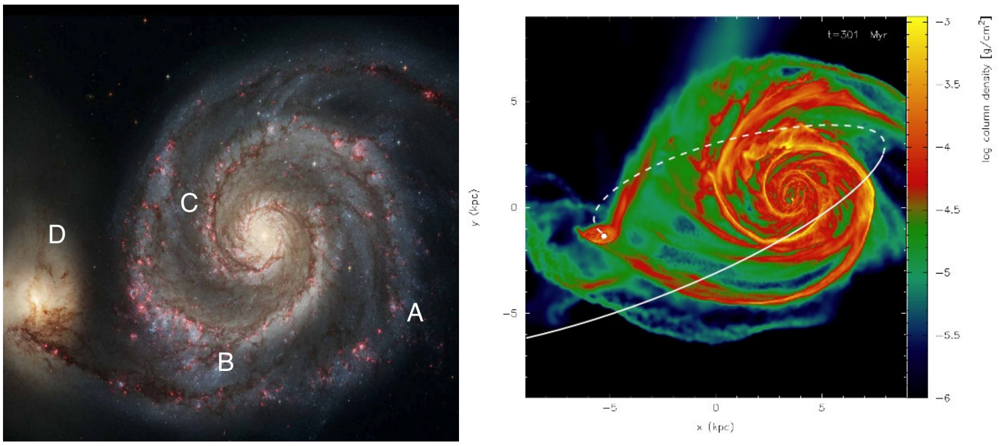

Figure 2.9: Interaction-driven spiral pattern : M51. HST image (left) compared to simulation of M51 interacting with its companion, NGC5195 (Dobbs et al., 2010).

Both tidal fields and gravity torques are responsible for the formation of tidal structures and the central inflow of gas, as illustrated by Toomre and Toomre (1972) (tidal fields) and Toomre (1981) (gravity torques). Due to its larger typical velocity dispersion and its collisionless dynamics, the stellar component is much less sensitive to these gravity torques than the gas. As a consequence, There is neither a significant stellar central inflow nor a great amount of pre-existing stars in tidal tails and *tidal dwarf galaxies* (TDGs; e.g Duc et al. 1997 for Arp105, Duc et al. 2000 for Arp245).

Large scale spiral structures can be maintained in a quasi-steady state in isolated disk galaxies but the interaction with another galaxy tends to excite a $m = 2$ spiral mode in the disk (e.g. Oh et al., 2008). The formation of grand design spiral arms may be triggered by the interaction with a less massive galaxy (see e.g. Dobbs et al., 2010, and fig. 2.9).

Dynamical friction

First introduced by Chandrasekhar (1943) in the case of a stellar background, dynamical friction is now more generally referred to as the gravitational interaction exerted on a massive object (the perturber) moving through a discrete (stars or dark matter halo) or continuous (ISM) matter distribution. For a particle of mass M_p moving at velocity $\mathbf{V_p}$ through a medium of density ρ with velocity dispersion σ, the gravitational drag exerted on the perturber writes

$$\mathbf{F}_{\rm df} = -4\pi\rho\sigma^2 R_{\rm BH}^2 f^{(*,{\rm gas})}\frac{\mathbf{V_p}}{V_p} \tag{2.25}$$

where $R_{\rm BH}$ is the radius of a *sphere of gravitational influence* of the perturber. The dynamical friction against the dark matter halo is one of the main cause of the galactic orbital decay (and merger) of interacting galaxies. At much smaller scales, dynamical friction against the gaseous or stellar background plays a major role in the dynamics of massive black holes (MHBs and see chapter 5). In the case of an accreting perturber moving in a continuous gaseous medium, $R_{\rm BH}$ is often referred to as the Bondi radius (Bondi and Hoyle, 1944) $R_{\rm B} = GM_{\rm p}/c_{\rm s}^2$ (Ruffert, 1996). Chandrasekhar (1943) provided an expression for the dimensionless factor f^* in the case of a Maxwellian distribution of star velocities:

$$f^* = \ln\Lambda\left[{\rm erf}(X) - \frac{2X}{\sqrt{\pi}}e^{-X^2}\right] \tag{2.26}$$

where $X = V_p/(\sigma\sqrt{2})$ and $\ln\Lambda = \ln(r_{\rm max}/r_{\rm min})$ is the *Coulomb logarithm* ($r_{\rm max}$ and $r_{\rm min}$ accounts for the maximum and minimum radial contributions to the drag).

The analytical study by Ostriker (1999) demonstrated that, in the case of a gaseous medium with velocity dispersion $\sigma = c_{\rm s}$, the dynamical friction efficiency $f^{(\rm gas)}$ writes:

$$f^{(\rm gas)}_{\rm subsonic} = \frac{1}{2}\ln\left(\frac{1+\mathcal{M}}{1-\mathcal{M}}\right) - \mathcal{M} \tag{2.27}$$

$$f^{(\rm gas)}_{\rm supersonic} = \frac{1}{2}\ln\left(\mathcal{M}^2 - 1\right) + \ln\Lambda \tag{2.28}$$

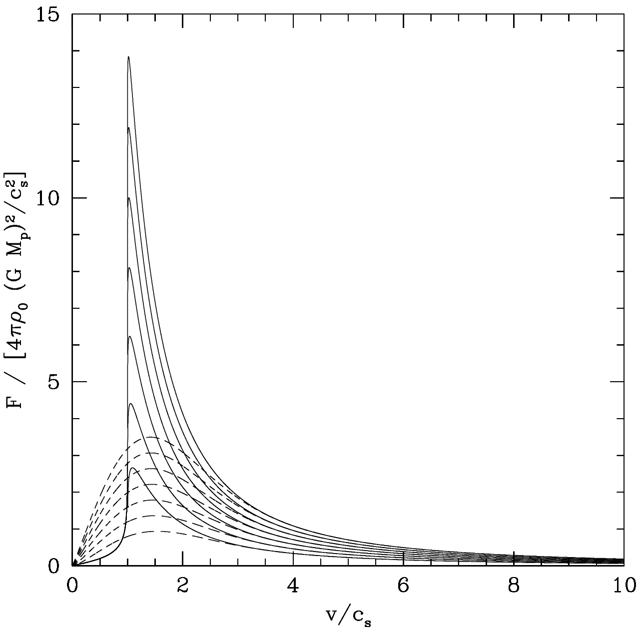

Figure 2.10: From Ostriker (1999). Dynamical friction efficiency in a gaseous medium (solid lines) and in a stellar background (dashed lines) as a function of the Mach number $\mathcal{M} = V_{\mathrm{p}}/c_{\mathrm{s}}$ for different values of the Coulomb logarithm $\ln\Lambda = 4, 6, 8, \ldots$

where the Mach number $\mathcal{M} = V_p/c_s$. This theoretical prediction suggested a peaking gaseous dynamical friction efficiency at transsonic regime although numerical studies have claimed that these formulae were probably overestimating the effect of dynamical friction at transsonic regime (Sánchez-Salcedo and Brandenburg, 2001; Escala et al., 2004).

2.5.2 Impact of mergers on galaxy morphology

The consequences of a galaxy merger depend on the orbit, the gas fraction and mostly on the mass ratio of the interacting galaxies. Mergers with a galactic mass ratio between 1:1 to 4:1 are called *major merger* whereas *minor mergers* have a mass ratio above 4:1. During a major merger, the gravitational potential undergoes a brutal modification. The induced relaxation of the system is violent and leads to the randomization of the stellar orbits (Lynden-Bell, 1967), resulting in a Maxwellian distribution of energies of the stars. Stellar disks are esaily destroyed during such events.

On the other hand, the consequences of a minor merger are less dramatic. While mergers with a mass ratio greater than 10:1 merely disturb the disk in spiral galaxies, those with a mass ratio between 4:1 and 10:1 lead to bulge growth

(Bournaud et al., 2005), thickening and radial expansion of the stellar disk (Toth and Ostriker, 1992) and result in the formation of a lenticular galaxy (Bournaud et al., 2004).

A large set of both analytical studies and numerical simulations have studied the properties of galaxy merger remnants. They show that elliptical galaxies can form after a major merger (Barnes, 1992; Mamon, 1992; Naab and Burkert, 2003; Bournaud et al., 2004, 2005, 2008; Cox et al., 2006; Jesseit et al., 2009) or, if frequent enough, after multiple minor mergers (Bournaud et al., 2007; Naab et al., 2007). Naab et al. (2009) argued that repeated minor mergers could explain the evolution of high-redshift compact spheroids into present-day elliptical galaxies.

Major mergers are also thought to induce the strongest bursts of star formation (Barnes and Hernquist, 1991; Mihos and Hernquist, 1996; Cox et al., 2006), while the star formation activity rapidly decreases with increasing mass ratio (Cox et al., 2008; Di Matteo et al., 2008; Manthey et al., 2008; Knierman, 2010). We will detail the process of star formation burst during galaxy mergers in the next section.

2.5.3 Merger-driven star formation bursts

Observations (e.g. Elbaz and Cesarsky, 2003) and numerical models (e.g. Hopkins et al., 2006) indicate that galaxies formed a significant fraction of their stars during violent interactions and mergers. Nevertheless, the overall contribution of mergers to the star formation budget of galaxies remains uncertain and quiescent star formation in isolated systems could dominate (Jogee et al., 2009; Robaina et al., 2009; Förster Schreiber et al., 2009; Daddi et al., 2010b).

In general, merger-induced star formation is assumed to be centrally concentrated and to fuel the formation of bulges and compact spheroids rather than extended disks (Naab and Burkert, 2003; Bournaud et al., 2004). The mechanism usually invoked, first proposed by Barnes and Hernquist (1991), to explain merger-induced starbursts is that gravity torques drive the gas inward inside the corotation radius, usually a few kpc. The gas density rapidly increases in the central regions, and so does the star formation rate. These results were quantified in merging galaxy simulations compared to the same galaxies in isolation and the star formation rate was increased by a factor of a few units (Di Matteo et al., 2008) to a few tens (e.g. Mihos and Hernquist, 1996; Cox et al., 2006).

A fundamental and general observational fact about interacting galaxies is that their star formation proceeds in GMCs and star clusters, which can be $10 - 100$ times more massive than in normal spiral galaxies, leading in particular to the formation of super star clusters (SSCs; Whitmore et al., 2007). A proposed theoretical explanation is increased gas turbulence (Elmegreen et al., 2000; Struck et al., 2005), so that the Jeans mass, which sets the typical mass of gas clouds, becomes larger while the free-fall time of these gas clouds decreases. Another mechanism involves shock-induced star formation bursts due to an enrichment of the gas density PDF toward high densities at the collision interface (Saitoh et al., 2009, and fig. 2.11). Such a mecanism has also been found in a model of the Mice galaxies (Barnes, 2004). Both mechanisms could trigger the star formation activity of interacting galaxies, independent of the traditional central inflow mechanism.

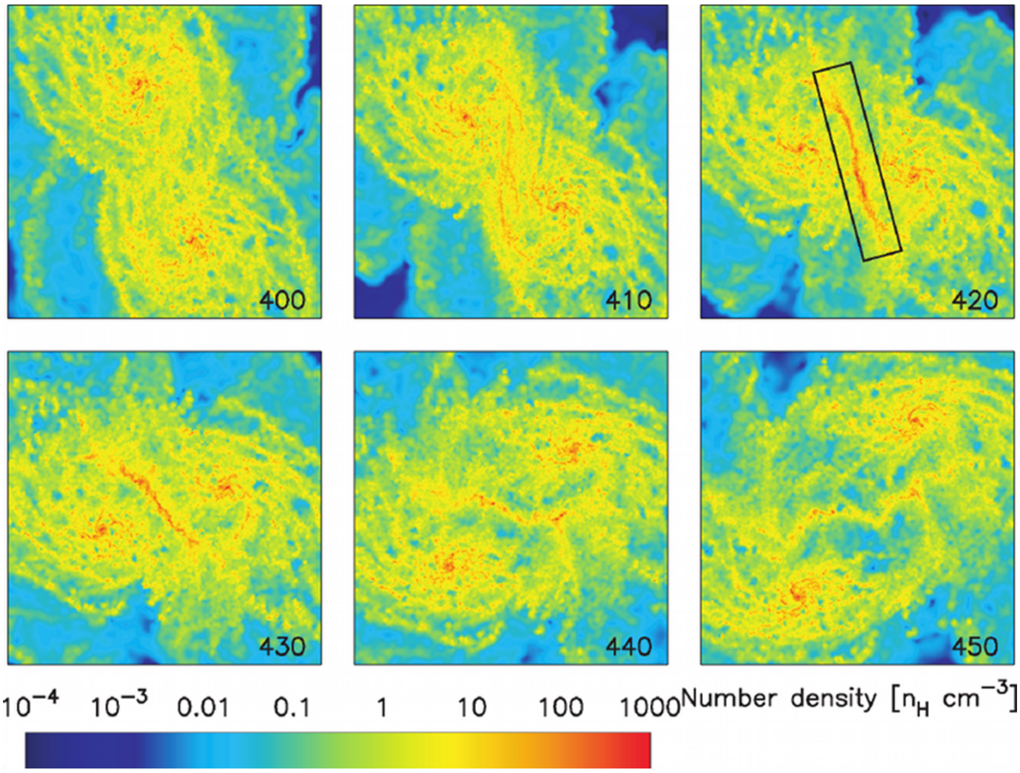

Figure 2.11: From Saitoh et al. (2009). Shock-induced star formation simulation of merging galaxies. The gas density PDF is enriched toward high density values at the collision interface where an intense star formation leads to the formation of stellar clusters.

2.5.4 AGN feedback and SMBHs pairing during galaxy merger

AGN feedback

Most galactic spheroids appear to host in their center a supermassive black hole (SMBH) with mass ranging from 10^5 to a few $10^9 M_\odot$ (see e.g. Ferrarese and Ford, 2005). Ferrarese and Merritt (2000); Tremaine et al. (2002) demonstrated that the black hole mass is almost perfectly correlated with the central velocity dispersion of their host in the so-called $M_{\mathrm{BH}} - \sigma_{\mathrm{c}}$ relation

$$M_{\mathrm{BH}} \propto \sigma_{\mathrm{c}}^{4.8\pm0.5} \tag{2.29}$$

An intense nuclear activity (jets or winds) is observed in some of these galaxies, particularly at high redshift (e.g. Reeves et al., 2003; Nesvadba et al., 2008). The nuclear region of such galaxies, called *active galactic nuclei* (AGN) are thought to exert some feedback on the ISM. Numerical simulations have included AGN feedback processes (Springel, 2005; Hopkins et al., 2005) to study the quenching of star formation in massive early-type galaxies. The parameters of such models are finely tuned so the consequences of AGN feedback on the quenching of star formation is still debated (Cattaneo et al., 2009).

SMBHs binary formation

In the context of galaxy mergers, mergers between SMBHs could be common, especially at high redshift when the galaxy merger rate is higher. However, the merger rate of SMBHs does not follow trivially from that of their host galaxies. Once the two galaxy cores have merged, leaving no distinct substructure at hundred of parsecs/kiloparsec scales, the two black holes will need to reduce their separation to less than 0.01 pc before they can start to lose orbital energy effciently via gravitational wave emission and eventually coalesce (Begelman, Blandford, and Rees, 1980). The coalescence of two SMBHs would produce the loudest gravitational wave signals in the Universe, and is the main target of planned low-frequency gravitational wave experiments, such as space-based laser interferometers and pulsar timing arrays (Vecchio, 2004; Sesana et al., 2009). Loss of orbital energy can occur via dynamical friction onto the stellar background (Milosavljević and Merritt, 2001) or due to the gas drag (Escala et al., 2004). Both mechanisms are relevant since SMBHs are inferred to exist at the center of both gas-rich spirals and gas-poor ellipticals/S0s (Volonteri et al., 2008). The first one is known to become ineffective when the binary begins to harden; at this stage the 3-body interactions between the binary and individual stars deplete its loss cone, which can be refilled only via some orbital diffusion mechanism that brings fresh stellar material from other regions of the galaxy (Berczik et al., 2005).

In recent years it has been shown that SMBH decay in a gas dominated system is much more effective at forming rapidly a binary of SMBHs, in only a few million years following the major merger of two moderately gas-rich disk galaxies (Mayer et al., 2007; Mayer and Kazantzidis, 2008). The reason is that the decay occurs in a much denser medium relative to the stellar dominated case, and because the black holes are in a nearly transsonic regime where the dynamical friction in a gaseous medium is expected to be more effective than in a collisionless system (Ostriker, 1999). Indeed the two black holes spiral down to parsec scales in a gaseous, dense nuclear disk of size $\sim$ 100 pc formed by the dramatic gas inflow in the merger. Such nuclear disks have been found in high resolution multi-wavelength observations of nearby merger remnants (Downes and Solomon, 1998; Davies et al., 2007). In minor mergers efficient black hole pairing at scales of tens of parsecs, namely even before a bound binary can form, requires high gas fractions ($> 30\%$) in both galaxies (Callegari et al., 2009, 2011) strengthening even further the crucial role of gas in the pairing and merging of SMBHs.

2.6 Conclusion

2.6.1 Limits of gas physics in galaxy simulations

Merger-driven clustered star formation bursts

So far, most existing models of galaxy mergers studying the star formation activity do not resolve clustered star formation in dense cold gas clouds. Numerical models of interacting galaxies lack the spatial resolution range, the mass resolution and temperature range required to capture star formation in an turbulent and inhomogeneous multiphase ISM. In many cases, a model for gas cooling below $\sim 10^4 K$ is missing. The star formation process is instead treated as a relatively smooth process (at least at scales of $100 - 1000$ pc), taking place in a relatively homogeneous ISM supported by thermal pressure ($T \sim 10^4$ K) instead of a cloudy ISM supported by turbulent motions. Star cluster formation is then only indirectly modeled using sub-grid recipes (e.g. Li et al., 2004). Only a few models of galaxy mergers can directly resolve cold gas clouds and clustered star formation (e.g. Wetzstein et al., 2007; Bournaud et al., 2008) but the properties of merger-induced star formation burst were not studied.

SMBHs pairing in galaxy merger simulations

First, many numerical investigations on the SMBHs pairing process resulting from a galaxy merger chose to start the simulation when the two black holes already form a loosely bound pair in a nuclear disk. They have suggested that the decay can continue to sub-pc scales under certain conditions but have utilized pre-defined models of nuclear disks (Escala et al., 2005; Dotti et al., 2006, 2007; Cuadra et al., 2009) rather than starting from a realistic galaxy merger and appeal to tidal torques rather than dynamical friction when the binary begins to harden. At the smallest scales they have assumed very specific configurations such as that of two black holes already at less than 0.1 pc separation embedded in a gap within the disk (Cuadra et al., 2009). Gap opening implies the transition to a regime in which tidal torques from the surrounding disk become the dominant mode to extract energy and angular momentum from the binary. However, the configuration of the host on which the two black holes are found at less than parsec scales is not really known because no computation exists that can reach such a stage starting from a realistic merger, and consequently the decay in such regime is not yet explored by three-dimensional simulations.

Until now, studies of binary black hole formation and shrinking in a gaseous environment have been based exclusively on SPH simulations, which might be unable to capture the turbulent nature of the flow in the disk. Turbulence arises as a result of shocks during the final galaxy collision, and later in the nuclear disk as a result of its gravitational instability (Mayer et al., 2007; Mayer and Kazantzidis, 2008). Furthermore, dynamical friction, which is the central physical process involved, is numerically challenging to capture since it involves both the effect of the local overdensity trailing the black holes and that of the larger scale torques and tidal distortions generated by the surrounding mass distribution (Colpi et al., 1999). While TreeSPH codes such as `GASOLINE` (Wadsley et al., 2004) are typically well suited to address processes in the domain of self-gravitating systems, to which category dynamical friction belongs, particle noise and the difficulty to resolve gradients between media of different densities (such as the overdense wake and the surrounding background), may cast doubts on the quantitative results regarding the strength of dynamical friction. More generally, confirmation of the results of SPH calculations on the effectiveness of the SMBH binary formation process in a gaseous environment is desirable. Due to the many scales involved, adaptive mesh refinement (AMR) simulations are ideally suited to the problem.

2.6.2 Outline of this thesis

This thesis will adress these issues based on numerical studies of galaxy mergers. First, chapter 3 will introduce the AMR hydrodynamical code `RAMSES` used to perform the numerical simulations. The additional modules developed in the course of this thesis for the specific purpose of galaxy merger simulations and associated thermodynamical model will be presented.

The chapter 4 will focus on the merger-induced clustered star formation burst in a high-resolution merger simulation based on a model of the Antennæ galaxies (NGC4038/39).

In chapter 5, results on the SMBHs pairing process and the dynamical friction due to a gaseous medium during a galaxy merger simulation will be presented.

CHAPTER 3

Galactic binary merger with `RAMSES`

In this chapter the AMR hydrodynamical code `RAMSES` is presented as well as the additional `RAMSES` modules developed for the specific purpose of galaxy merger simulations.

3.1 The AMR hydrodynamical code `RAMSES`

In cosmological and galaxy modeling applications, two different approaches are widely used in modern computational astrophysics :

Eulerian grid-based methods for hydrodynamical flow modelling.

Lagrangian particle-based methods such as Smooth Particles Hydrodynamics (SPH; Springel, 2005; Wadsley et al., 2004) or grid-based methods based on moving mesh (Springel, 2010).

`RAMSES`[1] (Teyssier, 2002) is a massively parallel Adaptive Mesh Refinement hydrodynamical code for self-gravitating plasma flows, written in Fortran90. A Magneto-Hydrodynamics (MHD) solver has also been implemented in `RAMSES` as well as many other physical ingredients such as star formation, interstellar medium cooling function, intergalactic background UV heating and supernovæ feedback.

In galaxy simulations performed with `RAMSES` :

- **stars** and **dark matter** are described by massive particles and modeled as a N-body collisionless fluid.
- the **gas** is described by a density/velocity/pressure/energy field discretised on an adaptatively refined grid.

---

[1] *Raffinement Adaptatif de Maillage Sans Effort Surhumain*
web: `http://irfu.cea.fr/Projets/Site_ramses/RAMSES.html`.

3.1.1 Adaptative mesh refinement

Modelization of the systems for which `RAMSES` has been designed often requires a wide dynamical range. As gravity tends to condense astrophysical structures like cosmological filaments, galaxies, giant molecular clouds or stars, very high density contrasts naturally appear in the simulations. On the one hand, a fine resolution together with small-scale physical ingredients are necessary to model the densest structures which only fill a small fraction of the simulation domain volume. On the other hand, a fine resolution is not required for large, empty and information-poor regions. To tackle the modelization of such systems, `RAMSES` implements the *adaptative mesh refinement* technology together with physical grid-refinement criteria.

Patch-based versus tree-based AMR

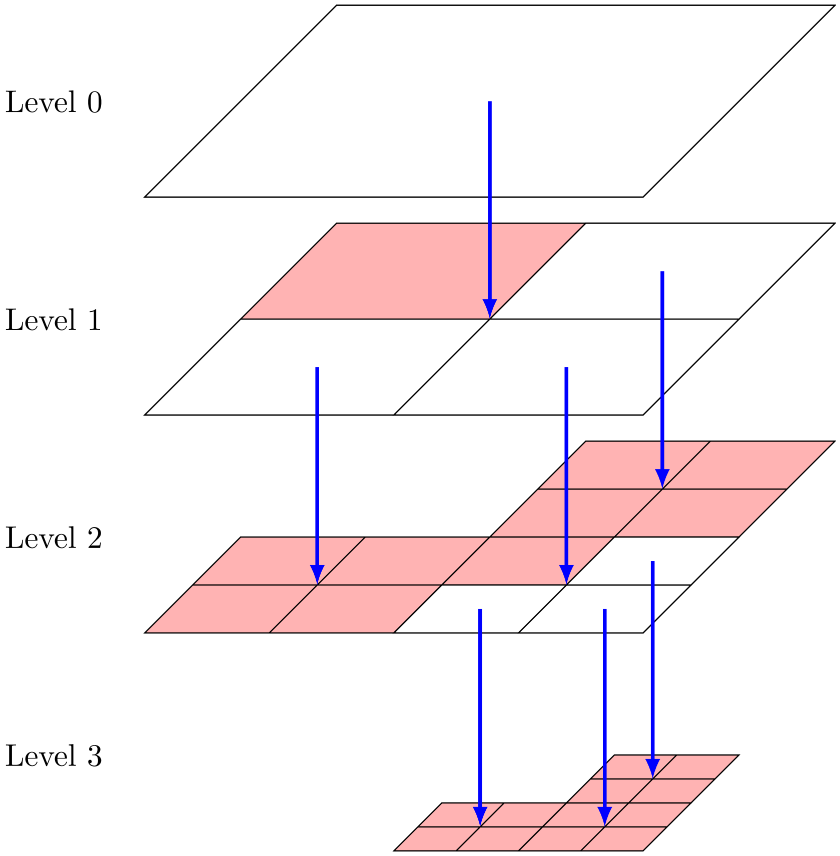

Figure 3.1: 2D illustration of a cell-based AMR quadtree. The white cells are *split cells* (i.e. refined cells), while the red cells are *leaf cells*. The leaf cells, when gathered from all AMR levels, form a partition of the computational domain (the top-level white cell).

The Adaptative Mesh Refinement method was first introduced in Berger and Oliger (1984). It consisted in a hierarchy of rectangular grid blocks of various size and resolution or *nested grids*. Slightly different from this *patch-based* approach, a *tree-based* approach was introduced by Barnes and Hut (1986). Khokhlov (1998) proposed a grid refinement method where the parent cells are refined into son cells on a cell-by-cell basis.
In computational astrophysics, a few AMR codes use the patch-based approach (ENZO[2], O'Shea et al. 2004 ; FLASH[3], Fryxell et al. 2000) or the tree-based approach (ART, Kravtsov et al. 1997; `RAMSES` , Teyssier 2002).

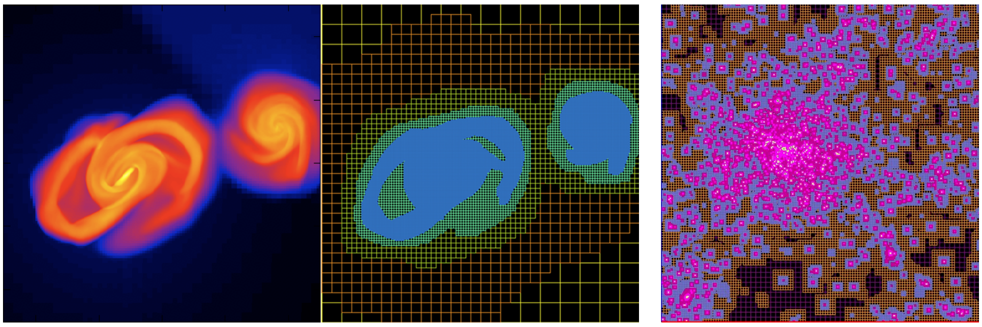

Figure 3.2: (Left, middle) gas density and AMR grid from a `RAMSES` galaxy merger simulation. (Right) AMR grid around a galaxy cluster from a cosmological simulation.

The data structure is less complex in the patch-based approach since the code has to handle a small set of nested grids covering areas of interest while the tree-based approach requires tree navigation methods such as father/neighbor/son fetching, which makes cache and memory access difficult to optimize.
Since the refinement strategy is local in the tree-based approach and follows more closely the hydrodynamical flow (discontinuities and shocks) throughout its evolution, the computational cost is far more optimized than in the patch-based approach.

In `RAMSES` , the AMR structure is based on an *octree* where each cell or *oct* is refined by two son cells along each dimension (in 3D, $2^3 = 8$ son cells ; in 2D, $2^2 = 4$ son cells) as shown in fig. 3.1.

Parallelisation and domain decomposition

`RAMSES` is parallelized with the Message Passing Interface (MPI) library and has been designed to run on more than 16,000 CPUs. Each processor handles a computational task related to a subvolume of the simulation box called *domain*. Several domain decomposition methods are implemented in `RAMSES` . The de-

---

[2] `http://lca.ucsd.edu/projects/enzo`

[3] `http://flash.uchicago.edu/site/flashcode/`

fault method is one of the most commonly used in computer science and is based on the *Peano-Hilbert space-filling curve* (Peano, 1890; Hilbert, 1891). This 1D-curve maps the entire n-dimensional simulation domain and lets the code divide the computational task into several well-balanced processes.

An example of this Peano-Hilbert curve decomposition is shown in fig. 3.3 for a 2D (16×16) grid divided between 5 processes.

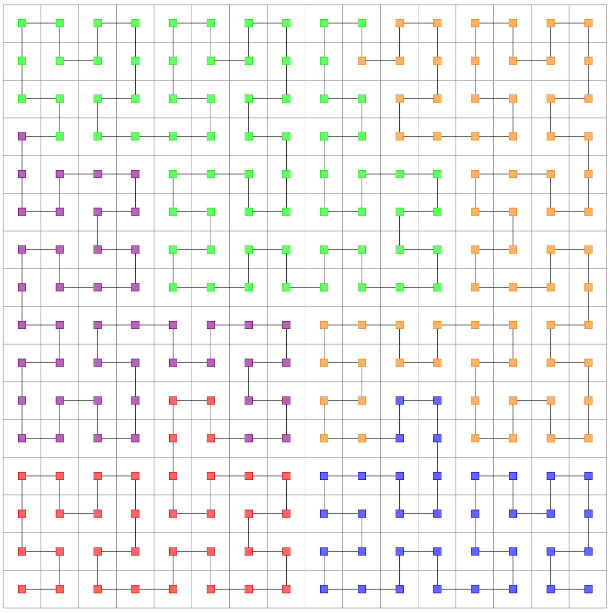

Figure 3.3: Hilbert curve domain decomposition example for a 16×16 grid using 5 processes in respectively, red, purple, green, orange and blue.

Adaptative time-stepping

In any eulerian code, to insure the convergence of numerical schemes when solving the advection of the flow on a grid where the cell size is Δx and the flow velocity is v, one must satisfied the so-called CFL condition (Courant, Friedrichs, and Lewy, 1967):

$$\frac{v\Delta t}{\Delta x} < C < 1 \tag{3.1}$$

As shown in fig. 3.1 of the `RAMSES` octree structure, cell sizes of different AMR levels l satisfy $\Delta x^{l+1} = \Delta x^{l}/2$. Consequently, the CFL condition implies $\Delta t^{l+1} = \Delta t^{l}/2$: both spatial resolution and timesteps are adaptative. While fine refinement levels (small scales) often dictates the most stringent CFL condition (shorter timescales) but only fill a small fraction of the simulation box volume, updating the whole grid every fine timestep is not only too costly but also unnecessary. That is why `RAMSES` , as most AMR codes do, uses *level subcycling* to update the grids of each AMR level according to its own timestep. The update of the whole AMR grid is not done more often than needed and fine and coarse levels are synchronized every other fine timestep, as shown in fig. 3.4.

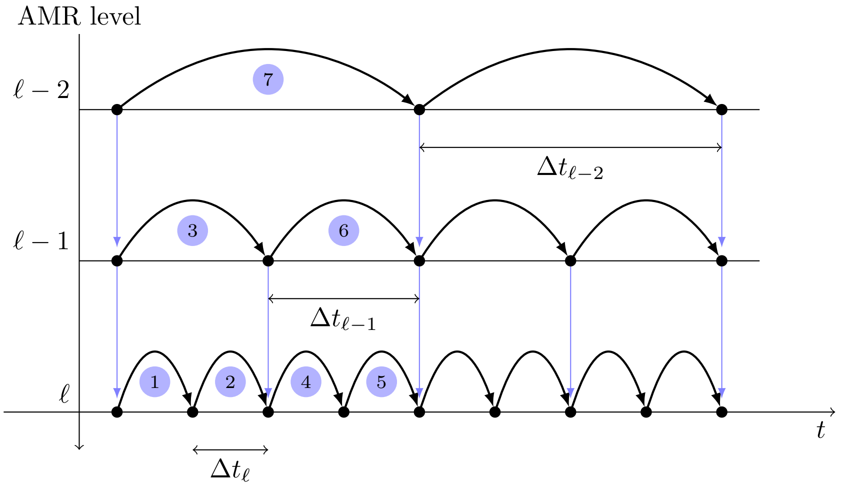

Figure 3.4: (from Guillet, 2010) Level subcycling as performed in `RAMSES` , showing the hierarchy of timesteps for a sequence of AMR levels. The arrows represent a full update at a given level. The levels are updated in the order specified by the blue numbered labels.

Grid refinement criteria

At the opposite of *patch-based* AMR techniques, `RAMSES` uses a *cell-based* (local) refinement strategy. To increase the spatial resolution only where required, several refinement criteria, based on velocity/pressure gradients,on the density or on the Jeans length (Truelove et al., 1997) have been implemented.

The refinement condition used in this work is the density criterion: for each AMR cell, the gas mass m_{gas} and the number of collisionless particles n_{p} contained in each cell are evaluated. The cell is refined if it satisfies one of the conditions:

$$m_{\text{gas}} = \rho_{\text{gas}}(\Delta x^{l})^{\text{ndim}} \geq n^{l}_{\text{refine}} \times M_{\text{sph}} \tag{3.2a}$$

$$n_{\text{p}} \geq n^{l}_{\text{refine}} \tag{3.2b}$$

In 3D `RAMSES` simulations, n^{l}_{refine} is often set to 8 for each AMR level so that each cell contains at least one collisionless particle or M_{sph} of gas mass. An illustration of such a refinement strategy is shown in fig. 3.5. A galactic gaseous disk from an Antennæ -like merger simulation (NGC4038 disk here) is fragmenting shortly after a pericentric passage (see chap. 4). The refinement levels of the AMR grid follow closely the gas density distribution.

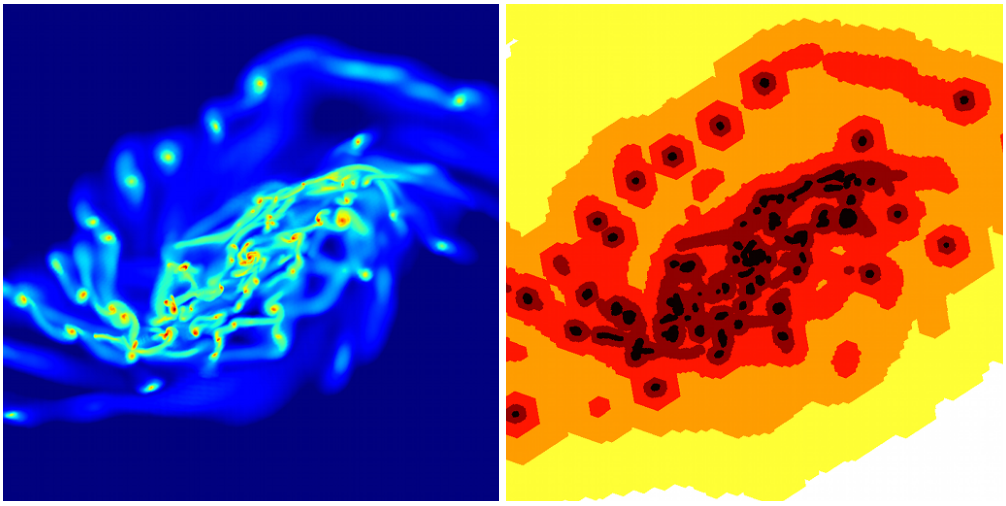

Figure 3.5: Face-on view of the NGC4038 fragmenting disk. (left) Density map. (right) AMR levels of refinement from $l = 9$ (white) to $l = 14$ (black).

3.1.2 Collisionless particle physics and self-gravity in `RAMSES` grids

Cold dark matter and stars are modeled as collisionless massive particles in `RAMSES` . These particles are only sensitive to the gravitational interaction. To compute their dynamical evolution, the *Poisson equation* needs to be solved.

$$\text{Poisson equation} \quad \Delta\Phi = 4\pi G(\rho_{\text{gas}} + \rho_{\text{particles}}) \tag{3.3}$$

$$\text{Gravitational force} \quad \dot{\mathbf{v}} = -\nabla\Phi \tag{3.4}$$

The computation of the gravitational potential field Φ first requires to know the density field on the AMR grid. The projection of the particle masses onto the grid is made according to the so-called *particle-mesh* (PM) method. Among various existing projection kernels, `RAMSES` implements the most commonly used which is the *cloud-in-cell* (CIC) kernel (see Hockney and Eastwood, 1981) as shown in fig. 3.6.

Once the collisionless matter contribution to the density field is computed, it is added to the gas density field and `RAMSES` can determine Φ using one of the various implemented Poisson solvers. In addition to the original Gauss-Seidel-based solver presented in Teyssier (2002), an optimized *multigrid solver* has recently been implemented in `RAMSES` (Guillet and Teyssier, 2011).

The gravitational force $\mathbf{g}^n = -\nabla\Phi^n$ at a given time t^n is computed on the grid by differentiating the potential Φ with a 5-points finite difference scheme and then interpolated at the particle positions $\mathbf{x}_p^n$ using the same CIC projection kernel. Finally, the particle velocities and positions are updated by a second-order predictor-corrector scheme (Teyssier, 2002) :

$$\mathbf{v}_p^{n+1/2} = \mathbf{v}_p^n - \nabla\Phi^n \Delta t^n/2 \tag{3.5a}$$

$$\mathbf{x}_p^{n+1} = \mathbf{x}_p^n + \mathbf{v}_p^{n+1/2}\Delta t^n \tag{3.5b}$$

$$\mathbf{v}_p^{n+1} = \mathbf{v}_p^{n+1/2} - \nabla\Phi^{n+1}\Delta t^n/2 \tag{3.5c}$$

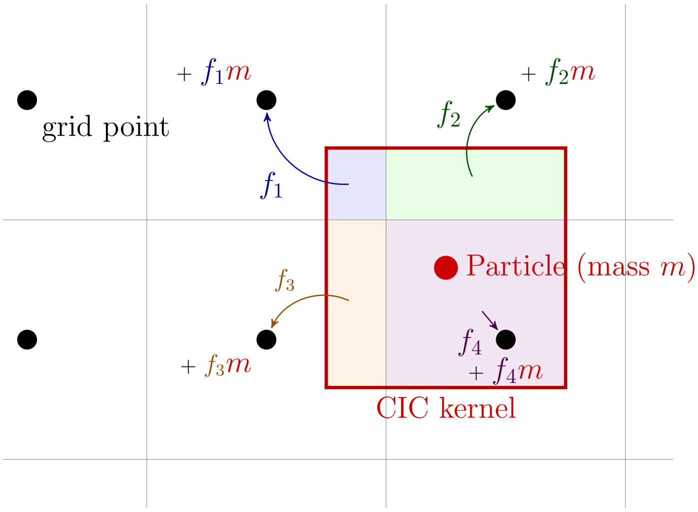

Figure 3.6: Cloud-in-cell interpolation scheme

3.1.3 Physics of the interstellar medium

The Eulerian approach for self-gravitating flows

Hydrodynamical processes are governed by the Euler equations. In astrophysical systems simulated with RAMSES , compressible inviscid self-gravitating flows are modeled as an ideal fluid insensitive to heat transfer. Such a fluid is described by the following conservation equations :

$$\frac{\partial \rho}{\partial t} + \nabla \cdot (\rho \mathbf{v}) = s_m \quad \text{(mass)} \tag{3.6a}$$

$$\frac{\partial (\rho \mathbf{v})}{\partial t} + \nabla \cdot (\rho \mathbf{v} \otimes \mathbf{v}) + \nabla P = -\rho \nabla \Phi + \mathbf{s_p} \quad \text{(momentum)} \tag{3.6b}$$

$$\frac{\partial E}{\partial t} + \nabla \cdot ((E+P)\,\mathbf{v}) = -\rho \mathbf{v} \cdot \nabla \Phi + s_e \quad \text{(energy)} \tag{3.6c}$$

where Φ is the gravitational potential (see eq. 3.3), ρ is the fluid density, $\mathbf{v}$ is the local Eulerian fluid velocity, P is the pressure and the total energy E is obtained from local quantities (e is the local specific internal energy) as:

$$E = \rho\left(\frac{1}{2}\mathbf{v}^2 + e\right), \tag{3.7}$$

To determine a unique solution to this equation system, a closing relation is needed, given by the equation-of-state (EOS) of the gas :

$$P = \frac{\rho k_B T}{\mu m_H} = \rho\left(\gamma - 1\right) e, \tag{3.8}$$

where $\gamma = C_p/C_v$ is the gas adiabatic index.
Equations 3.6 with vanishing source terms may be cast into a so-called *conservative form*:

$$\frac{\partial \mathbf{U}}{\partial t} + \nabla \cdot \mathbf{F}\left(\mathbf{U}\right) = 0. \tag{3.9}$$

where $\mathbf{U} = (\rho, \rho\mathbf{v}, E)$ corresponds to the *conservative state vector* and $\mathbf{F}$ corresponds to the variable fluxes at the cell boundaries. Given a discretization of a 1D space $\{x_i\}$, eq. 3.9 writes:

$$\frac{\mathrm{d}U_i}{\mathrm{d}t} + \frac{1}{x_{i+1} - x_i}\left[F(U)_{|x_{i+1}} - F(U)_{|x_i}\right] = 0 \tag{3.10}$$

where U_i stands for the average value of $U(x,t)$ in the finite volume $[x_i, x_{i+1}]$ also called *cell*:

$$U_i(t) = \frac{1}{x_{i+1} - x_i}\int_{x_i}^{x_{i+1}} U(t,x)dx \tag{3.11}$$

To determine the values of the fluxes $F_{i-1/2}$ and $F_{i+1/2}$ at the interfaces of the cell i, one needs to solve the (discontinuity) *Riemann problem* at each interface. Initially, each interface separates a *left state* $U^L_{i+1/2} = U_i$ and a *right state* $U^R_{i+1/2} = U_{i+1}$. The computation of the final state $U^*_{i+1/2}$ at the interface solves the Riemann problem and allows us to obtain the values for the fluxes at the cell boundaries.

There are different interpolation methods to compute these two initial states at the interface. First-order constant interpolation in the cell was first proposed in Godunov (1959) (Piecewise Constant Method). This first-order spatial accuracy scheme is particularly diffusive and does not resolve shocks well. Higher-order reconstruction of the solution $U(x,t)$ within the cell called MUSCL (Monotone Upstream-centered Schemes for Conservation Laws) scheme has been introduced by van Leer (1979), who proposed a piecewise-linear interpolation (Piecewise Linear Method). This method is much less diffusive, sports second-order spatial accuracy but requires to be coupled to *slope limiters* to avoid spurious oscillations and keep the scheme stable. Finally, a third-order spatial accuracy interpolation called Piecewise Parabolic Method (PPM) was proposed by Colella and Woodward (1984).

`RAMSES` uses the (second-order) MUSCL scheme together with the *minmod* or the *moncen* slope limiter. Nowadays, this high-order Godunov scheme, coupled with the AMR structure of RAMSES and sharp Riemann solvers is proved to be an efficient method to capture discontinuities within only a few cells (e.g. Teyssier, 2002; Fromang et al., 2006; Ziegler, 2005; Agertz et al., 2007). Several Riemann solvers have been implemented for hydrodynamics and MHD in RAMSES : HLL (Harten–Lax–von Leer), HLLC (HLL Contact), acoustic and a Lax-Friedrich solver. The choice of the Riemann solver is a critical one, as it may dramatically influence the numerical dissipation of the scheme.

In astrophysical applications :

- the local mass source term s_m may be caused by star formation processes which deplete the gas ($s_m = -\frac{\mathrm{d}\rho_*}{\mathrm{d}t}$).
- kinetic feedback during supernovæ explosions can impact the local momentum source term $\mathbf{s_p}$.
- the local energy density source term s_e is caused by heating/cooling processes ($s_e = n_\mathrm{H}^2(\mathcal{H} - \Lambda)$, Gnat and Sternberg 2007).

Star formation

Star formation is the result of a very-small scale gravitational collapse inside a cold molecular gas cloud. The collapsing timescale of a density perturbation in a pressureless fluid is knwon as the *free-fall time*:

$$\rho^{-1/2} \propto t_\mathrm{ff} = \sqrt{\frac{3\pi}{32G\rho}} \qquad \text{(3D homogeneous sphere)} \tag{3.12a}$$

$$= \sqrt{\frac{\pi}{G\rho}} \qquad \text{(infinite 1D cosine perturbation)} \tag{3.12b}$$

Since the physical scales of star formation are so far, even with AMR techniques, impossible to resolve in cosmological or even galactic scale simulations, RAMSES implements this physical ingredient as a subgrid recipe. The source term s_m in eq. 3.6a is set to the opposite of the star formation rate:

$$\frac{\partial\rho}{\partial t} + \nabla\cdot(\rho\mathbf{v}) = s_m = -\frac{\mathrm{d}\rho_*}{\mathrm{d}t} \tag{3.13}$$

In some cells of the AMR grid, the gas reservoir is therefore depleted and the corresponding mass is converted into new star particles. The *3D local* star formation rate follows :

$$\frac{\mathrm{d}\rho_*}{\mathrm{d}t} = \frac{\rho}{t_*} \;\; (\rho \geq \rho_0) \tag{3.14a}$$

$$= 0 \;\; (\rho < \rho_0) \tag{3.14b}$$

where ρ is the local gas density, t_* is the local star formation timescale and ρ_0 the gas density threshold above which star formation is enabled. The star formation timescale is assumed to be proportional to the local free-fall time t_{ff} of the gas :

$$t_* = \frac{t_{\mathrm{ff}}}{\epsilon} \tag{3.15}$$

where ϵ is the star formation efficiency.

In `RAMSES` , this star particle creation is a *random process* (Katz, 1992). Every time step Δt, in each leaf cell of the AMR grid where $\rho \geq \rho_0$, a stellar mass number n is computed where n follow a *Poisson's law* :

$$P(n = N) = \frac{\lambda^N}{N!} e^{-\lambda} \tag{3.16}$$

where the mean value λ is taken as :

$$\lambda =< n >= \left(\frac{\rho \Delta x^{\mathrm{ndim}}}{M_*} \right) \frac{\Delta t}{t_*} \tag{3.17}$$

For non-zero values of n, a new particle is created with a mass $m_* = n M_*$.

From eq. 3.14a, 3.15 and 3.12 we end up with :

$$\frac{\mathrm{d}\rho_*}{\mathrm{d}t} \propto \rho^{1.5} \tag{3.18}$$

The local star formation rate scales with the gas density to the power $\alpha = 1.5$, consistently with the large scale gas to star formation relations in observed galaxies (see sec. 2.3.3; Kennicutt 1998; Bigiel et al. 2008; Daddi et al. 2010a).

Heating/cooling processes

The radiative cooling due to atomic processes in the gas is modeled in `RAMSES` by a cooling function Λ. The UV background heating term coming from quasars and massive young stars is modeled by a heating function which follows Haardt and Madau (1996). The energy density source term s_e (see eq. 3.6c) therefore writes:

$$s_e = n_{\mathrm{H}}^2 \times (\mathcal{H} - \Lambda) \tag{3.19}$$

This energy density variation rate of the ISM s_e is tabulated beforehand into a lookup table for a set of (ρ, T, Z) values. Using this lookup table, the local cooling rate is interpolated for each AMR cell during the simulation.

Supernovæ feedback

The explosions of massive stars into supernovæ produce blast waves which coalesce into a large-scale feature called *superbubble*. The limited spatial resolution in cosmological or galactic-scale simulations is not sufficient to capture the blast wave following the explosion. However, these large-scale superbubbles can be resolved. `RAMSES` implements a supernova feedback recipe presented in Dubois and Teyssier (2008) to model these structures.

The propagation radius of a blast wave $\Delta t = 1$ Myr after the supernova explosion of energy $E_{\mathrm{SN}} = 10^{51}$ ergs in an interstellar medium of density $\rho = 0.1$ H/cc is given by:

$$r_{\mathrm{SN}} \simeq \left(\frac{E_{\mathrm{SN}}\Delta t^2}{\rho}\right)^{1/5} \simeq 100 \text{ pc} \tag{3.20}$$

The feedback scheme injects kinetic energy in bubbles of radius $r_{\mathrm{SN}} \sim 100 - 200$ pc, similar to turbulent forcing at scale r_{SN} . In practice, the energy is injected as a Sedov blast wave into the flow variables, and by converting stellar mass into *debris* particles.

3.2 This work: additional `RAMSES` module development

A small part of this thesis has been spent on the development of additional modules in `RAMSES` . These modules have been designed for the specific purpose of galaxy mergers and interstellar medium modelisation.

3.2.1 The merger module

The default version of `RAMSES` did not provide an easy way to set up galaxy simulations. The aim of the *merger* module is to set up isolated galaxy or galaxy merger initial conditions with few efforts from the user.

Let us assume one already has a set of initial condition files containing the positions, masses and velocities of the collisionless particles (dark matter, stellar disk and bulge) for various galactic models. Each galaxy is centered on the axes origin $(x = 0, y = 0, z = 0)$ and rotating around the z-axis. For each galactic model, one has the circular velocity profile

$$V_{\mathrm{circ}}(r) = \sqrt{\frac{GM(<r)}{r}} \tag{3.21}$$

stored in an ascii file following the format: column #1→ radius in pc, column #2→ circular velocity in km.s^{-1}.

If one wants to set up an isolated galaxy or a galaxy merger simulation using those galactic models while adding a gas disk in each galaxy, one must edit its namelist configuration file and define some parameters in a `&MERGER_PARAMS` block. These parameters are described in the tab. 3.1.

Variable name, syntax and default value	**Description**
`gal_center1=0.,0.,0.` `gal_center2=0.,0.,0.`	Galaxy centers coordinates, given in code units (like the particles coordinates in the `ic_part` file). the default value is the center of the simulation box. For isolated galaxy runs, set the `gal_center2` to twice the `boxlen` parameter.
`gal_axis1=0.,0.,1.` `gal_axis2=0.,0.,1.`	Galaxy rotation axis vectors. The default value is the z-axis of the AMR grid.
`Vgal1=0.,0.,0.` `Vgal2=0.,0.,0.`	Galaxy velocity vectors, given in km/s.
`ic_part_file_gal1='ic_part1'` `ic_part_file_gal2='ic_part2'`	IC particle ascii files for the two galaxies, to be found in the `initfile` directory.
`Vcirc_dat_file1='Vcirc1.dat'` `Vcirc_dat_file2='Vcirc2.dat'`	Circular velocity profile ascii file paths for the two galaxies. Each file must contain 2 columns: the first column are radii (in pc) and the second the circular velocities (in km/s).
`Mgas_disk1=1.0D2` `Mgas_disk2=1.0D2`	Galactic gas disk masses, in $10^9\ M_\odot$. Must satisfy $M_{\text{gas1}} \geq M_{\text{gas2}}$. For isolated galaxy runs, set $M_{\text{gas2}} = 0.0$.
`rad_profile='exponential'`	Radial density profile of the gaseous disks (`'exponential'` or `'Toomre'`).
`z_profile='gaussian'`	Vertical density profile of the gaseous disks (`'exponential'` or `'gaussian'`).
`typ_radius1=3.0D0` `typ_radius2=3.0D0`	Gasous disk radial scale length r_0, in kpc.
`cut_radius1=10.0D0` `cut_radius2=10.0D0`	Gaseous disk cut radius r_{max}, in kpc.
`typ_height1=1.5D-1` `typ_height2=1.5D-1`	Gasesous disk vertical scale length z_0, in kpc.
`cut_height1=4.0D-1` `cut_height2=4.0D-1`	Gaseous disk cut height z_{max}, in kpc.
`IG_density_factor=1.0D-5`	Density contrast δ_ρ between the extragalactic gas and the outer rim of the galactic disk.

Table 3.1: `&MERGER_PARAMS` block parameters description in the *merger* module

Gas disk density profiles

Several gas density profiles are implemented in the merger module. The gas density cylindrical profile is sampled during the initialization of the AMR grid.

$$\rho(r,z) = \rho_0 f(r) g(z) \text{ where } r \leq r_{\text{max}} \text{ and } |z| \leq z_{\text{max}} \tag{3.22a}$$

$$= \rho_{\text{ex}} \text{ elsewhere} \tag{3.22b}$$

where

$$f(r) = \begin{cases} 1/\sqrt{1+r^2/r_0^2} & \text{(Toomre profile)} \\ \exp(-r/r_0) & \text{(exponential radial profile)} \end{cases} \tag{3.23a}$$

$$g(z) = \begin{cases} \exp(-1/2 \times (z^2/z_0)^2) & \text{(gaussian profile)} \\ \exp(-|z|/z_0) & \text{(exponential vertical profile)} \end{cases} \tag{3.23b}$$

The extragalactic gas velocity is set to the velocity of the closest galaxy and its density is set to a uniform value of :

$$\rho_{\text{ex}} = \delta_\rho \times \rho(r = r_{\text{max}}, z = z_{\text{max}}) \tag{3.24}$$

where δ_ρ is the user-defined density contrast and $\rho(r,z)$ the analytical gas density profile of the closest galaxy.

The central density ρ_0 is chosen so that the analytical enclosed mass is equal to M_{gas}:

$$\rho_0 = M_{\text{gas}} / \left[\left(\int_0^{r_{\text{max}}} 2\pi r f(r) \mathrm{d}r \right) \left(\int_{-z_{\text{max}}}^{z_{\text{max}}} g(z) \mathrm{d}z \right) \right] \tag{3.25}$$

Rotation-supported gas disk

From the circular velocity profile $V_{\text{circ}}(r)$ provided by the user, the gaseous disk is initialized at rotation equilibrium. This equilibrium is caracterized by a rotation velocity $\mathbf{V}_{\text{rot}}(r,\theta,z) = V_{\text{rot}}(r)\mathbf{u}_\theta$ that exactly compensates the gravitational acceleration plus the thermal and turbulent pressure accelerations.

$$\mathbf{a} = \frac{\mathrm{d}\mathbf{V}_{\text{rot}}}{\mathrm{d}t} = -\frac{{\mathbf{V}_{\text{rot}}}^2}{r}\mathbf{u_r} = \left[-\frac{GM(<r)}{r^2} - \frac{1}{\rho}\nabla P \cdot \mathbf{u_r} + \frac{3\sigma^2}{r} \right] \mathbf{u_r} \tag{3.26}$$

If we assume the gas velocity dispersion $\sigma = c_{\text{s}} = \sqrt{k_{\text{B}}T/(\mu m_{\text{H}})}$ where T is the `T2_star` namelist parameter from the `&PHYSICS_PARAMS` block, we obtain from eq. 3.21, eq. 3.23 and eq. 3.26

$$V_{\text{rot}}^2(r) = V_{\text{circ}}^2(r) + \frac{r c_{\text{s}}^2}{\rho}(\nabla\rho \cdot \mathbf{u_r}) - 3c_{\text{s}}^2 \tag{3.27}$$

Within the disk, the gas velocity field is therefore initialized to

$$\mathbf{V}_{\mathrm{rot}}(r) = \begin{cases} \sqrt{V_{\mathrm{circ}}^2(r) - \frac{r}{r_0}c_{\mathrm{s}}^2 - 3c_{\mathrm{s}}^2}\;\mathbf{u}_\theta & \text{(exponential disk)} \\ \sqrt{V_{\mathrm{circ}}^2(r) - \frac{r^2}{r^2+r_0^2}c_{\mathrm{s}}^2 - 3c_{\mathrm{s}}^2}\;\mathbf{u}_\theta & \text{(Toomre disk)} \end{cases} \tag{3.28a}$$

Galaxy Ro(c)ks (ROtated/Kicked/Shifted) !

Using the parameters from tab. 3.1, geometrical transformations are applied to both collisionless particles and hydrodynamical density/velocity fields. Each galaxy is rotated according to its new user-defined rotation axis vector and kicked so that its mean velocity vector satisfies the user-defined value. Finally, it is shifted at its new center coordinates.

With a single set of galactic models, the merger module let the `RAMSES` user explore many collision models at will. It has been extensively used in this thesis work (see chapter 4 and Teyssier, Chapon, and Bournaud 2010, chapter 5 and Chapon et al. 2011) and more broadly by the `RAMSES` community (Bournaud et al., 2011, 2010; Powell et al., 2011a,b).

3.2.2 The equation-of-state module

To model properly the thermodynamical behavior of the interstellar medium, one should solve the energy equation (eq. 3.6c) to capture the dynamical heating/cooling processes, which are strongly dependant on the metal enrichment of the ISM (Gnat and Sternberg, 2007). This can be done in `RAMSES` simulations by enabling the *cooling* modules. The resolution of eq. 3.6c comes with greater computational cost: the cooling time scales completely governs the numerical timestep $\Delta t \sim 10^{-3}$ Myr instead of $\Delta t \sim 1$ Myr in the case of galactic scale simulations without cooling.

I implemented an *EOS module* to provide a simpler thermodynamical model for the ISM: the gas temperature is given by a fixed *equation-of-state* $T = T(\rho)$ corresponding to the equilibrium between cooling and heating processes. Since we mimic the heating/cooling source term in the energy equation, this approach is not strictly speaking an equation-of-state. The dispersion relation with heating/cooling source terms would yield an imaginary sound speed value. This method rather comes down to the assumption that the cooling time $dt_{\mathrm{cool}} = 0$ or that the gas, once its density is slightly perturbed, immediately falls to its new equilibrium temperature.

This methods leads to a $\sim 30\%$ computational time reduction compared to the resolution of the energy equation but prevents shock heating, which is believed to be an important mechanism in the virialization process of the gas during halo formation. Consequently, this thermodynamical model is not to be used in cosmological simulations but gives the possibility to invest on higher resolution galaxy simulations to capture the small-scale turbulent structure of the ISM. The parameters of the EOS module are described in tab. 3.2.

Variable name, syntax and default value	**Description**
`eos_type='isothermal'`	`'isothermal'`, `'pseudo_cooling'` or `'gamma_support'`.
`nH_H_cc_threshold=10.0D0`	For the `'gamma_support'` mode only. Gas density threshold $\rho_{\rm th}(\ \mathrm{H/cc})$ above which the adiabatic index becomes $\gamma_{\rm high}$ given by the `gamma_high_rho` parameter.
`gamma_high_rho=1.666D0`	For the `'gamma_support'` mode only. High density gas adiabatic index $\gamma_{\rm high}$.
`max_used_level=levelmax`	Effective maximum AMR level corresponding to the smallest cells present in the grid. The default value is equal to the `levelmax` parameter from the `&AMR_PARAMS` block. Parameter used to set the Jeans pressure floor to prevent numerical fragmentation of the ISM.

Table 3.2: `&EOS_PARAMS` block parameters description in the *Equation-Of-State* module

In the EOS module, the low-density gas is modeled as follow:

- Diffuse gas ($\rho < 10^{-3}\ \mathrm{H/cc}$): the thermodynamical behavior of the diffuse phase of cold cosmological gas together with the hot virialised gas in the dark matter halo (see fig. 1.5) can be well approximated by a $\gamma = 5/3$ polytropic equation-of-state:

$$\frac{T}{\mu} = 4 \times 10^{6} \left(\frac{\rho}{10^{-3}\ \mathrm{H/cc}}\right)^{5/3-1}\ \mathrm{K} \tag{3.29}$$

- Isothermal gaseous disk ($\rho > 10^{-3}\ \mathrm{H/cc}$): the gaseous galactic disk lies in this density range, where it is assumed to be optically thin so it can be heated by UV background radiation. The equilibrium beetween heating and cooling processes yields a quasi-isothermal gas, the temperature of which is $T_{\rm iso}$ given by the `T2_star` parameter:

$$\frac{T}{\mu} = T_{\rm iso} \sim 10^{4}\ \mathrm{K} \tag{3.30}$$

For the high-density gas, three different modes have been implemented. The default mode `isothermal` sets the gas in an isothermal state as previously explained. The two other modes, `pseudo_cooling` and `gamma_support`, bring a modified equation-of-state at high density and are described in details below.

Pseudo-cooling mode

Above a gas density of 0.3 H/cc, the ISM is no longer isothermal, as shown in fig. 3.7. The gas temperature is fitted with a $\gamma = 1/2$ equation-of-state:

$$\frac{T}{\mu} = T_{\mathrm{iso}} \times \left(\frac{\rho}{0.3\ \mathrm{H/cc}}\right)^{1/2-1} \mathrm{K} \tag{3.31}$$

In this regime, the gas is more unstable than an isothermal gas and simulations naturally produce a cold clumpy and turbulent phase in the ISM (see chapter 4 and Teyssier, Chapon, and Bournaud 2010; Bournaud et al. 2010). The gas velocity distribution, dispersion and power spectrum observed in the Large Magellanic Cloud (LMC) (Block et al., 2010) are well reproduced over a wide scale range in *pseudo-cooled* numerical simulations (Bournaud et al., 2010).

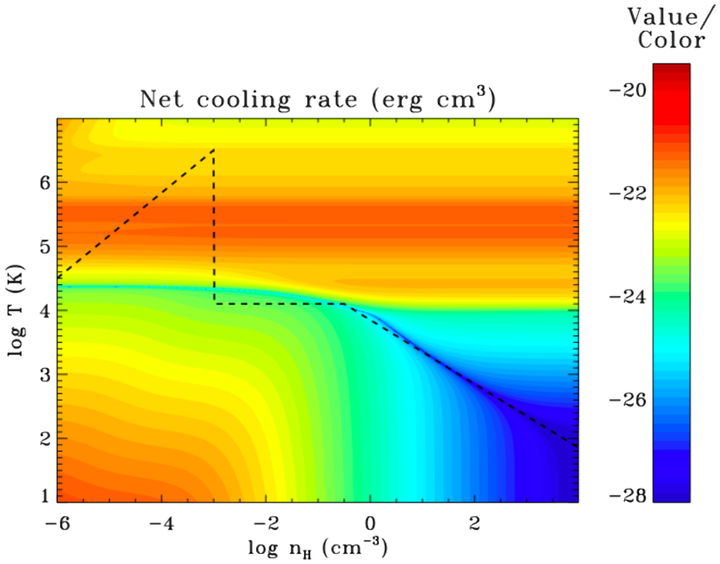

Figure 3.7: Net heating/cooling rate (ρ, T) diagram for a $Z = Z_\odot/3$ gas. The black dashed line fitting the blueish equilibrium valley corresponds to the *pseudo-cooling* equation-of-state.

This model doesn't take into account *self-shielding* and *UV heating from young OB stars*. In molecular clouds, the assumption that the gas is optically thin is no longer valid: the gas can shield the cloud core from the UV background, allowing the gas to cool down enough to form H_2 molecules. Thus, the heating might be shut out of this kind of region and the equilibrium temperature could be even colder. The UV radiation from young OB stars could heat the gas in star forming regions and compensates this effect. OB stars would play the role of *internal* heating sources when the external one is prevented from entering.

High density polytropic mode

The polytropic equation-of-state for high density gas has been previously used by Dubois and Teyssier (2008); Schaye and Dalla Vecchia (2008):

$$T = T_0 \left(\frac{\rho}{\rho_0}\right)^{\gamma_{\mathrm{eff}}-1} \tag{3.32}$$

where the effective adiabatic index γ_{eff} can take values in the range $[0.7;2.3]$ (Springel and Hernquist, 2003).

This model is enabled by setting `eos_type='gamma_support'`. The user choose its own adiabatic index above a given density threshold:

$$\frac{T}{\mu} = T_{\mathrm{iso}} \times \left(\frac{\rho}{\rho_{\mathrm{th}}}\right)^{\gamma_{\mathrm{high}}-1} \tag{3.33}$$

where $\rho_{\mathrm{th}}(\ \mathrm{H/cc})$ is given in by `nH_H_cc` and γ_{high} by the `gamma_high_rho` namelist parameter. This mode has been used in this work (see chapter 5) with values of $\gamma_{\mathrm{high}} \in \{7/5, 5/3\}$ to mimic the feedback from Active Galactic Nuclei (AGN) in the nuclear region of galaxies (Spaans and Silk, 2000).

Numerical fragmentation, resolution and Jeans polytrope

The various thermodynamical modes presented before come from purely physical considerations. But another ingredient called *numerical fragmentation* absolutely needs to be considered whatever the chosen equation-of-state. To resolve all the physical scale lengths, an ideal numerical simulation should have infinite resolution and therefore requires infinite time and memory to run. Due to technical limitations, numerical simulations are bound to use limited spatial resolution and amount of memory. Consequently, the smallest physical scales are not resolved, and in many astrophysical applications, these small scales are governed by the *Jeans length* (Jeans, 1902):

$$\lambda_{\mathrm{Jeans}} = c_s \times t_{\mathrm{ff}} \tag{3.34}$$

The Jeans length corresponds to the collapsing scale length of a sound wave pertubation. t_{ff} is the free-fall time (eq. 3.12) and the sound speed can be written

$$c_s = \sqrt{\frac{\gamma P}{\rho}} \tag{3.35}$$

Truelove et al. (1997) demonstrated that the Jeans length needs to be resolved by at least a few cells to prevent artificial fragmentation of a self-gravitating gas. Wherever this so-called *Truelove criterion* is not satisfied, the grid needs to be refined. But the grid cannot be refined indefinitely. Two different approaches are considered to prevent artificial fragmentation in the most refined cells: *sink particles* and pressure support. The first one, proposed by Bate et al. (1995), turns any small gas cloud of gas where the Jeans length is no longer resolved into a collisionless "sink" accreting particle to capture smaller scale physics. The second method, implemented in the EOS module, artificially increases the Jeans length so that the Jeans length is always resolved by 4 cells in the finest resolution level:

$$4\Delta x_{\rm min} \leq \lambda_{\rm Jeans} \tag{3.36}$$

This technique, introduced in a different context by Machacek et al. (2001), efficiently prevents the formation of spuriously fragmenting clumps in galaxy formation simulations (Robertson and Kravtsov, 2008; Agertz et al., 2009b).

From eq. 3.12, 3.34 and 3.36, we obtain:

$$P \geq P_{\rm Jeans}(\Delta x_{\rm min}) = \frac{16G}{\pi\gamma}(\Delta x_{\rm min})^2\rho^2 = K\rho^2 \tag{3.37}$$

A $\gamma = 2$ polytropic equation-of-state, depending on the spatial resolution limit $P_{\rm Jeans}(\Delta x_{\rm min})$ is set as a pressure floor, as shown in fig. 3.8 in the case of pseudo-cooling equation-of-state. The typical density and temperature at which the pressure floor dominates are

$$\rho_{\rm Jeans} \simeq 6 \times \left(\frac{\Delta x_{\rm min}}{100\ \rm pc}\right)^{-4/3}\ \rm H/cc \tag{3.38a}$$

$$T_{\rm Jeans} \simeq T(\rho_{\rm Jeans}) \simeq 2500 \times \left(\frac{\Delta x_{\rm min}}{100\rm pc}\right)^{2/3}\ \rm K \tag{3.38b}$$

Then the gas mass resolution writes

$$M_{\rm res} = \rho_{\rm Jeans}(\Delta x_{\rm min})^3 \simeq 1.9 \times 10^5 \left(\frac{\Delta x_{\rm min}}{100\ \rm pc}\right)^{5/3}\ M_\odot \tag{3.39}$$

The gas mass resolution decreases by an order of magnitude every other AMR level ($(2^2)^{5/3} \simeq 10$). This pressure floor insures that the Jeans criterion is satisfied in the most refined cells of the AMR grid. To resolve the Jeans length by at least 4 cells at every AMR level, the user has two options:

- Use the Jeans length-based grid refinement strategy: set the `jeans_refine` parameter from the `&REFINE_PARAMS` block to 4, for every AMR level. This technique has been proved very costly in galaxy merger simulations due to rarefaction waves after pericentric passages. In some diffuse regions,

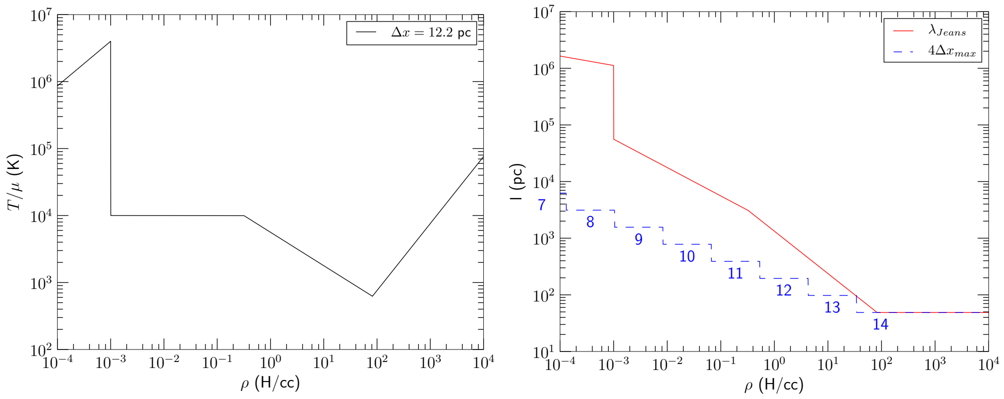

Figure 3.8: Pseudo-cooling equation-of-state for a gas with maximum spatial resolution of $\Delta x = 12$ pc. (left) Temperature as a function of gas density. The hot virialised gas corresponds to densities below 10^{-3} H/cc. The isothermal disk is set to 10^4 K. The pseudo-cooling temperature decreases down to $T(\rho = 90 \text{ H/cc}) \simeq 600$ K where the Jeans pressure floor dominates, preventing the gas from artificially fragmenting. (right) Jeans length and four times the cell max size as functions of gas density. The Jeans length is resolved by at least 4 cells at every AMR level of refinement as to prevent numerical fragmentation (Truelove et al., 1997).

negative numerical values of the gas density/pressure could arise. The local Jeans length would artificially decrease or even become zeroin these regions, which would lead to a costly while unnecessary refinement of the grid.

– Choose the $(M_{\mathrm{SPH}}, n_{\mathrm{refine}})$ parameters of the mass refinement criterion (eq. 3.2) consistently with the mass resolution according to the relation

$$M_{\mathrm{SPH}} \times n_{\mathrm{refine}} \lesssim 3.2 \times M_{\mathrm{res}} \tag{3.40}$$

An illustration of such a choice of parameters is presented in (fig. 3.8, right).

In the Jeans length definition, one should keep in mind that the free-fall time depends on the local matter density, and not only on the local gas density (eq. 3.14):

$$t_{\mathrm{ff}} \sim \rho^{-1/2} = (\rho_{\mathrm{gas}} + \rho_{\mathrm{stars}} + \rho_{\mathrm{DM}})^{-1/2} \tag{3.41}$$

In fig. 3.8 the Jeans length correponds to a situation with gas only. In a galactic disk with a dark matter halo and a stellar component, the physical Jeans length would be lower, especially in the regions where the stellar density dominates the gas density by an order of magnitude or so (> 100 pc scales).

At these particular scalelengths, the "gas only" Jeans length is greater than $4 \times \Delta x_{\mathrm{max}}$ by a factor of ~ 10 (see fig. 3.8, right, $l < 11$) due to the grid refinement criterion. This security factor means that numerical fragmentation would be prevented in the presence of stellar and dark matter components, should the free-fall time be 10 times lower, and should the total density ($\rho \propto t_{\mathrm{ff}}^{-2}$) be $10^2 = 100$ times higher than the gas density.

The EOS module has been used in a pseudo-cooling mode in an Antennæ -like merger simulation (see chapter 4 and Teyssier, Chapon, and Bournaud 2010) as well as in several studies of interacting galaxies with modelling of the the cold phase of the ISM (Bournaud et al., 2011; Powell et al., 2011a,b; Bournaud et al., 2010). The "pressure support" mode has been used in this work to mimic the AGN feedback in the nuclear region of merging galaxies (see chapter 5 and Chapon et al. 2011).

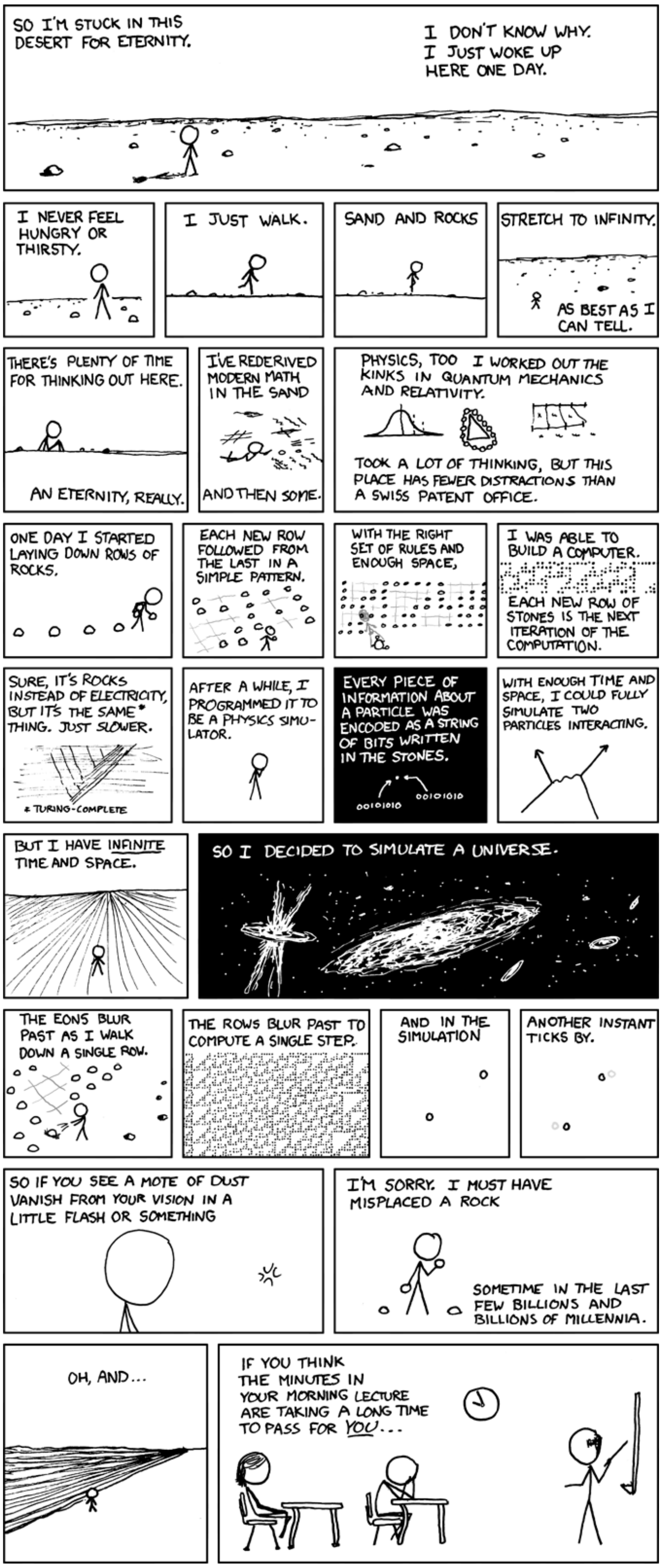
SO I'M STUCK IN THIS DESERT FOR ETERNITY.
I DON'T KNOW WHY. I JUST WOKE UP HERE ONE DAY.
I NEVER FEEL HUNGRY OR THIRSTY.
I JUST WALK.
SAND AND ROCKS
STRETCH TO INFINITY.
AS BEST AS I CAN TELL.
THERE'S PLENTY OF TIME FOR THINKING OUT HERE.
AN ETERNITY, REALLY.
I'VE REDERIVED MODERN MATH IN THE SAND
AND THEN SOME.
PHYSICS, TOO. I WORKED OUT THE KINKS IN QUANTUM MECHANICS AND RELATIVITY.
TOOK A LOT OF THINKING, BUT THIS PLACE HAS FEWER DISTRACTIONS THAN A SWISS PATENT OFFICE.
ONE DAY I STARTED LAYING DOWN ROWS OF ROCKS.
EACH NEW ROW FOLLOWED FROM THE LAST IN A SIMPLE PATTERN.
WITH THE RIGHT SET OF RULES AND ENOUGH SPACE,
I WAS ABLE TO BUILD A COMPUTER.
EACH NEW ROW OF STONES IS THE NEXT ITERATION OF THE COMPUTATION.
SURE, IT'S ROCKS INSTEAD OF ELECTRICITY, BUT IT'S THE SAME* THING. JUST SLOWER.
* TURING-COMPLETE
AFTER A WHILE, I PROGRAMMED IT TO BE A PHYSICS SIMULATOR.
EVERY PIECE OF INFORMATION ABOUT A PARTICLE WAS ENCODED AS A STRING OF BITS WRITTEN IN THE STONES.
00101010
00101010
WITH ENOUGH TIME AND SPACE, I COULD FULLY SIMULATE TWO PARTICLES INTERACTING.
BUT I HAVE INFINITE TIME AND SPACE.
SO I DECIDED TO SIMULATE A UNIVERSE.
THE EONS BLUR PAST AS I WALK DOWN A SINGLE ROW.
THE ROWS BLUR PAST TO COMPUTE A SINGLE STEP.
AND IN THE SIMULATION
ANOTHER INSTANT TICKS BY.
SO IF YOU SEE A MOTE OF DUST VANISH FROM YOUR VISION IN A LITTLE FLASH OR SOMETHING
I'M SORRY. I MUST HAVE MISPLACED A ROCK
SOMETIME IN THE LAST FEW BILLIONS AND BILLIONS OF MILLENNIA.
OH, AND...
IF YOU THINK THE MINUTES IN YOUR MORNING LECTURE ARE TAKING A LONG TIME TO PASS FOR YOU...

CHAPTER 4

The Antennæ system: a star formation laboratory

The Antennæ system (NGC4038/39) is the closest ongoing major merger we can observe and thus one of the most studied in the litterature, in both observational and numerical studies. To validate any theory on galaxy interaction relying on simulations, the Antennæ galaxies are therefore a choice laboratory to study merger-driven processes, and in particular star formation. Based on a hydrodynamical simulation of the Antennæ galaxy merger, the impact of the galaxy interaction on the gas dynamics and the star formation have been studied. The results presented in Teyssier, Chapon, and Bournaud (2010) are detailed in this chapter.

Figure 4.1: HST image of the central region of NGC4038/39, the Antennæ galaxies (credit: B. Whitmore).

4.1 The Antennæ galaxies (NGC4038/39)

4.1.1 Observations...

Based on different observational methods, the distance of the Antennæ galaxies have been estimated in the range $6 - 30$ Mpc (see e.g. Rubin et al., 1970; Whitmore and Schweizer, 1995; Fabbiano et al., 2001; Hibbard et al., 2001; Zezas and Fabbiano, 2002; Saviane et al., 2004) in the past decades. Until recently, the common adopted value for this distance was ~ 19.2 Mpc, based on recession velocity measurements Whitmore et al. (1999).

Using an observation of the SNIa explosion (SN 2007sr), Schweizer et al. (2008) found a distance of 22.3 ± 2.8 Mpc. While still debated, the estimation of this distance is a key point in every observational analysis as it is used to derive the sizes, masses and ages in the Antennæ system.

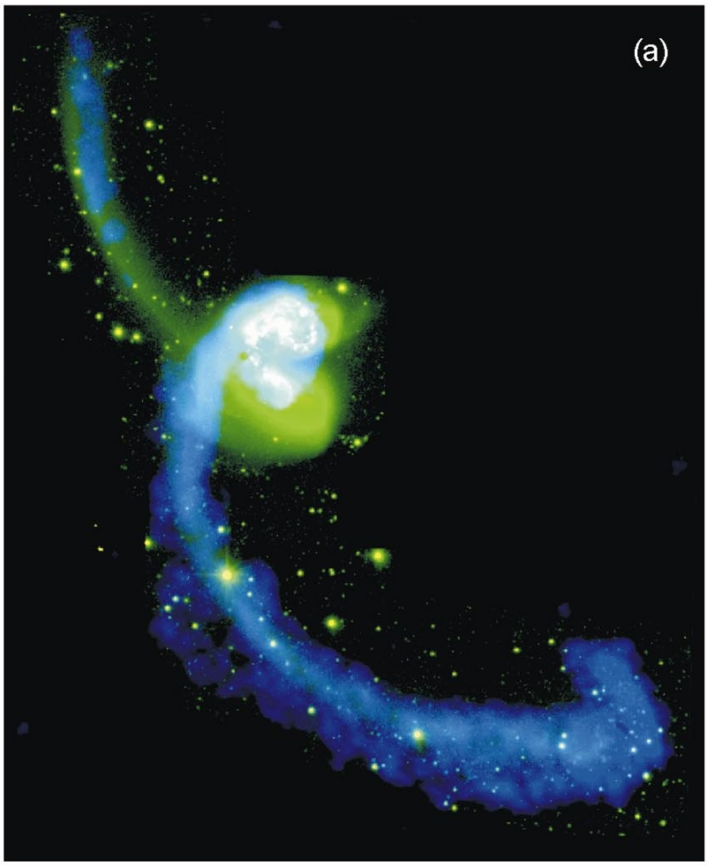

Figure 4.2: From Hibbard et al. (2001). Large scale HI gas (blue) and star (green/white) distribution of the Antennæ galaxies. Long gaseous tidal tails are extending from the disks of the progenitor galaxies.

The Antennæ , and in particular the central region, has been observed in all wavelengths from radio (e.g. Hummel and van der Hulst, 1986) to X-ray (e.g. Baldi et al., 2006) through IR (e.g. Bushouse et al., 1998; Wang et al., 2004; Brandl et al., 2005), optical (e.g. Hibbard et al., 2001) and UV (e.g. Hibbard et al., 2005). At large scales, long tidal tails extending from the galactic disks of the progenitor galaxies are visible in the star and HI gas distribution (see fig. 4.2). In the central region (see fig. 4.1), the two nuclei are separated by an *overlap* region filled with molecular clouds (pink) the luminosity of which is obscured by the absorption of dust (brown) in the ISM.

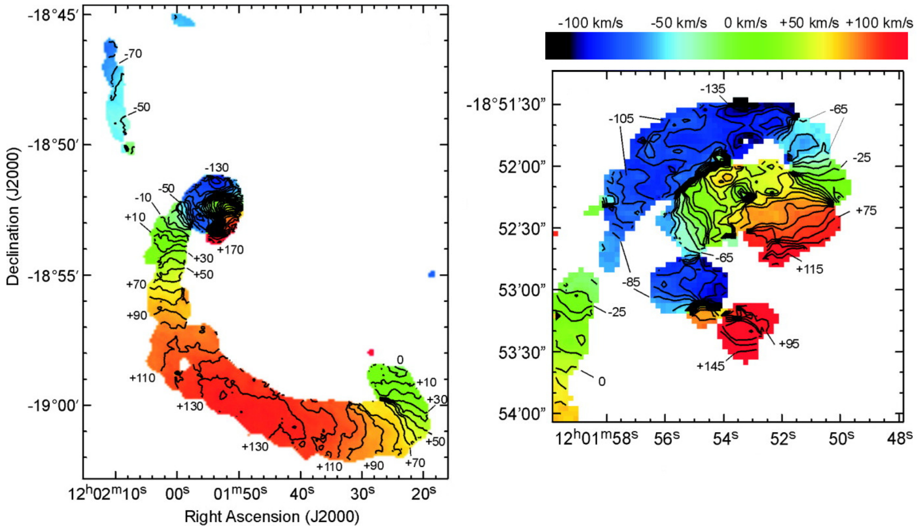

Figure 4.3: From Hibbard et al. (2001). Intensity-weighted HI velocity maps of the Antennæ galaxies (left) and the central region (right).

Observations also bring precious information on the kinematics of this ongoing merger, as shown in fig. 4.3. The velocity gradients observed in the central region make the galactic disks of the two progenitors NGC4038 ad NGC4039 easy to distingush. The velocity maps and numerical models agree on the fact that the long tidal tails are the result of a first pericentric passage that occcured a few ~ 100 Myr earlier, in contradiction with the assumed phase-1 classification made by (Toomre, 1977). A second pericentric passage that occured in the last ~ 10 Myr may be the cause of the intense star formation activity and complex structures in the ISM observed in the central region of the Antennæ galaxies. More than 10^3 bright young star clusters have been identified in this region and may have formed during a recent merger-induced star formation burst (Whitmore et al., 1999).

4.1.2 ... and numerical simulations

The first numerical simulation of the Antennæ galaxy merger was done by Toomre and Toomre (1972), where each galaxy was modeled as a point-mass. By looking at the gravitational influence of these point-mass on a set of pseudo-particles, they proved that bridges and tails observed in the Antennæ system were caused by the tidal interaction. But the pseudo-particles didn't contribute to the gravitational potential in their approach, thus particle interaction was prevented. Since the orbital decay of the galaxies via dynamical friction was not taken into account in their symmetrical model of the merger, it failed to reproduce the correct separation between the two galactic nuclei, as shown in fig. 4.4 (top).

Figure 4.4: First numerical simulations of the Antennæ system by Toomre and Toomre (1972) (top), Barnes (1988) (middle) and Mihos et al. (1993) (bottom). Restricted simulation by Toomre and Toomre (1972) well reproduced the tidal tails. Self-consistent simulation by Barnes (1988) took into account the orbital decay of the galaxies and better reproduced the central region. Mihos et al. (1993) presented the first hydrodynamical simulation with star formation enabled.

(Barnes, 1988) made the first self-consistent simulation of the Antennæ galaxies, highlighting the key role of the dark matter halo in the orbital decay of the galaxies. Their model better reproduced the close galactic nuclei in the central region. The first hydrodynamical simulation of the Antennæ system was done by Mihos et al. (1993). In addition to the collisionless particles (stars and dark matter), their model took into account a dissipative gaseous component able to form stars, although the required resolution to capture the small-scale physical processes such as molecular clouds collapse was not accessible yet (Barnes, 2004).

More recently, updated merger models have been introduced by Renaud et al. (2008) and Karl et al. (2008, 2010). These models are constrained to match both morphological and kinematical observations of the Antennæ , from large scale (tails) to small scale (central region), as shown in fig. 4.5. They better reproduced both the morphology and the kinematics of the long tidal tails and better match the observed *overlap* region (top right). The simulation presented in Renaud et al. (2008) (middle and bottom) only models the collisionless component of the galaxies where the intense star formation activity could be triggered in some regions undergoing compressive modes of the tidal field, in agreement with stellar cluster detection (Mengel et al., 2005, and see fig. 2.7). Karl et al. (2008, 2010) take into account the gaseous component of the Antennæ galaxies with hydrodynamical simulations, but used a *warm* thermodynamical model for the ISM, preventing the gas from fragmenting into clumps.

To capture the inhomogeneous star formation in a fragmenting ISM, I performed AMR hydrodynamical simulations of the Antennæ galaxy merger based on the collisionless model by Renaud et al. (2008). A “cold” thermodynamical model was used so I could investigate the impact of the modelization of the turbulent and cold phase of the ISM on the starbursting regime in merging galaxies. This work is presented in details in the next section.

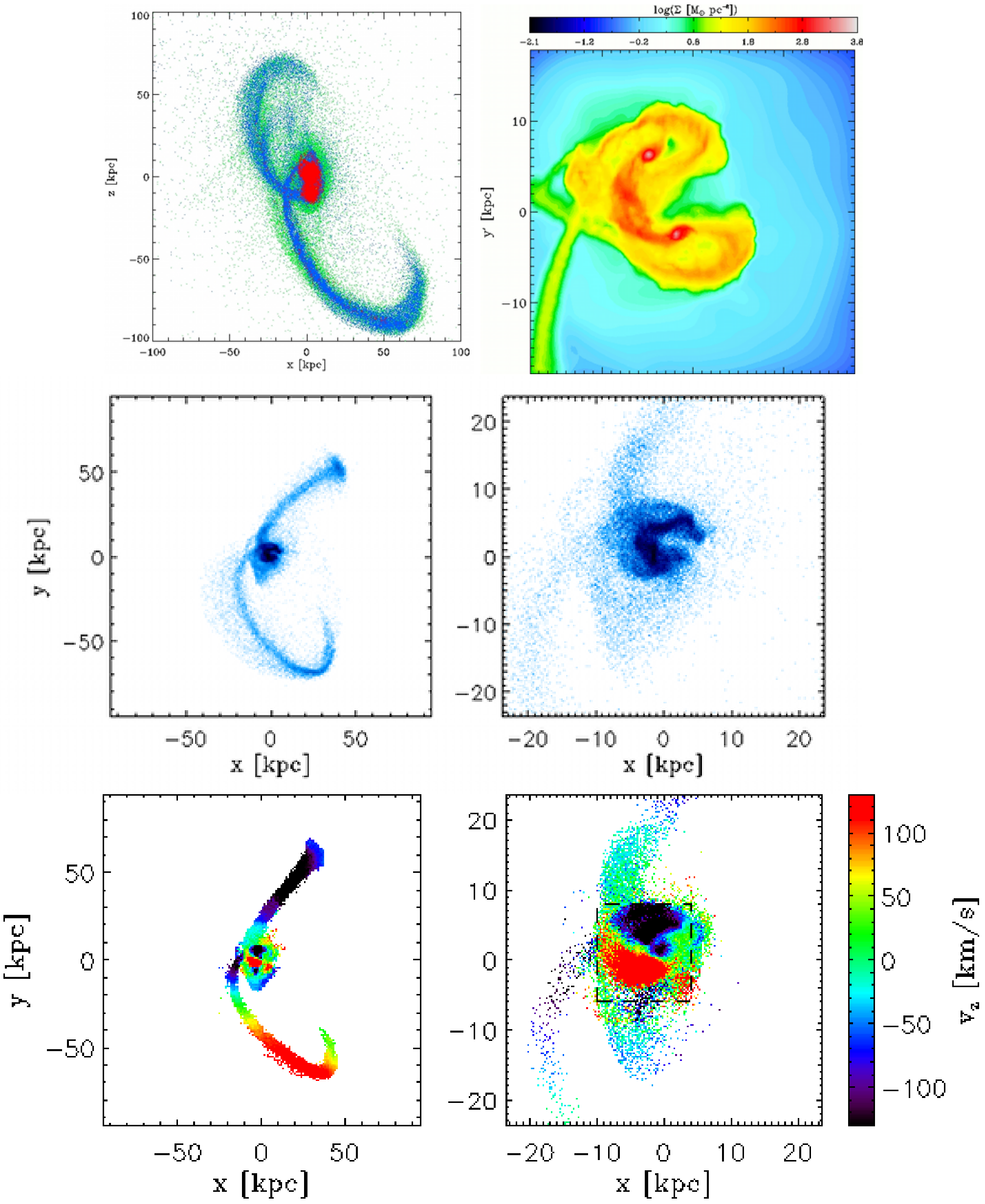

Figure 4.5: Recent numerical models of the Antennæ merger, constrained by both morphological and kinematical data. (top) stellar age from Karl et al. (2008) (left) and gas surface density from Karl et al. (2010) (right) showing the overlap region between the two galactic nuclei (red). (middle) Stellar surface density and line-of-sight velocity maps (bottom) from Renaud et al. (2008), showing fair agreement with the observational data (see fig. 4.2 and fig. 4.3).

4.2 This work: AMR hydrodynamical simulation of the Antennæ merger

I performed hydrodynamic AMR simulations of a galaxy major merger following the orbit of the Antennæ galaxies. The refinement strategy and the thermodynamical model I employed ensure that gas can cool down to a few 100 K so that gas fragmentation into dense clouds and star formation therein can thus be directly captured, at least down to masses of $\sim 10^6\ M_\odot$ and scales of $\Delta x_{\rm min} = 12$ pc. A realistic multiphase ISM with cold, dense and tubulent gas clouds embedded in a warm diffuse phase naturally arises. Using this model, I studied the interaction-induced star formation properties and compared to a lower-resolution simulation with a relatively homogeneous, warmer and more stable ISM. While merger-driven bursts of star formation are generally attributed to large-scale gas inflows toward the nuclear regions, I show that once a realistic ISM is resolved, the process of gas fragmentation into massive and dense clouds and rapid star formation therein dominates the merger-induced activity, while gas inflows become less efficient when a clumpy multiphase ISM is modeled.

Consequences include a potentially stronger starburst, but also a more extended and less homogeneous distribution of gas and star formation, while the gas density probability distribution function rapidly evolves toward very high densities. I thus propose that the actual mechanism of starburst triggering in galaxy collisions can only be captured at high spatial resolution and when the cooling of the gas is modeled down to less than 10^3 K. Not only does our model reproduce the properties of the Antennæ system, but it also explains the “starburst mode” recently revealed in high-redshift observations of active mergers compared to quiescent disks.

4.2.1 Model and parameters

Merger parameters and initial conditions

We model a pair of equal-mass galaxies in a box of size 200 kpc, with isolated and outflow boundary conditions. The collisionless particle model is the one described in Renaud et al. (2008). Each galaxy is embedded in a live halo with a Hernquist (1993) density profile. The pre-existing stars are described as two exponential disks. A central bulge with $B/D = 1$ is added, with a Hernquist (1990) profile. Although thinner, the gas distribution follows the stellar disk profile with a total gas fraction of 9% in each galaxy. We use the hyperbolic orbit proposed by Renaud et al. (2008) to reproduce the Antennæ system (see fig. 4.14). The merger model parameters are detailed in tab. 4.1. The AMR grid has a coarse level of $l_{\rm min} = 7$ corresponding to a coarse resolution of $\Delta x_{\rm max} = 1.5$ kpc. I considered two different runs:

- Low-resolution: $l_{\rm max} = 11$ ($\Delta x_{\rm max} = 100$ pc), mass resolution of $10^6\ M_\odot$.
- High-resolution: $l_{\rm max} = 14$ ($\Delta x_{\rm max} = 12$ pc), mass resolution of $4 \times 10^4\ M_\odot$.

Parameter	NGC 4038	NGC 4039
Numbers of particles		
N_{total}	7×10^5	7×10^5
N_{disk}	2×10^5	2×10^5
N_{bulge}	1×10^5	1×10^5
N_{halo}	4×10^5	4×10^5
Scalelengths (kpc)		
h_{disk}	0.88	0.88
$h_{\text{disk}_{\text{gas}}}$	0.44	0.44
r_{disk}	4.4	4.4
a_{bulge}	4.4	4.4
r_{halo}	30.8	30.8
Cut-off radii (kpc)		
z_{max}	8.8	8.8
$z_{\text{max}_{\text{gas}}}$	2.2	2.2
$r_{\text{max}_{\text{disk}}}$	22.0	13.2
$r_{\text{max}_{\text{bulge}}}$	4.4	4.4
$r_{\text{max}_{\text{halo}}}$	30.8	30.8
Masses ($10^9\ M_\odot$)		
m_{disk}	36.0	36.0
$m_{\text{disk}_{\text{gas}}}$	7.2	7.2
m_{bulge}	36.0	36.0
m_{halo}	180.0	180.0
Toomre parameters		
Q	1.5	1.5
Disk inclinations		
θ_x	60°	-60°
θ_y	0°	30°
Initial coordinates (kpc)		
(x, y)	$(26.4, 26.4)$	$(-26.4, -26.4)$
Initial velocities (km/s)		
(v_x, v_y)	$(-95.0, -47.5)$	$(95.0, 45.5)$

Table 4.1: Parameters of the Antennæ merger model adapted from Renaud (2010). A gaseous disk, thinner than the stellar disk is added ($f_{\text{gas}} = 9\%$). Note that both galaxies have the same mass, the only difference is that NGC4038 has a more radially extended disk than NGC4039.

Gas Physics and Star Formation Model

Gas equation-of-state The simulations have been performed with the AMR code `RAMSES` , using the EOS and merger modules developed in this work (see chapter 3). The *pseudo-cooling* mode of the equation-of-state was enabled, resulting in the temperature profiles shown in fig. 4.6. For the high resolution run, the gas can cool down to $T \simeq 600$ K whereas the temperature floor is $T \simeq 2500$ K at low resolution.

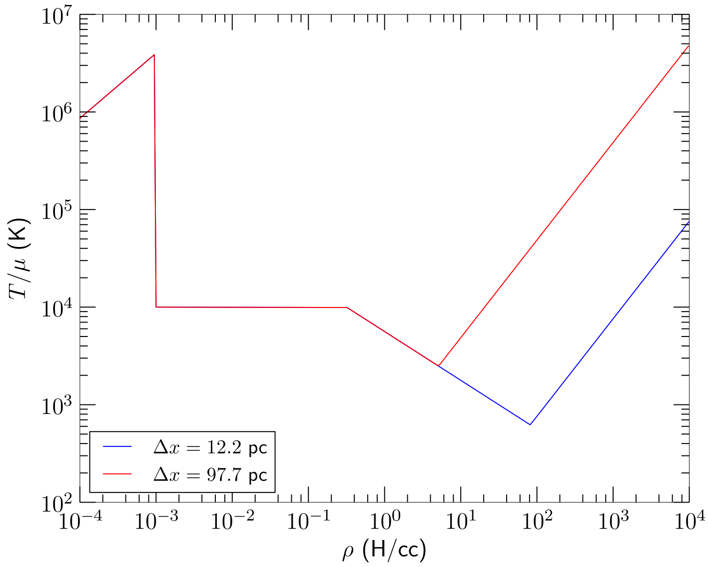

Figure 4.6: Pseudo-cooling equation-of-state for the low (red) and high (blue) resolution runs. When the maximum spatial resolution is $\Delta x \simeq 100$ pc, the temperature decreases at high density down to $T(n_{\text{Jeans}} = 5\ \text{H/cc}) \simeq 2500$ K. For the high resolution run ($\Delta x \simeq 12$ pc), the temperature reaches $T(n_{\text{Jeans}} = 90\ \text{H/cc}) \simeq 600$ K where the Jeans pressure floor dominates, preventing the gas from artificially fragmenting.

Note that in this pseudo-cooling approach, self-shielding of the radiation is neglected: gas cooling at very high density may have been underestimated, but I also neglected the effect of local radiation sources such as OB stars as additional heating sources. Although this thermal model appears rather uncertain, it provides a reasonable route of gas dissipation, maintaining the gas temperature to a realistic average value at a given density.

Gas probability density function (PDF) and star formation As shown by several authors (Elmegreen, 2002; Elmegreen and Scalo, 2004; Wada and Norman, 2007), the multiphase structure of the ISM is built up from complicated processes involving radiative losses (ultraviolet and infrared line cooling, molecular and dust cooling) as well as various heating mechanisms (cosmic rays and UV heating, supernovae and stellar feedback) and of course self-gravity. Surprisingly, numerical experiments have shown universal properties for the gas density PDF in isolated galaxies, with log-normal or power-law distribution shapes (Wada and Norman, 2007; Tasker and Tan, 2009; Agertz et al., 2009a). The gas density PDF $f(\rho)$ in the galactic disk can be described by a single log-normal function:

$$f(\rho)\mathrm{d}\rho = \frac{1}{\sqrt{2\pi}\sigma}\exp\left[-\frac{\ln(\rho/\rho_0)^2}{2\sigma^2}\right]\mathrm{d}\ln\rho \tag{4.1}$$

where ρ_0 is the characteristic density and σ is the dispersion. This was explained as a fundamental property of isothermal (or dissipative) self-gravitating turbulence. This EOS-based model produced a log-normal gas density PDF in isolated galaxies similar to the results of complete cooling/heating calculations and a realistic density power spectrum of ISM substructures (Bournaud et al., 2010).

In this work, the impact of a galaxy collision on the turbulence, the evolution of the gas density PDF and the resulting star formation rate (SFR) is studied. Star formation occurs only in dense enough regions (molecular clouds). In the simulation, it is controlled by a set of two parameters: the star formation efficiency ϵ_* and the gas density threshold n_* above which gas mass can be converted into star particles.

Parameter	Low-res.	High-res.
ϵ_*	1%	1%
n_*	10^{-1} H/cc	8.0 H/cc

Table 4.2: Star formation parameters used in the low and high resolution simulations of the Antennæ merger.

These two main parameters are usually calibrated using observations of nearby galaxies and the so-called Kennicutt–Schmidt (KS) law. The real efficiency is $\sim 40-50\%$ in regions where the gas density reaches $n_\mathrm{H} \sim 10^4 - 10^5$ H/cc. But models with a limited resolution cannot reach this density range and have to use a low threshold combined with a low efficiency (Wada and Norman, 2007), which globally reproduces the same KS law (Elmegreen, 2002). The global SFR in our model (like most others) can be computed directly by integrating the Schmidt law over the gas density probability distribution function (PDF) above the threshold n_* . The problem therefore boils down to predicting the PDF evolution during the merger process. The star formation parameters have been calibrated so that the initial SFR is $\sim 1\ M_\odot.\mathrm{Myr}^{-1}$ per galaxy in isolated disks, in agreement with the KS law of local spirals. They are summarized in tab. 4.2. Since n_* is significantly below the pressure floor density n_Jeans in both low and high resolution runs, the star forming part of the PDF is well sampled.

4.2.2 Merger driven gas fragmentation into massive GMCs

At the beginning of the simulation, both galaxies behave like isolated disks and settle at hydrostatic equilibrium. At $t \simeq 230$ Myr, the first pericentric passage triggers strong perturbations in boths disks. The low-resolution model, with an artificially warm, smooth and stable ISM, follows the traditional gas response to disk interaction, where tidal torques excite a strong $m = 2$ mode, drives tidal tail formation outside the corotation radius and gas inflows inside the corotation radius. The gas response is dominated by the gradual inflow of gas toward the nuclear region with a timescale of a few 10^2 Myr.

In the high resolution run, the $m = 2$ mode is also excited but the gas can cool down to a few ~ 100 K, the fragmentation process is resolved and dense gas clumps form in a few 10 Myr. In this case, the gas response to the interaction is therefore dominated by fragmentation in many dense clouds scattered in the disks, along the spiral arms or in a "beads on a string" mode along the gaseous bridge linking the two galaxies (see fig. 4.9).

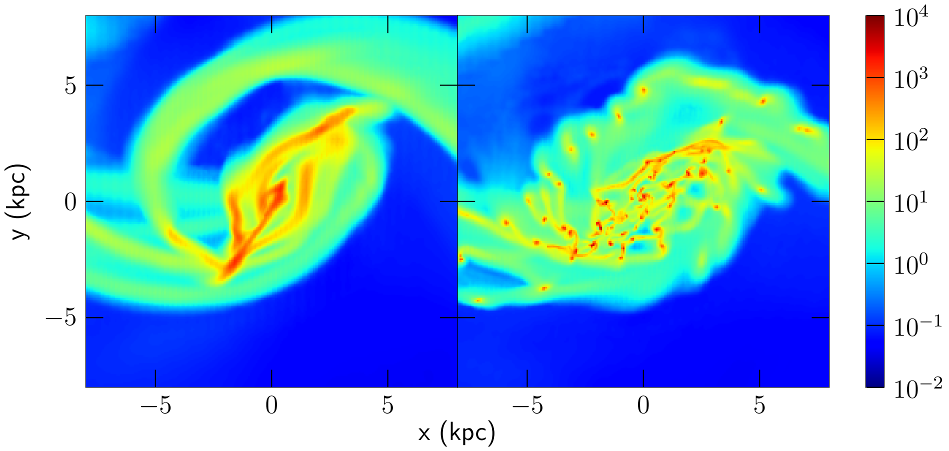

Figure 4.7: Face-on views of NGC4038 gaseous disk at $t = 350$ Myr, nearly 120 Myr after the first pericenter. At low resolution, the interaction excites a $m = 2$ mode, resulting in a strong gas inflow and smooth spiral arms (left). At high resolution, the gas fragments into dense and cold clumps, making the gas inflow less efficient.

Using the theory of gravitational instability in a cylinder (Chandrasekhar and Fermi, 1953; Ostriker, 1964; Elmegreen, 1979), we can compute the spiral arm stability criterion $q = \sigma^2/(2G\mu)$, where μ is the linear mass density along the arm. The higher temperature at high resolution result in thinner spiral arms (higher surface density) but the linear density is quite similar in both simulations ($\mu \simeq 4000\ M_\odot$.pc^{-1} on average). At low resolution, the minimum sound speed always lies above 5 km.s^{-1} , so that $q > 1$ everywhere and the arm remains stable. At high resolution, the minimum sound speed can be lower (around

2.5 km.s^{-1}) so that q can be as low as 0.25 in quiescent regions, and the spiral arm can fragment into clumps in a free-fall time ($\sim$ 1 Myr). These clumps have typical masses in the range $M_{\text{clump}} \sim 10^6 - 10^8\ M_\odot$. The gas velocity dispersion in our isolated disk at high resolution is typically $10 - 15$ km.s^{-1} but it increases by a factor of $2 - 3$ in most regions, and locally by a factor of 5 or more, during the interaction. The Jeans length increases in similar proportions, so the typical mass of gas clouds formed by gravitational instabilities at fixed average density is increased by factors of typically $10 - 100$. Such increased gas turbulence is observed in interacting galaxies (e.g. Elmegreen et al., 1995) and the associated formation of supermassive gas clouds studied by Elmegreen et al. (1993). The low-resolution model produces an artificially stable ISM and does not resolve this process.

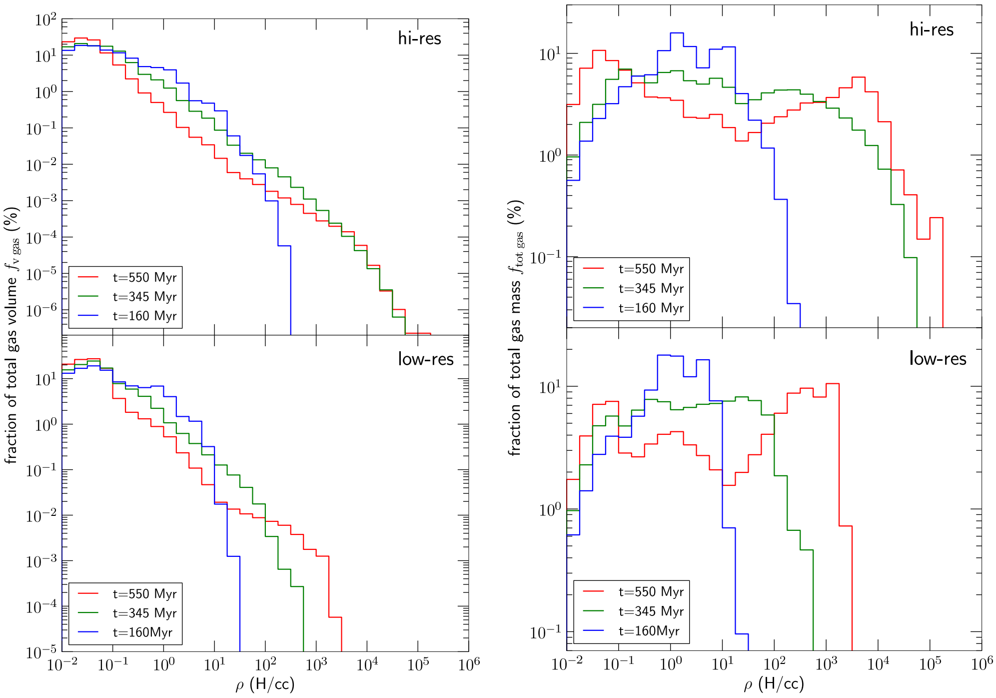

Figure 4.8: Evolution of the gas mass (right) and volume (left) density PDF before ($t =$ 160 Myr, blue) and during the merger ($t = 345, 550$ Myr, green and red) for the high (top) and low (bottom) resolution simulations. The galaxy interaction drives an enrichment of the PDFs toward higher densities. The higher the resolution, the larger density range can be resolved.

The associated density PDF increases slowly and continuously toward higher and higher densities (see fig. 4.8) as a result of the galaxy interaction. This evolution is achieved rapidly after first pericenter passage and with little changes in the later stages. Note that no feedback process has been taken into account into this merger model. This process is expected to have a great impact on the gas PDF since is is an efficient way to reinject energy from small scales (high densities) to large scales (low densities). It could efficiently self-regulate the gas dissipation into small dense clumps (see e.g. Bournaud et al., 2010), and consequently star formation. The evolution of the PDF directly impacts the star formation in the Antennæ galaxies, as detailed in the next section.

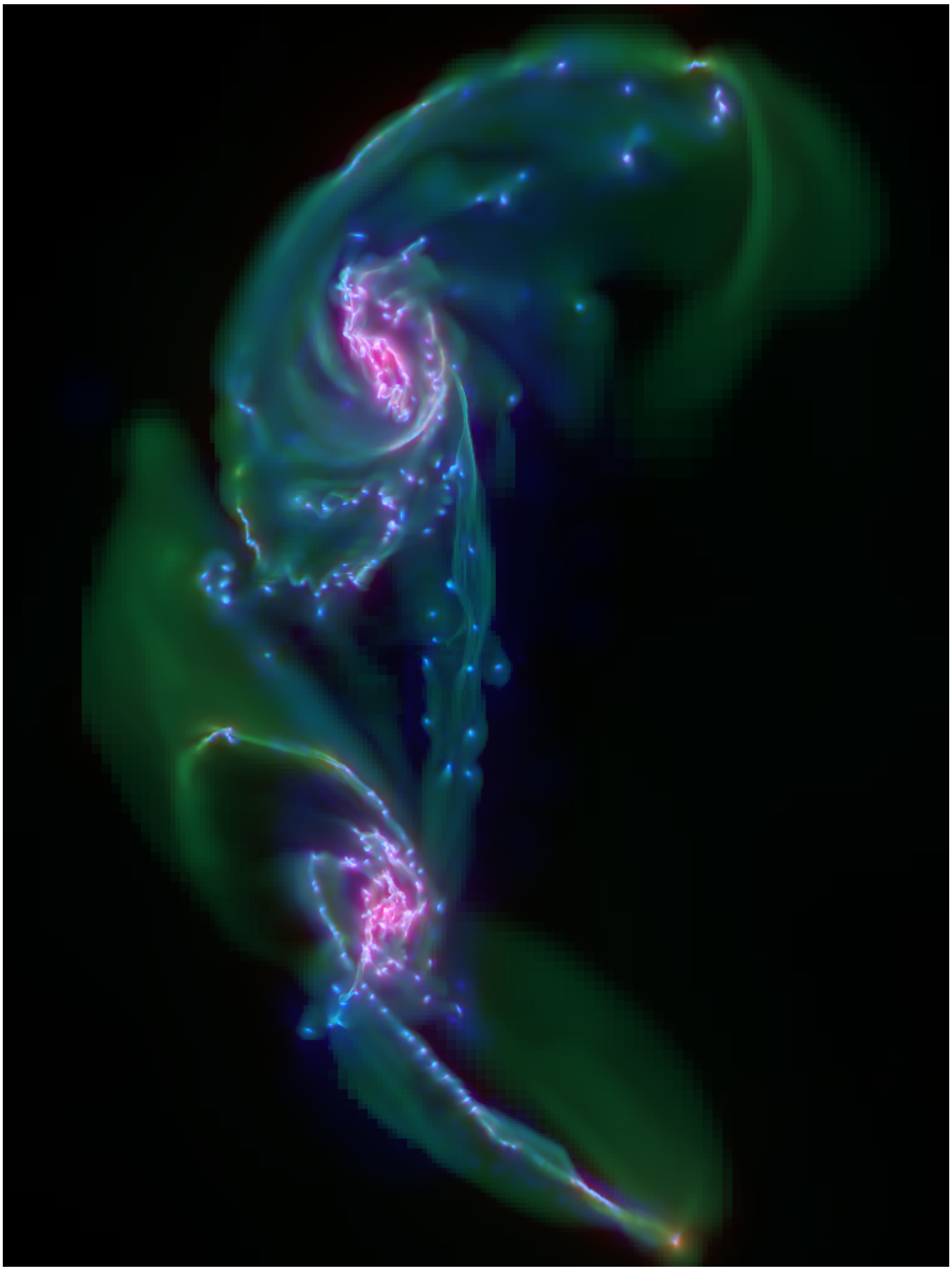

Figure 4.9: Antennæ merger simulation snapshot at $t \simeq 350$ Myr (~ 120 Myr after the first pericenter). The gas density is shown in green, the old stellar particle distribution in red and the newborn star particle distribution in blue. The gravitational perturbation due to the first pericentric passage made the gas fragment into ~ 200 massive giant molecular clouds(GMCs) within the disks, along the tidal tails and in a *beads-on-string* mode along the gaseous bridge linking the two galaxies. Each cloud host a super stellar cluster (SSCs) due to its intense star formation.

4.2.3 Star formation burst and formation of SSCs

Although the pre-merger isolated disks have been calibrated to produce stars at a similar rate ($\sim 1\ M_{\odot}.\mathrm{yr}^{-1}$), the global star formation efficiency during the mergers is totally different depending on the resolution, i.e., depending on whether we model a smooth and warm ISM or a cloudy multiphase ISM at high resolution.

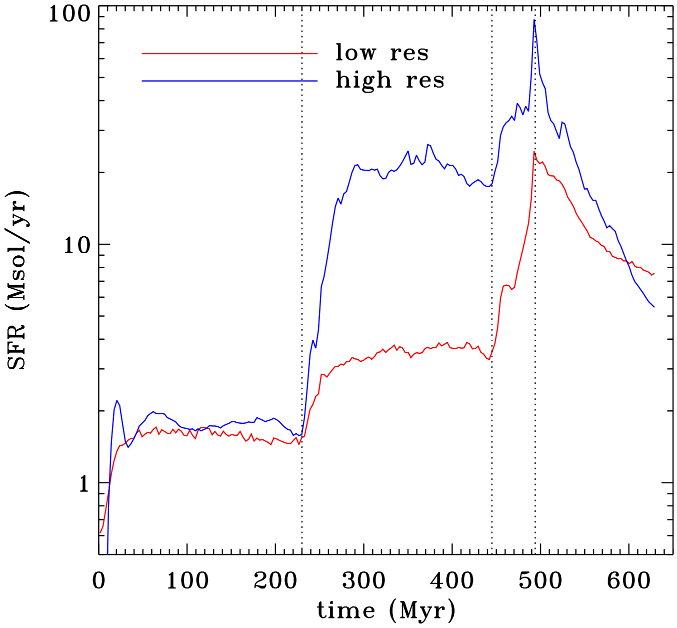

Figure 4.10: Star formation history in the Antennæ merger simulations for the low (red) and high (blue) resolution runs. Times for the first pericenter, second pericenter, and final merger are indicated by vertical dotted lines.

At first pericentric passage ($t \simeq 250$ Myr), the star formation rate rapidly rises in both runs but with a dramatic difference in amplitude. Around $t \simeq 450$ Myr (second pericenter) and $t \simeq 500$ Myr (final coalescence), the star formation rate increases again, now more significantly for the low-resolution run, and it steadily declines after the merger. Star formation rates are discrepant by a factor of ~ 10 after the first pericenter and ~ 5 in the final merger stages.

This is due to completely different ISM dynamics building up two different density PDFs between the low- and the high-resolution runs (see fig. 4.8) and different spatial distribution of the gas. In the low-resolution model, the gas response is dominated by a strong inflow. The growing central concentration of gas lead to an an enhanced star formation that takes place in the central kiloparsec (see fig. 4.11).

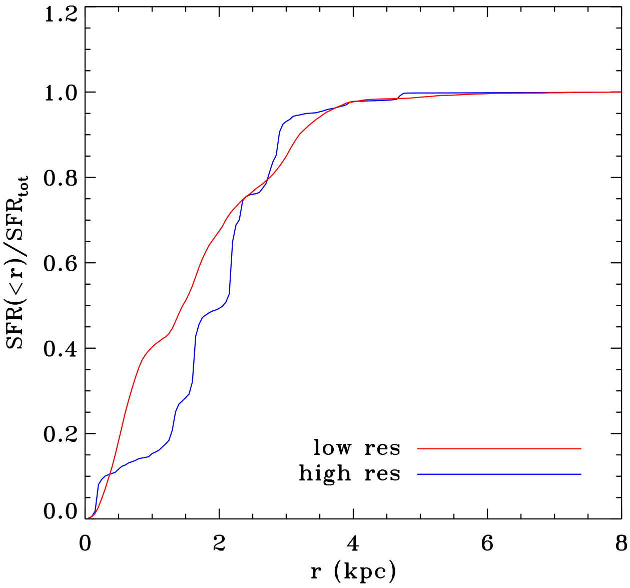

Figure 4.11: Fractional star formation rate radial profiles of the NGC4038 galactic disk presented in fig. 4.7. The two lines corresponds to the low (red) and high (blue) resolution runs. The low-resolution run has a homogeneous nuclear star formation while the star formation is more clustered and widespread at high resolution.

The gas evolution largely differs in the high-resolution run with a cloudy multiphase ISM. An m = 2 mode excited by tidal torquing is still visible in the right panel of fig. 4.7. However, since the collapse timescale of the gas clouds is much smaller than the inflow timescale ($t_{\mathrm{ff}} \sim 1$ Myr $\ll 100$ Myr $\sim t_{\mathrm{dyn}}$), the dominant process in the ISM is the gas fragmentation and the clumpy structure has a less collisional behavior than a smooth spiral arm . As a consequence, the angular momentum transfer responsible for the strong gas inflow is much less efficient than in the low resolution run, the clumpy gas builds a much more modest central density peak than the low-resolution model and star formation is more widespread over the central 3 kpc.

The star formation rate also follows this evolution driven by ISM fragmentation in massive and dense clouds (see fig. 4.13 and proceeds in super stellar clusters (SSCs). Between the first and second pericenter ($t \simeq 345$ Myr and see fig. 4.1), the stellar cluster population peaks at ~ 200 SSCs, with masses in the range $2 \times 10^5 - 10^8$ $M_\odot$. Figure 4.12 shows a good agreement between the SSCs mass spectrum of our Antennæ model and the one by Bournaud et al. (2008). Since SN feedback was not taken into account in this simulation, the only process able to destroy the stellar clusters remains tidal disruption, which occured during the second pericenter and final merger of the galaxies.

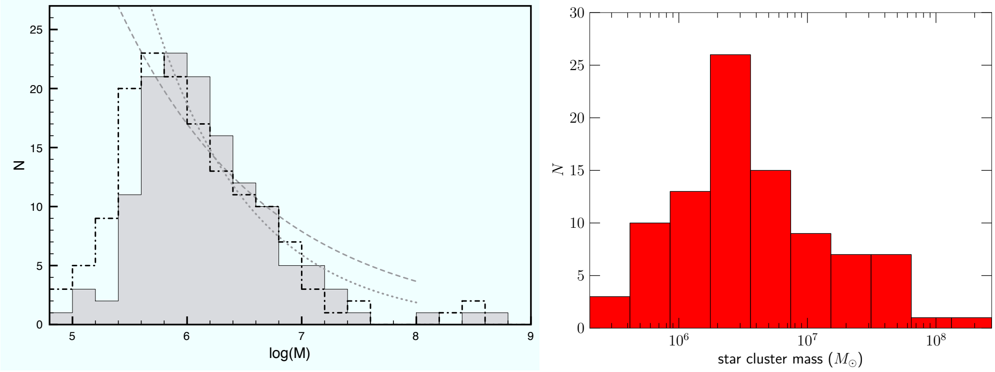

Figure 4.12: Super stellar cluster mass spectrum from Bournaud et al. (2008) (left) and this work (right) at $t \simeq 345\,\mathrm{Myr}$, when the total number of SSCs peaks (see fig. 4.9).

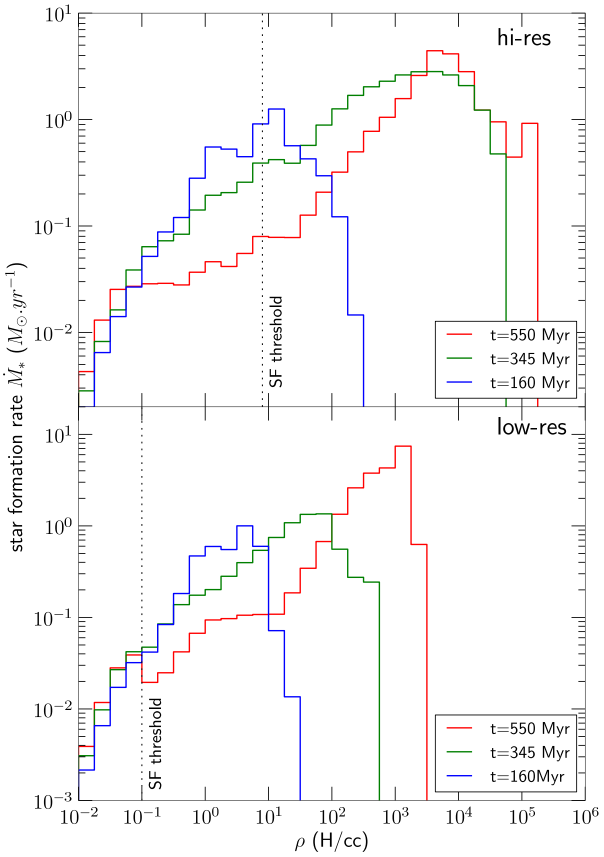

Figure 4.13: Star formation-weighted gas density PDF at three different epochs, before ($t = 160\,\mathrm{Myr}$) and during the merger ($t = 345, 550\,\mathrm{Myr}$), for the high (top panel) and low (bottom panel) resolution simulations. In each case, the star formation density threshold is indicated by the dotted vertical line.

4.2.4 Implications

Antennæ and other mergers

Although merger-induced star formation in our model is not primarily driven by an inflow of gas and less concentrated than in earlier models, it remains relatively concentrated near the center of the merging systems (see fig. 4.11): there is still a tidally induced inflow, and the central regions are denser and more prone to star-forming instabilities.

This is consistent with SF in ultra-luminous infrared galaxies (ULIRGs) being in general centrally concentrated (assuming ULIRGs are mergers). Nevertheless, our model also explains that the interaction-induced star formation can also be, for a part, radially extended. This can explain why a number of interacting galaxies actually show extended star formation with SSCs forming at several kpc from their center, such as Arp 140 (Cullen et al., 2006) and the Antennæ (Wang et al., 2004).

As for the Antennæ , the orbit of which is matched by our simulation, there is a general consensus that we are witnessing the merger close to the second pericenter passage, when the two disks are still well separated (Renaud et al., 2008). This corresponds to an epoch close to 475 Myr in our simulation (see fig. 4.14). Our low-resolution models reaches star formation rates around 10 Myr^{-1} just after the second pericenter passage and during only 50 Myr: these properties are in broad agreement with recent SPH simulations by Karl et al. (2010) and with the observed SFR (Zhang et al., 2001). Karl et al. (2010) then proposed that this high star formation rate and the extended star formation in the Antennæ result from the system being observed just at the particular instant of overlap between the two disks. Our high-resolution model, however, shows that high star formation rates around 20 Myr^{-1} and relatively extended star formation can be produced during a longer period (300 Myr) and does not require the system to be observed at a particular and brief instant.

Assuming a magnitude-age relation for stellar clusters, we can compute a mock observational map of the stellar distribution from our simulation at the time corresponding to the observed Antennæ system. Figure 4.14 is an age-colored stellar luminosity map based on the double power law fit of the M_v-age relation obtained from cluster simulations (Weidner et al., 2004):

$$L \propto \begin{cases} L_0 & (\mathrm{age} \leq 10\ \mathrm{Myr}) \\ L_0 \left(\frac{\mathrm{age}}{10\ \mathrm{Myr}}\right)^{-0.7} & (\mathrm{age} > 10\ \mathrm{Myr}) \end{cases} \tag{4.2}$$

The clustered distribution of young stars in the central region is more representative of the star formation process as seen in HST images of the Antennæ system than the smooth distribution shown in Karl et al. (2010) (fig. 4.5, top right).

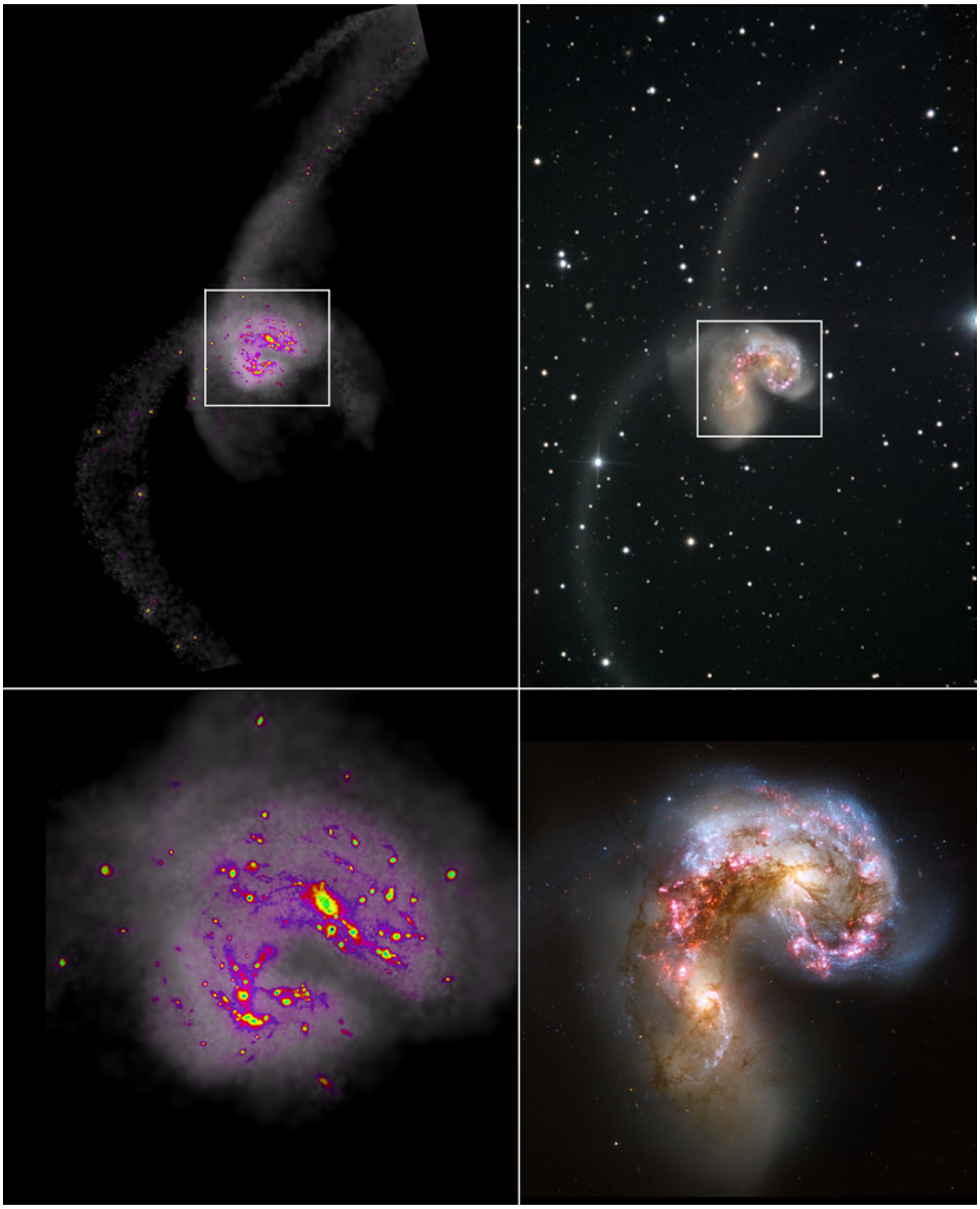

Figure 4.14: (left) Age-colored stellar luminosity maps shown at the best-fit time from the simulation ($t \simeq 475\,\mathrm{Myr}$) between the second and third pericentric passage. The massive but old stellar population appears faintly white. The young luminous stellar clusters appear purple/red/yellow/green. (right) Hubble Space Telsecope image.

General Star-formation Laws and the Starburst Regime

Observations suggest a dual law for star formation, where the integrated gas consumption timescale ($\Sigma_{SFR}/\Sigma_{gas}$) is relatively low for quiescent star-forming disks and higher for starbursting ULIRGs and sub-millimeter galaxies (likely major mergers), as pointed out independently by Daddi et al. (2010a) and Genzel et al. (2010). To compare our models with these observations, we retrieved integrated properties such as half-light radii, the total gas mass and the total star formation rate at several instants during the simulations, for both low- and high-resolution models. The low-resolution model, where the starburst is driven only by the central gas inflow, does not show the observed change in $\Sigma_{\mathrm{SFR}}/\Sigma_{\mathrm{gas}}$: the star formation rate increases during the merger, but only in proportion corresponding to the increase in the global gas density Σ_{gas} , and this model remains close to the standard relation for isolated disks.

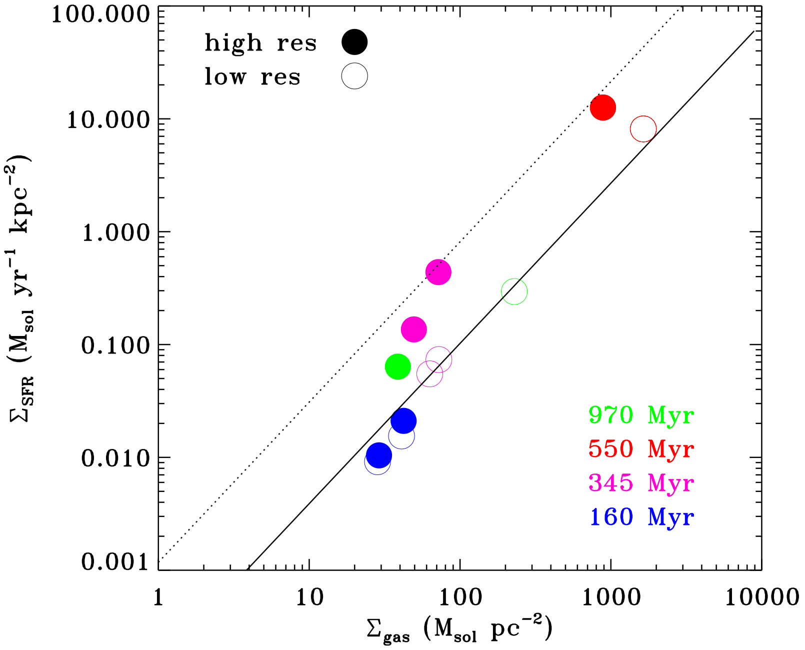

Figure 4.15: Time evolution of the two merging galaxies in the Kennicutt-Schmidt diagram, comparing the low- and high-resolution runs. The solid line is a fit to the average Kennicutt-Schmidt law for quiescent galaxies, while the dotted line is the law for starburst galaxies (see eq. 2.3, eq. 2.4 and Daddi et al. 2010a).

The high-resolution model has its starburst driven mostly by increased gas turbulence and fragmentation. The gas density increases mostly on small scales in dense clumps throughout the system: this process does not affect the total effective size of the gas component, so the observable global density Σ_{gas} has only a modest increase. At the same time, the starburst is even stronger than in the low-resolution model. This process brings our model in agreement with the "starburst versus quiescent KS law" pointed out by observations, throughout the duration of the merging process.

Clustered star formation in high-resolution merger models can also affect the final structure of the resulting early-type galaxies (Bois et al., 2010). We thus propose that these recent observations unveiled a "starburst regime" where the efficiency of star formation on small scales and at high densities is unchanged, but exacerbated gas turbulence and fragmentation into massive clouds result in faster gas consumption and higher integrated star formation efficiency. The adopted star formation law inside the clouds is not the key ingredient in the interpretation, the main effect being the rapid evolution of the density PDF. Different star formation models can indeed lead to different quantitative predictions, but the main qualitative change comes from resolving the high-density tail of the PDF (Governato et al., 2010). Previous models of galaxy mergers did not resolve ISM turbulence and clouds, and could not unveil the physical processes driving this starburst mode. The actual process of star formation in starbursting mergers cannot be captured with sub-grid models on scales larger than 100 pc and requires clustered star formation in a multiphase ISM to be directly resolved.


(46 BILLION LIGHT-YEARS UP)
HUBBLE DEEP FIELD OBJECTS
— ONE BILLION LIGHT-YEARS —
GREAT ATTRACTOR
ANTENNAE GALAXIES (COLLIDING)
ANDROMEDA
HOLY CRAP LOTS OF SPACE
— ONE MILLION LIGHT YEARS —
MAGELLANIC CLOUDS
EDGE OF GALAXY
GALACTIC CENTER
CRAB NEBULA
ORION NEBULA
HORSEHEAD NEBULA
RIGEL
BETELGEUSE
FORD PREFECT
ROMULAN NEUTRAL ZONE
THE PLEIADES DUH.
EXPANDING SHELL OF RADIO TRANSMISSIONS
EDGE OF FEDERATION SECTOR 0-0-1
POLLUX
ARCTURUS
MISSING WMD's
SIRIUS
ALPHA CENTAURI
BARNARD'S STAR
— ONE PARSEC —
— ONE LIGHT-YEAR —
OORT CLOUD (?)
BUPKIS

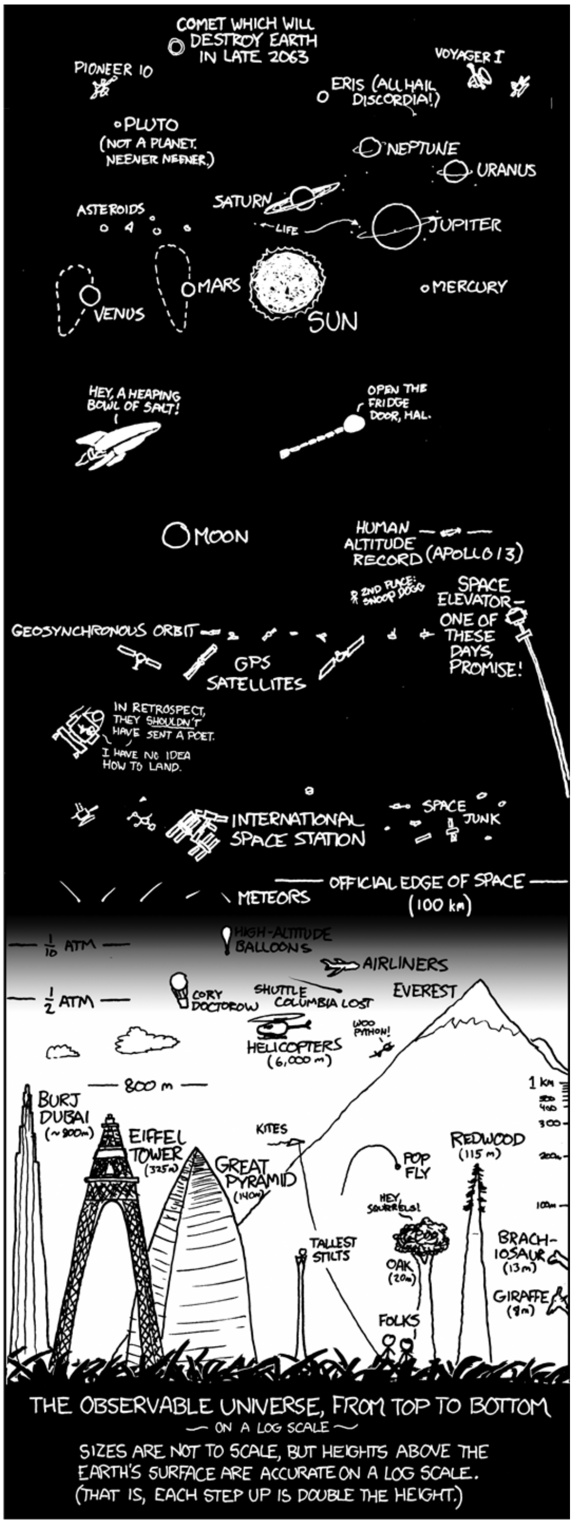
COMET WHICH WILL DESTROY EARTH IN LATE 2063
PIONEER 10
VOYAGER I
ERIS (ALL HAIL DISCORDIA!)
PLUTO (NOT A PLANET. NEENER NEENER.)
NEPTUNE
URANUS
SATURN
ASTEROIDS
LIFE
JUPITER
MARS
VENUS
SUN
MERCURY
HEY, A HEAPING BOWL OF SALT!
OPEN THE FRIDGE DOOR, HAL.
MOON
HUMAN ALTITUDE RECORD (APOLLO 13)
2ND PLACE: SNOOP DOGG
SPACE ELEVATOR — ONE OF THESE DAYS, PROMISE!
GEOSYNCHRONOUS ORBIT
GPS SATELLITES
IN RETROSPECT, THEY SHOULDN'T HAVE SENT A POET.
I HAVE NO IDEA HOW TO LAND.
INTERNATIONAL SPACE STATION
SPACE JUNK
METEORS
OFFICIAL EDGE OF SPACE (100 km)
1/10 ATM
HIGH-ALTITUDE BALLOONS
AIRLINERS
1/2 ATM
CORY DOCTOROW
SHUTTLE COLUMBIA LOST
EVEREST
WOO PYTHON!
HELICOPTERS (6,000 m)
800 m
1 km
500
400
300
200
100 m
BURJ DUBAI (~800m)
EIFFEL TOWER (325m)
GREAT PYRAMID (140m)
KITES
POP FLY
REDWOOD (115 m)
HEY, SQUIRRELS!
TALLEST STILTS
OAK (20m)
BRACHIOSAUR (13m)
GIRAFFE (5m)
FOLKS
THE OBSERVABLE UNIVERSE, FROM TOP TO BOTTOM
— ON A LOG SCALE —
SIZES ARE NOT TO SCALE, BUT HEIGHTS ABOVE THE EARTH'S SURFACE ARE ACCURATE ON A LOG SCALE. (THAT IS, EACH STEP UP IS DOUBLE THE HEIGHT.)

CHAPTER 5

SMBHs pairing during galaxy mergers

The configuration of the nuclear region of a remnant galaxy in which two SMBHs could form a binary system with sub-parsec scale separation within the few 10^6 years after a merger is not really known yet. A few simulations tried to reach such a stage starting from a realistic galaxy merger model, but none of them were successful to capture properly all the key processes involved in the formation of a black hole binary within a gas-rich nuclear disk: dynamical friction onto the gas, turbulence, AGN feedback, shocks. The orbital decay of massive black holes in such a regime involving many scales is not yet explored by eulerian three-dimensional hydrodynamical simulations.

In this chapter, I present the first AMR simulations of a galaxy merger hosting the formation and hardening of a SMBH binary system embedded in a hot nuclear disk. The simulation follows the orbital decay of the two SMBHs down to tenths of parsec scale separation. First, I will briefly introduce the LISA space mission and then the numerical results presented in Chapon et al. (2011) will be detailed in this chapter.

5.1 Who is LISA ?

Laser Interferometer Space Antenna (LISA), is (was ?) a joint NASA-ESA mission designed to observe astrophysical and cosmological sources of gravitational waves. Predicted by Einstein's theory of relativity, graviational waves are propagating perturbations in the curvature of spacetime generated by heavy, rapidly accelerating matter and energy.

LISA consists of three identical spacecrafts linked together by laser beams and flying on a Earth-trailing orbit in a triangular constellation, with equal arms of 5×10^6 km each. As gravitational waves from distant sources reach LISA, they warp space-time, stretching and compressing the triangle. In a low frequency

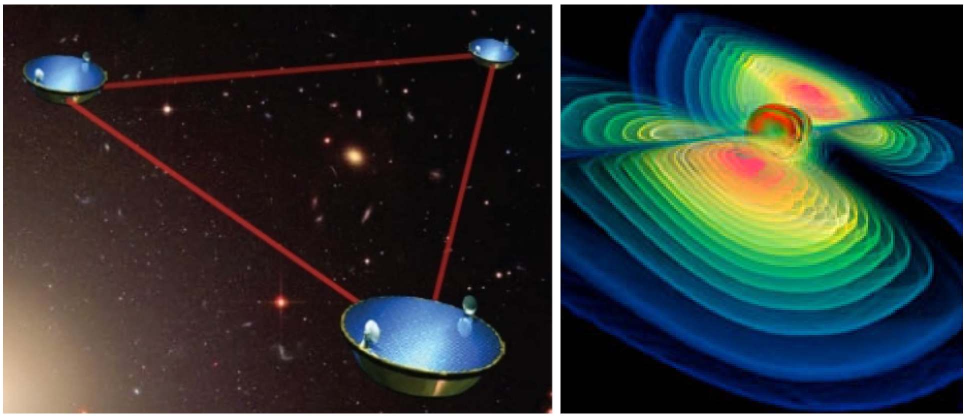

Figure 5.1: (left) The 3 identical spacecrafts of the Laser Interferometer Space Antenna (LISA) mission. (right) Simulation of gravitational wave emission from coalescing massive black holes. (Credit: NASA-ESA)

band (0.03 mHz $\leq f \leq$ 0.1 Hz), its interferometer could detect a variation of the arm length of $\sim$ 20 pm, allowing LISA to measure the shape and timing of the waves emitted by various sources such as cosmological gravitational wave background/burst, galactic binaries, extreme mass ratio inspiral (EMRI) and coalescing massive black holes in the center of merging galaxies (see e.g. Jaffe and Backer, 2003; Vecchio, 2004; Sesana et al., 2005).

LISA could detect massive black hole binaries only during the final stage of the binaries when its separation reach subpc ($\sim$ 0.01 pc) scales. But an important question remains: how can they reach the gravitational wave emission regime ? To reach such a separation, binary formation and hardening must occur at larger scale beforehand. Various processes are involved: dynamical friction against the stellar and gaseous background, 3-body interactions and tidal torquing. The dynamical range that a black hole binary needs to cover to become a LISA-detectable source is several orders of magnitude. These binary formation events are likely to be associated with large scale galaxy mergers and are likely to occur in gas-dominated backgrounds.

So far, no numerical study has been done with a hydrodynamical grid code to study these processes at subparsec scale resolution. The first high resolution AMR hydrodynamical simulation focused on the SMBH pairing process in the context of a galaxy merger is detailed in the following section.

5.2 SMBHs pairing in an AMR hydrodynamical simulation of a galaxy merger

5.2.1 Numerical setup

I used the `RAMSES` code introduced in chapter 3 to follow both the galaxy merger at large scale and the binary SMBHs merger at small separation. Its shock capturing abilities and low intrinsic numerical viscosity (the HLLC Riemann solver and the MinMod slope limiter were adopted) make it ideal to address the problem at hand.

I model the evolution of a galactic major merger with a coplanar orbit in which each galaxy hosts a SMBH at its center. The galactic model, inspired by the one from Mayer and Kazantzidis (2008), consists in a NFW isotropic dark matter halo, a rotating exponential stellar disc, a Hernquist bulge, a thin rotating exponential gas disc and a single motionless and non-accreting SMBH particle placed at the center of the galaxy.

Parameter	
Dark matter halo (NFW)	
$N_{\rm DM}$	7×10^6
v_{200}	138 km.s^{-1}
M_{200}	$8.7 \times 10^{11}\ M_\odot$
conc. parameter c	9
spin factor λ	0.05
Stellar disk	
$N_{\rm disk}$	1.8×10^6
$M_{\rm disk}$	$0.05\ M_{200} = 4.35 \times 10^{10}\ M_\odot$
$R_{\rm disk}$	3.6 kpc
$h_{\rm disk}$	$0.1\ R_{\rm disk}$
Stellar bulge	
$N_{\rm bulge}$	8×10^5
$M_{\rm bulge}$	$0.02\ M_{200} = 1.74 \times 10^{10}\ M_\odot$
$a_{\rm bulge}$	$0.1\ R_{\rm disk}$
Gas disk	
$M_{\rm gas}$	$4.18 \times 10^9\ M_\odot$
$R_{\rm gas}$	$R_{\rm disk}$
$h_{\rm gas}$	$h_{\rm disk}$
Black hole	
$M_{\rm BH}$	$2.5 \times 10^6\ M_\odot \simeq 1.4 \times 10^{-4}\ M_{\rm bulge}$

Table 5.1: Parameters of the galaxy model for the equal-mass merger adapted from Mayer and Kazantzidis (2008).

As in Kazantzidis et al. (2005), the mass of the SMBH particle is chosen consistently with the $M_{bh} - \sigma$ relation (Ferrarese and Merritt, 2000; Tremaine et al., 2002). The gaseous disk is initialized on the AMR grid as a continuous density field with an exponential profile.

For the merger model, we use the same parabolic coplanar orbit presented in Mayer and Kazantzidis (2008). During the interaction, both SMBH particles keep at the center the galactic cores in which they were embedded. After a few (galactic) pericentric passages, dynamical friction finally makes the two glaxies merge at $t \simeq 5.244$ Gyr. The first 4 Gyr of the simulation have been run at low resolution to let us focus on the final merger of the galactic cores at much higher resolution. To avoid binary relaxation among DM/stellar particles, the gravitational softening of every particle except for the two SMBH particles cannot be smaller than $\epsilon_{min} = 3$ pc, consistently with our particle mass resolution. Meanwhile, the two SMBH particle dynamics and the gas dynamics follow the local resolution of the AMR grid without any limitation.

5.2.2 Thermodynamical model

In this numerical study we adopt a simple thermodynamical model: the gas temperature follows an equation-of-state and only depends on its density, as detailed in 3.2.2. For the high-density gas, the model is based on a polytropic equation of state with various adiabatic index.

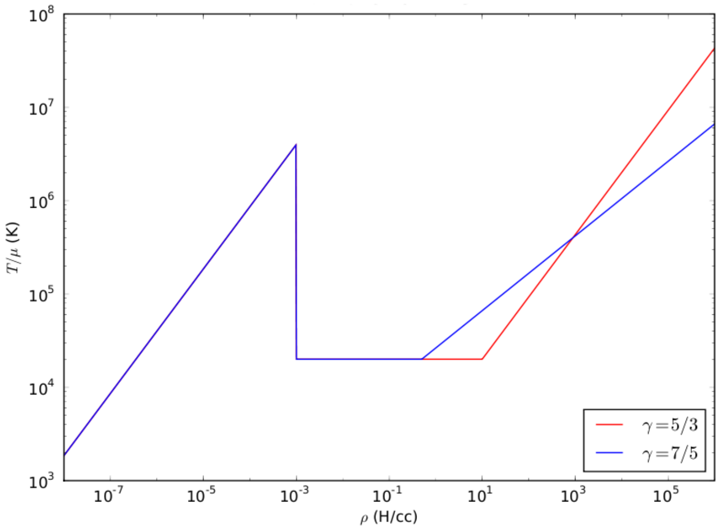

Figure 5.2: Adiabatic ($\Gamma_\mathrm{d} = 5/3$) and AGN-like ($\Gamma_\mathrm{d} = 7/5$ Spaans and Silk, 2000) polytropic equation of state for the high-density gas. For both models, the typical sound speed is $c_{\mathrm{s,d}}(n_\mathrm{d} = 10^3\ \mathrm{H/cc}) = 75\ \mathrm{km.s}^{-1}$.

At the end of the merger, the two black holes are embedded in the nuclear gas core of the remnant galaxy. The thermodynamics of this inner region is the key parameter of such a study. It is interesting to investigate the impact of various models on the black hole orbital decay. First, we assumed that a strong heating source such as an active galactic nucleus could completely shut down radiative cooling in the high-density regions, resulting in a purely adiabatic gas ($\Gamma_\mathrm{d} = 5/3$). Spaans and Silk (2000) showed that the thermodynamic state of a solar metallicity gas heated by a starburst can be well approximated by an ideal gas with adiabatic index $\Gamma_\mathrm{d} = 1.3 - 1.4$ over a wide range of densities. Consequently, we also adopted a second model for which the high-density gas is more dissipative than in the first model and follow a $\Gamma_\mathrm{d} = 7/5$ polytropic equation-of-state. For both models, using as characteristic density $n_\mathrm{d} = 10^3$ H/cc, we use the following equation-of-state across the whole disk

$$T = \max\left[10^4\ \mathrm{K}, T_\mathrm{d}\left(n_H/n_\mathrm{d}\right)^{\Gamma_\mathrm{d}-1}\right] \tag{5.1}$$

with a characteristic temperature $T_\mathrm{d} = 3 \times 10^5$ K or equivalently a characteristic sound speed $c_{\mathrm{s,d}} = 75$ km.s^{-1}.

5.2.3 Nuclear disk formation and turbulence dissipation

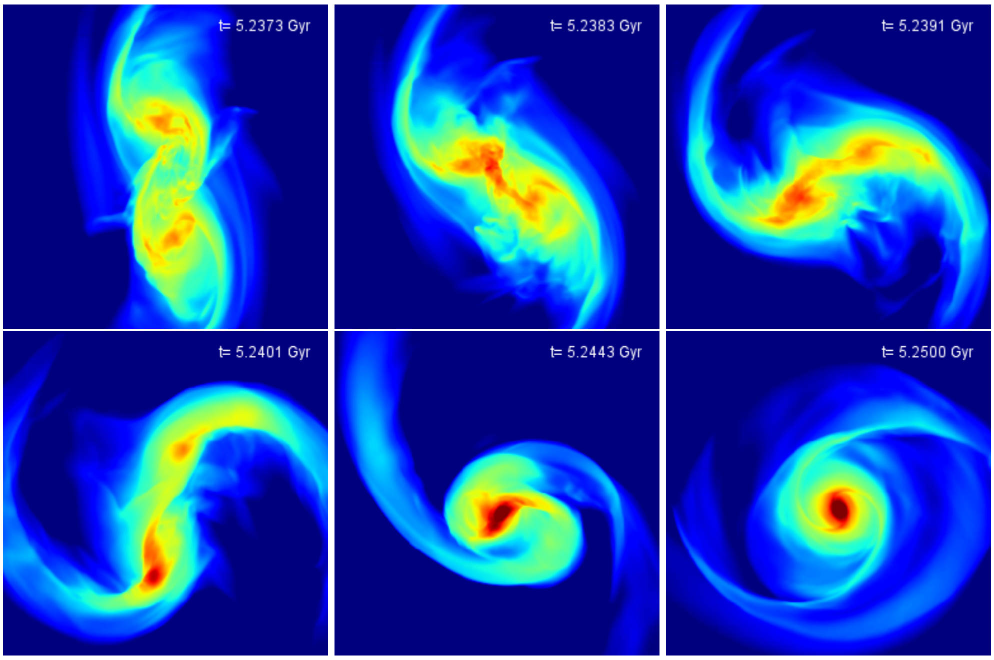

Figure 5.3: Mass-weighted gas density maps during last pericenter and final merger. The line-of-sight is perpendicular to the orbital plane and the maps are 1.8 kpc wide. While fairly symmetric before the pericenter (top left), the density distribution becomes clearly asymmetric after the pericenter (middle right). After the final merger, a $\sim 10^9\ M_\odot$ gaseous nuclear disk is formed (bottom).

A few Myr before the final merger of the two gaseous cores, during the last pericenter, the symmetry of the gas distribution changes dramatically. In figure 5.3, one can see that the gas distribution, perfectly symmetric before the last pericenter, becomes asymmetric afterwards. This is due to small scale turbulence between the two galactic cores (top left view) that made the shocks within the gas asymmetric during the last pericenter. Afterwards, one of the galactic cores (and SMBH within) ends up with a bit slower and with a little more mass than the other (bottom right view). An asymmetrical SMBH injection in the nuclear disk results from this symmetry breaking : one of the black holes is injected a few parsecs away from the nuclear disk center, while the other starts orbiting with an apocenter as large as $r \sim 100$ pc.

After an additional 4 Myr , the two galactic cores finally merge together. In the $\Gamma_{\rm d} = 5/3$ case, the core coalescence leads to the formation of a ~ 140 pc thick gas spheroid while in the $\Gamma_{\rm d} = 7/5$ case, the nuclear region is more disky with a disk thickness of ~ 60 pc. In both cases, the enclosed gas mass within 100 pc is $\sim 10^9\ M_\odot$. The parameters of the nuclear disk we obtain from this galaxy merger simulation are consistent with nuclear regions observed in Ultra Luminous Infrared Galaxies (ULIRGs; Downes and Solomon, 1998; Sanders and Mirabel, 1996), except that our model is missing the intense star formation processes of the observed nuclear regions. Figure 5.5 shows the velocity dispersion, sound speed, surface density and Toomre stability parameter maps of this disk ($\Gamma_{\rm d} = 7/5$ case). The Toomre paramter is above 1 across the whole disk. The velocity dispersion $\sigma_{\rm v}$ is dominated by the sound speed $c_{\rm s}$.

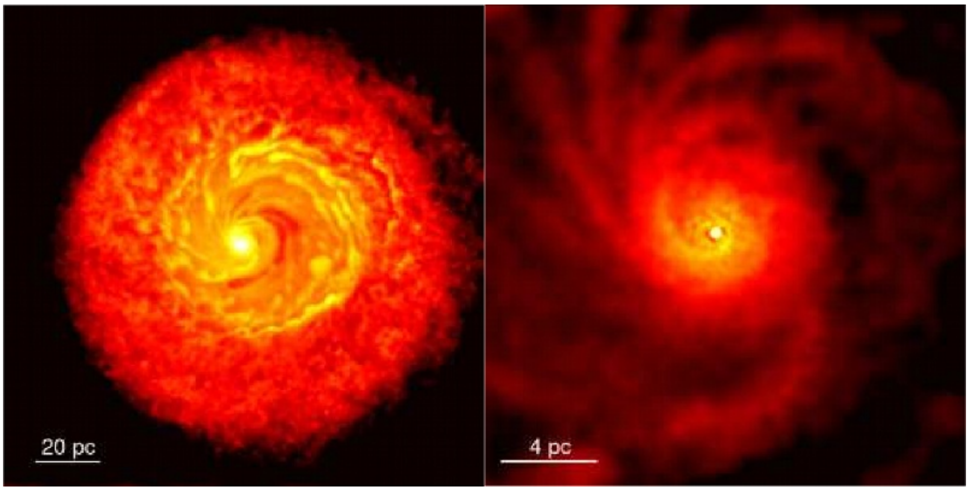

Figure 5.4: From Mayer and Kazantzidis (2008). Turbulent nuclear disk formed in the high-resolution simulation (0.1 pc and $\Gamma_{\rm d} = 7/5$) 1 Myr after the galaxy merger is deemed complete.

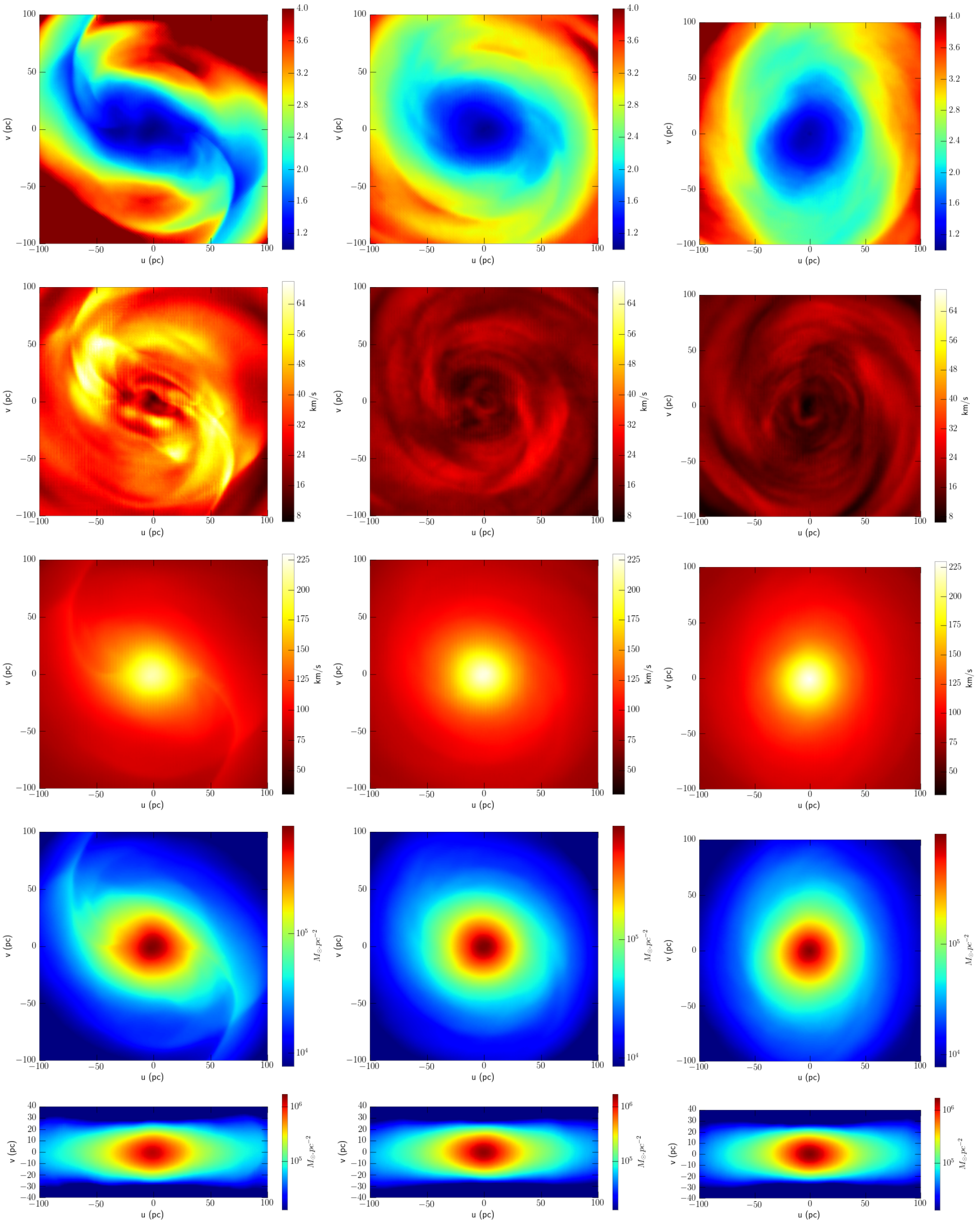

Figure 5.5: 200 pc-wide nuclear disk ($\Gamma_d = 7/5$ case) at $t(\text{Gyr}) = 5.25$ (left), 5.256 (middle) 5.2571 (right). From top to bottom are shown the Toomre parameter, velocity dispersion, sound speed, face-on and edge-on gas surface density maps.

Compared to SPH calculations made by Mayer and Kazantzidis (2008) with the same merger model, the overall properties of the disk are qualitatively in good agreement with our AMR simulations. The nuclear disk formed in the SPH simulation was however found to be marginally gravitationally unstable. This caused the formation of a strong spiral wave and the collapse of the disk as the angular momentum was driven outward. The resulting inflow was at the origin of a fast decrease of the ambient gas density around the SMBH and of the stalling of the orbital decay. Testing the robustness of this result using a different thermodynamical model and a different numerical method is precisely the main justification of the present work. A more stable nuclear disk configuration would result in a larger gas density and in a stronger drag force. In my AMR model, without any other source of turbulence than gravity, the gas velocity dispersion is quite high at the beginning, and a rather strong spiral mode can be seen in the density maps. But both the spiral wave and the turbulence are slowly dissipated from $\sigma_v \simeq 70$ km.s^{-1} to $\sigma_v \simeq 30$ km.s^{-1} (fig. 5.5, second row) in the nuclear disk, over a timescale $t_{\rm cross} = h/\sigma_v \simeq 2$ Myr. In contrast to the SPH results, we do not see a sustained transport of angular momentum outward, and the disk settles in a stable pressure equilibrium, with high gas density but also high gas sound speed ($c_{\rm s} \sim 200$ km.s^{-1}).

5.2.4 SMBHs orbital decay

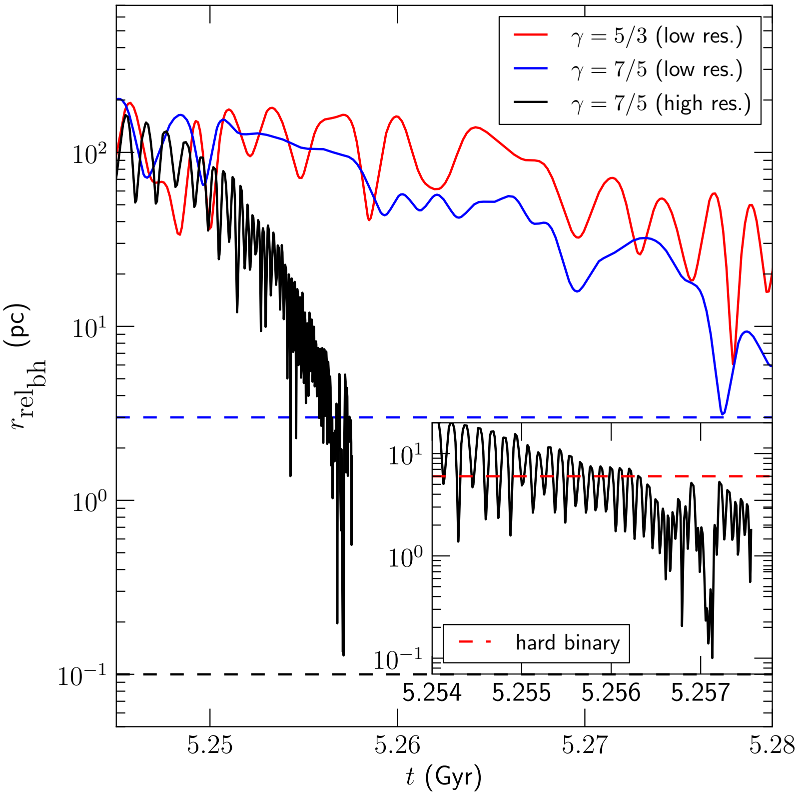

Figure 5.6: SMBH particles relative separation evolution for the low-resolution runs ($\Delta x_{min} =$ 3 pc) with $\Gamma_{\mathrm{d}} = 5/3$ (red) and $\Gamma_{\mathrm{d}} = 7/5$ (blue) and the high-resolution run ($\Delta x_{min} = 0.1$ pc) with $\Gamma_{\mathrm{d}} = 7/5$ (black). The blue (resp. black) dashed line corresponds to the low (resp. high) spatial resolution limit. The red dashed line corresponds to the black hole separation limit where the binary becomes hard ($M_{\mathrm{binary}} = 2M_{\mathrm{BH}} = M(r < 3\,\mathrm{pc})$).

We follow the evolution of the two SMBH particles in this nuclear region for the different models. Figure 5.6 shows the evolution of the black hole relative separation. The low resolution runs are in good agreement with Mayer and Kazantzidis (2008) results. While the hot ($\Gamma_{\mathrm{d}} = 5/3$) thermodynamical model leads to a stalling of the black hole orbital decay around $r \sim 40$ pc, the cold model ($\Gamma_{\mathrm{d}} = 7/5$) let the black hole relative separation falls down to the numerical resolution ($\Delta x = 3$ pc) after only 30 Myr. These first experiments are however not conclusive, since, as we will demonstrate in the next section, this resolution is too low to resolve properly the wake causing the hydrodynamical friction in the nuclear disk.

In our high resolution run, shown as the black solid line in fig. 5.6, the environment of the SMBH is much better resolved. As a consequence, the SMBH relative separation decreases from 100 pc down to 1 pc in less than 10 Myr. Although the black hole binary system reaches very briefly a relative separation close to our resolution limit ($\Delta x = 0.1$ pc), the orbital separation of the black holes is stalling well above the resolution limit and settles around 2 parsecs where the binary system becomes hard ($2M_{\rm BH} = M(r < 3\ {\rm pc})$, red dashed line). Using a different thermodynamical model than the previous SPH simulations results in a denser, more stable nuclear disk, but, as we now show in more detail, this also leads to inefficient hydrodynamical friction and failure of the model to harden the binary system down to sub-parsec scales in the center of this nuclear disk. Note however that, in our case, the dynamical friction time scale is increased by roughly one order of magnitude, so that orbital decay is not stopped entirely and SMBH pairing will probably take place after several tens of Myr. We couldn't follow the late time evolution over such a long period by lack of sufficient computational resources.

5.2.5 Dynamical friction in a gaseous medium

Figure 5.7 shows the gas overdensity induced by a SMBH particle during an orbit where the black hole is about $r = 20$ pc from the center of the nuclear disk. On each panel, the position of the black hole is marked by a black dot and the orientation is taken so that the relative velocity of the black hole in its surrounding gas is pointing rightward. The black hole induces a shock and a trailing hydrodynamical wake, which both get stronger as the black hole reach a transsonic regime where the Mach number is defined using the relative velocity of the SMBH with respect to the gas

$$\mathcal{M} = \frac{v_{\rm bh} - v_{\rm gas}(\mathbf{x}_{\rm bh})}{c_{\rm s}(\mathbf{x}_{\rm bh})} \tag{5.2}$$

The hydrodynamical wake exerts a gravitational drag on the black hole proportional to $4\pi\rho c_{\rm s}^2 R_{\rm BH}^2$, where the Bondi radius is expressed as $R_{\rm BH} = GM_{\rm BH}/c_{\rm s}^2$ (Ruffert, 1996). The true efficiency of the dynamical friction exerted by the gaseous medium on the black hole can be expressed by the dimensionless correction factor

$$f^{\rm (gas)} = \frac{F_{\rm DF}}{4\pi\rho(GM_{\rm BH}/c_{\rm s})^2} \tag{5.3}$$

In order to compare our numerical drag to these analytical and numerical estimates, we computed the gravitational force of the perturbed density field seen by the orbiting black hole particle. Figure 5.8 shows the dynamical friction dimensionless factor $f^{\rm (gas)}$. The numerical values obtained during one orbit of the distant black hole particle is in good agreement with the analytical prediction of Ostriker (1999) if we use $\ln\Lambda \simeq 3$. Deviations from the analytical model could

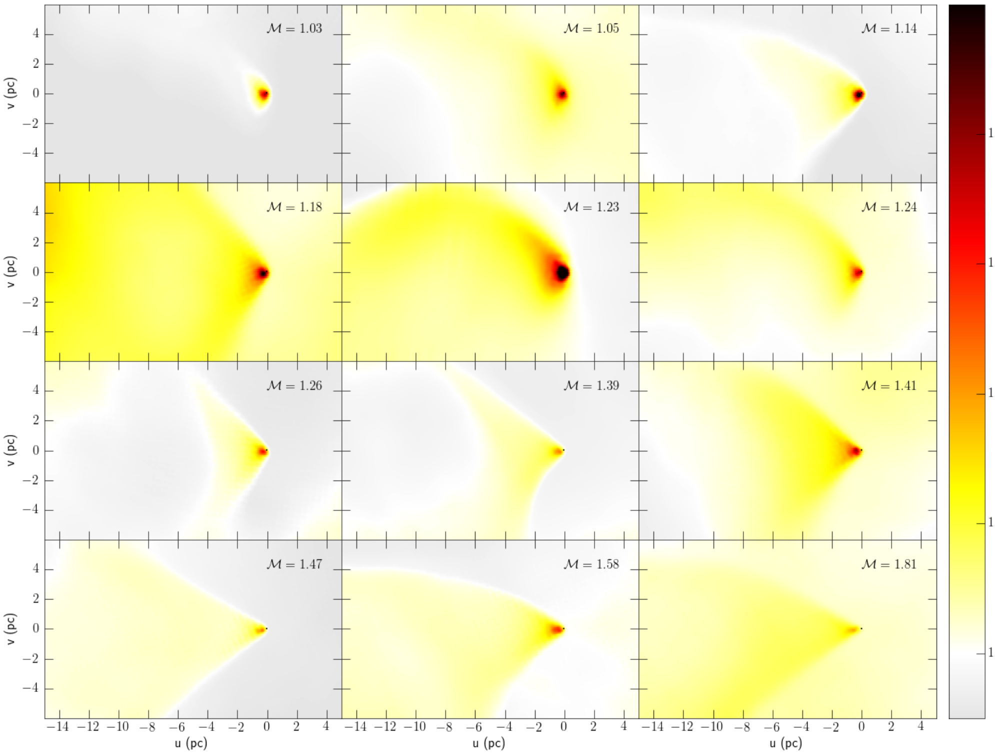

Figure 5.7: Gas Overdensity maps behind the SMBH particle (the relative velocity of the SMBH compared to the surrounding gas is pointing rightward). The hydrodynamical wakes and Mach cones are shown for increasing values of $\mathcal{M} = V_{\mathrm{bh/gas}}/c_{\mathrm{s}}$. These wakes are clearly stronger and make the dynamical friction much more efficient when the black hole is in a transsonic regime ($\mathcal{M} = 1.14, 1.18, 1.23$).

be easily explained by the time-dependent nature of the SMBH orbit, while the theory of Ostriker (1999) is based on a strictly stationary flow around the black hole.

In Figure 5.9, we plot the fractional contribution to the total gravitational drag of plane-parallel slabs of gas perpendicular to the propagation axis of the BH. In this plot, the x-coordinate is the distance of each slab (of size 3 pc) to the BH. We see immediately that for various Mach numbers, the maximum radius that contributes to the drag force is roughly $r_{\mathrm{max}} \simeq 2.5$ pc. Moreover, the fractional drag profile is well resolved by the cell size of our simulation, which quite naturally corresponds to the minimum scale that contributes to the drag $r_{\mathrm{min}} \simeq 0.1$ pc. From these two numbers, we can estimate the Coulomb logarithm in our simulation as $\ln \Lambda = \ln r_{\mathrm{max}}/r_{\mathrm{min}} \simeq \ln 25 \simeq 3.2$. We see in Figure 5.8 that the analytical model of Ostriker (1999) using $\ln \Lambda = 3$ (red) or $\ln \Lambda = 3.5$ (green) is a perfectly good fit to our numerical data. From Figure 5.9, we see that resolving the SMBH environment with sub-parsec resolution is mandatory

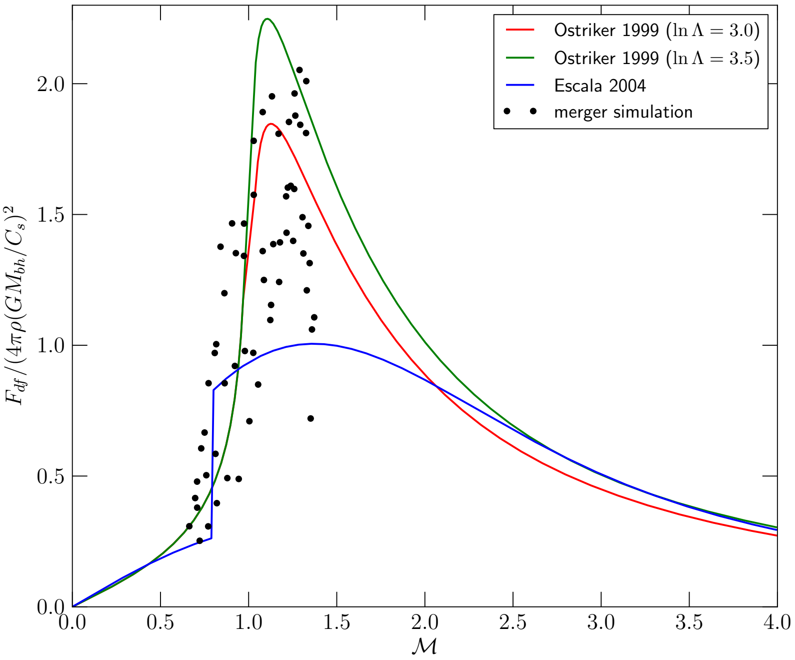

Figure 5.8: Dimensionless factor $f^{(\mathrm{gas})}$ of the dynamical friction force as a function of the Mach number $\mathcal{M} = v_{bh/gas}/c_{\mathrm{s}}$. Analytical prediction by Ostriker (1999) for a Coulomb logarithm $\ln \Lambda = 3$ (red) and $\ln \Lambda = 3.5$ (green) compared to numerical results from Escala et al. (2004) (blue) and this work (black dots), corresponding to a numerical Coulomb logarithm $\ln \Lambda \simeq 3.2$.

in order to resolve the wake properly. At Mach number slightly above unity, the wake profile sharply declines towards the BH position, and even higher resolutions would probably result in a stronger drag force, by effectively raising the value of the Coulomb logarithm.

5.2.6 A transition from fast to slow orbital decay

Let us consider a simple model of orbital decay. Assuming that the black hole evolves on circular orbits with circular velocity $v_{\mathrm{circ}}(r)$ and undergoes a hydrodynamical friction force opposite to its velocity vector and of amplitude F_{df}. The BH angular momentum writes

$$L = M_{\mathrm{BH}} r v_{\mathrm{circ}} \tag{5.4}$$

and the angular momentum losses write

$$\dot{L} = |\mathbf{r} \times \mathbf{F}_{\mathrm{df}}| = -rF_{\mathrm{df}} \tag{5.5}$$

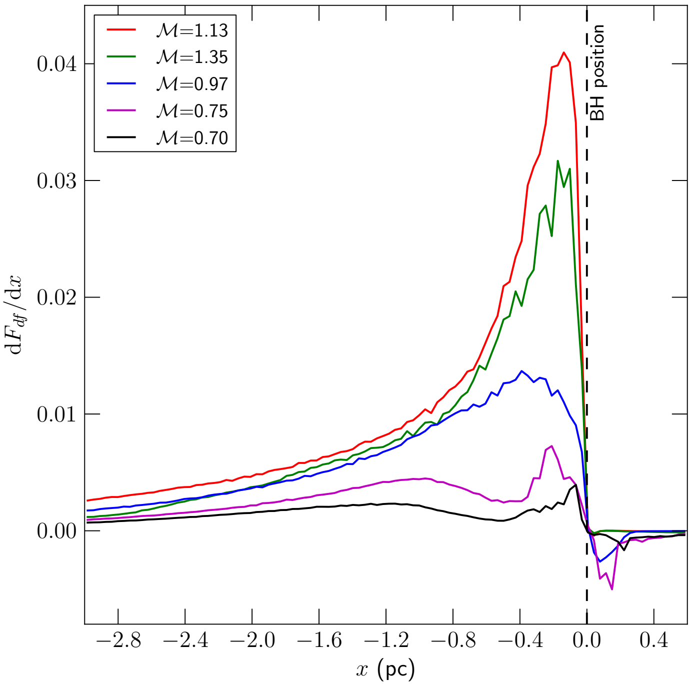

Figure 5.9: Spatial contribution to the gravitational drag the gas exerts on the black hole particle at different Mach number. The strength of the drag peaks around transsonic regime ($\mathcal{M} = 1.13$, red).Whatever the Mach number, most of the gravitational drag comes from the $2 - 3$ pc region trailing behind the black hole.

We can derive the orbital decay timescale as

$$\tau_{\mathrm{od}} = \frac{L}{\dot{L}} = \frac{M_{\mathrm{BH}} v_{\mathrm{circ}}}{F_{\mathrm{df}}} \tag{5.6}$$

When the BH is evolving at large radii, say 20 pc, the gas density is rather low, $\rho = 6 \times 10^5$ H/cc, as is the gas sound speed with $c_s = 230$ km.s^{-1}. The Mach number of the BH relative speed is however measured in the simulation to be Mach $\simeq 1.2$, which, using the Ostriker (1999) formula into eq. 5.6 results in a rather fast orbital decay with $\tau_{\mathrm{od}}(r = 20 \text{ pc}) \simeq 1$ Myr, quite consistent with the orbital evolution of the BH seen in fig. 5.6. When the black hole falls within the innermost $r = 5$ pc of the nuclear disk, its relative velocity drops below 100 km.s^{-1} while the local sound speed reaches $c_{\mathrm{s}} = 310$ km.s^{-1}. In this strongly subsonic regime, the drop of $f^{(\mathrm{gas})}(r < 5 \text{ pc}) \simeq 0.05$ is not compensated by the increase of the ratio ρ / c_{s}^2 and the orbital decay timescale rises to $\tau_{\mathrm{od}}(r \sim 1 \text{ pc}) \simeq 10$ Myr. This explains why the orbital decay at parsec scales shown in figure 5.6 is slowing down significantly. While the BH is sinking towards the center of the nuclear disk, its orbit is getting more and more circular, as found by Dotti et al. (2006, 2007). This will reduce the relative velocity of the BH with respect to the gas disk even more, and strengthens the robustness of our conclusion, namely that BH pairing in a stable, pressure-supported, nuclear disk is a rather slow mechanism.

The issue of gap-opening is an important point in the process of black hole binary formation and its final coalescence. If the black holes are able to open a circumbinary gap, the density of the gas sourrounding the black holes drops significantly and dynamical friction is no longer efficient to make the binary separation decrease even further. One can determine the gap-opening criterion by comparing the gap-closing and gap-opening times as it has been done in the context of planetary rings (Goldreich and Tremaine, 1982). In our nuclear disk of thickness $h = 60$ pc, the black hole mass gap-opening criterion can be written (Escala et al., 2005, eq. 6)

$$M_{\rm BH} \geq \sqrt{\frac{\Delta r/h}{4\pi \mathcal{M} f^{(\rm gas)}(\mathcal{M})}} \left(\frac{h}{r}\right) M(<r) \tag{5.7}$$

When the two black holes fall into the innermost 5 pc, $\mathcal{M} \simeq 0.15$ and $f^{(\rm gas)}(\mathcal{M}) \simeq 0.05$. As shown in the previous section, the black hole should clear a gap of typical size $\Delta r \simeq 2.5$ pc to prevent the formation of a hydrodynamical wake and make the dynamical friction inefficient. Consequently, the black hole critical mass is $2 \times 10^8\ M_\odot$, well above the mass of our black hole particle which could never open a gap in such a nuclear disk. Even if a Bondi-Hoyle accretion modeled was taken into account in the simulation, Callegari et al. (2011) showed that, in minor merger simulations, one of the black hole could grow by nearly an order of magnitude in mass at the most, which would not be enough for our $2.5 \times 10^6\ M_\odot$ black hole to reach the critical mass. However, since the observed black hole masses range from 10^6 to a few $10^9\ M_\odot$, the formation of a circumbinary gap by a more massive black hole is possible in our disk.

5.3 Conclusions and discussion

This numerical study is the first one that uses an AMR code to address the formation of a nuclear gas disk resulting from an equal-mass dissipative galaxy merger and the concurrent formation of a SMBH binary at parsec scales within such a disk. My results confirm previous findings of SPH simulations with the `GASOLINE` code, with particle splitting that started from very similar initial conditions (Mayer et al., 2007; Mayer and Kazantzidis, 2008). After the initial asymmetric black hole injection following the final merger of the galactic cores, the dynamical friction from the gaseous background dominates the one due to the stellar background and makes the black hole separation fall from 100 pc to a few parsecs in less than 10 Myr, in qualitatively good agreement with Mayer et al. (2007) results. Indeed, in the reference simulation adopting a polytropic equation of state with $\Gamma_{\rm d} = 7/5$, the mass, size and typical density of the nuclear disk that arises (respectively, $\sim 10^9 M_\odot$ and 60 pc) are extremely close to those of the nuclear disk in Mayer et al. (2007), as is its characteristic temperature. Due to the polytropic equation-of-state we adopted for the high-density gas ($\Gamma_\mathrm{d} = 7/5$), the nuclear disk is hot, its thickness is $\sim$ 60 pc consistently with observed nuclear regions in ULIRGs and the flow is laminar (the turbulence generated by the collision of the galaxy cores is rapidly damped). Being embedded in a background with properties similar to that in the Mayer et al. (2007) calculations, in particular with comparable density and temperature, the pair of SMBHs sinks by dynamical friction very rapidly after the merger, and becomes bound also at a similar separation, about 6 pc. We have also run two lower resolution simulations with different polytropic indexes, one with $\Gamma_\mathrm{d} = 7/5$ as in the reference run and another one with $\Gamma_\mathrm{d} = 5/3$; the comparison shows the same trend found by Mayer et al. (2007), namely that with a stiffer EOS ($\Gamma_\mathrm{d} = 5/3$) the orbital decay is slower, both because the decay regime is more subsonic and because the gaseous background has a lower characteristic density, both effects going in the direction of reducing dynamical friction.

At a closer inspection, there are however some differences between the SPH nuclear disks of Mayer et al. (2007) and that in the new `RAMSES` simulations presented in this paper. First, the disk in the SPH simulations displayed a stronger spiral structure since its appearance, as a result of a higher central surface density and thus a stronger self-gravity (the Toomre parameter was close to 1.5 while $\geq$ 2.0 in our disk, see top row of fig. 5.5). The stronger spiral modes lead to a more effective transfer of angular momentum and thus a continuously increasing central density. Second, the level of non-thermal motions in the gas, usually termed "turbulence", was a factor of about 3 higher than in the `RAMSES` run ($\sim$ 100 km.s^{-1} instead of $30 - 40$ km.s^{-1}), likely as a result of the stronger self-gravitating response. The reason for these differences are not clear. The higher numerical viscosity in the SPH runs, due to the use of explicit Monaghan artificial viscosity, especially the quadratic term in shock dissipation during the merger, is expected to dissipate gas motions into thermal energy. This would damp the turbulence faster, at odds with the higher turbulence seen in the SPH simulation, but would also generate viscous transport of angular momentum, leading to an increase in central density and therefore a higher susceptibility to gravitoturbulence, at least in the innermost region. Another possible cause of the difference is the fact that in the `GASOLINE` runs of Mayer et al. (2007) the energy equation was solved, including shock dissipation via artificial viscosity, possibly producing a nuclear disk with lower entropy immediately after the merger relative to the `RAMSES` runs adopting a fixed polytropic equation of state which does not account, by construction, for entropy dissipation in shocks. Finally, as we explain below, resolution in SPH and AMR runs is not guaranteed to be identical even if the setup is designed to be as close as possible as in the case that we are discussing.

The exact timescale of the sinking of the SMBH binary is however dependent on resolution, as was also noticed in Mayer and Kazantzidis (2008), in particular becomes shorter for increasing resolution. At higher resolution the dynamical friction wake is better resolved as density gradients are better captured, this being a likely reason behind the faster dynamical friction timescale (in collisionless systems an analogous resolution dependence of dynamical friction, mediated by gravitational softening, has been reported extensively in the literature, see e.g. Colpi et al. (1999). The formation of a front shock and a trailing hydrodynamical wake which exerts a gravitational drag on the black hole, the so called dynamical friction wake, is a remarkable result of our `RAMSES` simulations. The `RAMSES` simulations presented in this paper are indeed the first that allow to capture the wake of dynamical friction very clearly in a highly dynamic situation such as that of a nuclear disk arising from merging galaxies. We show that this gravitational drag is due to overdense gas within $2-3$ pc behind the black hole and that the efficiency of the hydrodynamical friction peaks at transonic regime, in fair agreement with the analytical prediction from Ostriker (1999). Although we did not prove that the dynamical friction wake structure has already converged, the fact that it is very clearly resolved, while it was not in previous calculations conducted with SPH simulations, prompts us to believe that our results are quantitatively more robust than those in previous works.

Our `RAMSES` simulations, owing to the aggressive refinement enabled by the AMR technique, allow to reach a spatial resolution of 0.1 pc in the center of the disk where the SMBHs are sinking, which is ten times better than the nominal resolution in Mayer et al. (2007). We caution, however, that comparing the resolution in AMR and SPH is not straightforward. In particular, it in the SPH simulations of Mayer et al. (2007) and Mayer and Kazantzidis (2008) we adopted a fixed gravitational softening in the high resolution region after particle splitting, which can thus be considered the actual limit of spatial resolution in those calculations (the SPH smoothing length being smaller in high density regions due to the large number of particles employed). In `RAMSES` the gravitational force resolution is not fixed, rather it is tied to the cell size, therefore it shrinks as the refinement is applied to the cells , a situation more reminiscent of what happens with SPH codes adopting an adaptive softening length (e.g. Bate and Burkert, 1997). We notice that in Mayer and Kazantzidis (2008) a run was presented with a maximum spatial resolution, in terms of gravitational softening, comparable to the highest resolution simulation presented here; although the simulation was carried out only for a few orbits after the black holes have formed a binary rather than for many orbits as in the `RAMSES` simulations presented here, in both cases the separation of the SMBHs appears to fluctuate significantly, with no clear signs of sustained decay below parsec separation. Below such separation it is expected that dynamical friction will become inefficient because the mass of the gaseous background enclosed within the orbit of the two SMBHs becomes smaller than the mass of the SMBH binary. In addition, in the innermost 5 pc of the nuclear disk, the sound speed reaches ~ 300 km.s^{-1}, a subsonic regime for the motion of SMBHs, which also implies an inefficient dynamical friction. In polytropic equilibrium models of nuclear disks, Escala et al. (2004) reported an asymmetric torque due to an ellipsoidal deformation of the density distribution around the binary, which extracted angular momentum from the binary allowing it to shrink further. This is not seen here nor in the previous SPH simulations of some of us. One reason might be that the thermodynamical conditions and density profile of the disk that develops here are different from those in equilibrium disk models. In particular, the system analyzed by Escala et al. (2004) had a sound speed of about 60 km.s^{-1} even at the center, hence it was a much colder gas disk than ours. On the other hand, a colder disk could act against the decay in two ways, namely by driving a stronger mass inflow by gravitational torques that steepens the central density on a dynamical timescale and might thus evacuate the gas around the black hole binary, or might provide more favourable conditions for the opening of a gap by the binary after it has become bound. Finally, it is important to note that binary decay stalls around $2-3$ pc, a separation at which the orbital evolution might not be correctly captured with only ~ 20 AMR cells. A similar resolution problem, as well as possible associated issues with orbit integration accuracy, might have been present also in the previous SPH calculations.

Our findings thus suggest that, as in the case of purely stellar backgrounds, a continued decay towards the gravitational wave regime is not automatically achieved in a gaseous background. However, concluding that there is a last parsec problem in gaseous backgrounds is highly premature. First of all, while the strength of our models, relative to other studies adopting idealized nuclear disks, relies in the realistic disk conditions inherited by the galaxy merger, there are still several important simplifications and omissions in the physics at play. First, as in Mayer et al. (2007) and Mayer and Kazantzidis (2008), we considered a single phase medium described by an effective EOS. In reality the nuclear disk will host a complex multi-phase ISM, with possibly a highly inhomogeneous density structure (e.g. Wada and Norman, 2001). Star formation and supernovae feedback will provide both diffuse and localized heating sources, and if the black holes are active as AGNs during one or more phases of the merger they would likely change the initial conditions of the nuclear disk arising after the merger (i.e. change its density and thermal structure, both being crucial for dynamical friction). Ongoing work with a new multi-phase ISM, star formation and feedback scheme, for the moment implemented only in `GASOLINE` , will soon provide a clue on the importance of such complexity in the sinking rate of the SMBH binary (Roskar et al., in preparation). Furthermore, allowing for star formation to happen in the nuclear disk, another missing ingredient, will have an impact since stars can aid the decay in regions where the gas becomes inefficient, as long as stars move on sufficiently non circular orbit with respect to the frame of the binary, in order to keep the loss cone continuously filled (Preto and Amaro-Seoane, 2010; Khan et al., 2011). Indeed, in a massive self-gravitating disk such as the one obtained here, stars would likely exhibit centrophilic orbits as a result of non-axisymmetric instabilities. One can image thus a multi-stage decay, in which gas is the leading drag source down to parsec scales, owing to its very efficient action demonstrated here (Mayer et al., 2007), and stars might take over at smaller separations. Future calculations capable of capturing both a realistic multi-phase gaseous medium and the full stellar dynamical response including three-body interactions between the binary and the stars at small scales mark the necessary next frontier that will be needed to progress further in understanding the shrinking of SMBH binaries well below parsec scales.

CHAPTER 6

PyMSES: Python analysis toolbox for `RAMSES` data

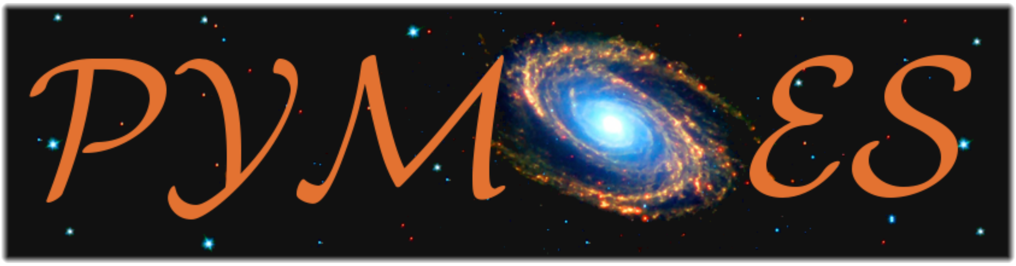

Following Moore's law (Moore, 1965), the computational power of worldwide supercomputing facilities have increased exponentially in the past decades. To make good use of this supercomputing power, astrophysicists and numericians have developed massively parallel numerical codes to perform astrophysical simulations of growing size and complexity in the same period :

- MareNostrum simulation (Ocvirk et al., 2008)
- Aquarius project (Springel et al., 2008)
- Millenium simulation (Springel et al., 2005)
- Horizon simulation (Teyssier et al., 2009)
- Via Lactea simulation (Kuhlen et al., 2008)
- SNe Ia simulations (Almgren et al., 2010)
- Bolshoi simulations (Klypin et al., 2011)

But all these ambitious numerical projects will produce higher and higher volumetry data. In the next decade, the greatest challenges for the computational astrophysicists will be less related to the physical processes involved than in these two technical issues: data access and data processing. In the years to come, the data transfer speed might become the bottleneck in every numerical project. Furthermore, the software tools to examine data strongly lack of usability and their performance have not kept pace with the explosion of the supercomputing power.

However, a few projects of massively parallel visualization tools such as VisIT[1], Mayavi[2] and ParaView[3] have been created to fill that void. But these multi-purpose tools are quite general and often require a conversion of the data format into a more standard format like, for example, VTK[4]. In astrophysics, there are a few domain-specific analysis software. Some dedicated visualization tools must be mentioned such as VAPOR[5], SDVision[6] or Glnemo[7], although they focus more on visualization than data processing functionalities.

Along with `RAMSES` are provided a large set of low-level I/O and basic analysis routines, written in Fortran90 or IDL[8]. The `RAMSES` community investigate a wide range of astrophysical applications: accretion disks, SN explosions, galaxy formation, pre-stellar core collapse, ISM fragmentation, galaxy mergers and large scale structure formation on cosmological scales. Although these different groups of researchers use the same astrophysical code and consequently the same data format, they don't need to perform the same analysis on the simulation outputs. As a consequence, each group (or even each researcher) develops its own specific analysis scripts by adapting the default low-level routines to its own needs. Every analysis script needs to read data from disk, assemble it in memory, convert units, select subsections of that data, perform some type of quantitative analysis, and then output a reduced data product. The first four steps of this process are common to every group but require a fair knowledge of the `RAMSES` code and its data format. This unproductive and constant reinvention of the wheel by different research group in the `RAMSES` community motivated the development of a unified tool for data access and processing called PyMSES.

At the same time, an identical motivation leaded to a similar application in California, called `yt`[9] (Turk et al., 2011). Initially developed to examine slices and projected regions through deeply nested adaptive mesh refinement (AMR) cosmological simulations conducted with the `Enzo` code, it was quickly repurposed to be a multi-code mechanism for data analysis and visualization. Although `yt`'s aim is to provide a flexible and cross-code software package for AMR applications, it is not optimized for the octree data structure of `RAMSES` compared to the dedicated tool presented in the next section.

---

[1] `https://wci.llnl.gov/codes/visit/`

[2] `http://pypi.python.org/pypi/mayavi/`

[3] `http://www.paraview.org/`

[4] `http://www.vtk.org`

[5] `http://www.vapor.ucar.edu/`
Visualization and Analysis Platform for Ocean, atmosphere and solar Researchers

[6] `http://irfu.cea.fr/Projets/COAST/visu.htm`

[7] `http://www.oamp.fr/dynamique/jcl/glnemo/index.fr.html`

[8] `http://www.ittvis.com/language/en-US/ProductsServices/IDL.aspx`

[9] `http://yt.enzotools.org`

6.1 Introduction

PyMSES is a set of Python[10] modules designed for `RAMSES` data processing. It provides a set of tools to help `RAMSES` users read their simulation data transparently and assemble the data in memory. By using PyMSES, the expert knowledge about domain decomposition, AMR data structure or Fortran90 binary formatting is no longer mandatory. It is written in Python but several routines have been developed in C or Cython[11] for better I/O performance and faster computation. As any Python module, PyMSES can interface with a lot of powerful (and already available) Python libraries such as Numpy[12]/Scipy[13], Matplotlib[14], PIL[15] and HDF5[16]/PyTables[17].

The purpose of PyMSES is to be a post-processing toolbox for `RAMSES` user's own scientific analysis. It is not an interactive environment by itself, but it provides modules which can be used interactively, for example with IPython[18]. To encourage simulation monitoring and data exploration of the `RAMSES` simulation outputs, a visualization graphical user interface (GUI) called AMRViewer has been developed as a sub-module of PyMSES. The strong decoupling proposed in PyMSES between data I/O and scientific analysis allows the user to focus on its specific science rather than technical details.

I co-developed PyMSES initially with Thomas GUILLET and more recently with Marc LABADENS on parallelization and optimization of visualization algorithms.

The present chapter only focus on the functionalities and performances of the visualization module. For full documentation on the data I/O, unit conversion, subselection via data filters and all the other functionalities implemented in PyMSES, see `http://irfu.cea.fr/Projets/PYMSES/intro.html`. In the next sections, basic visualization functionalities are illustrated by a few examples and the early results of a parallelization benchmark will be presented.

---

[10] `http://python.org`
[11] `http://cython.org`
[12] `http://www.numpy.scipy.org`
[13] `http://www.scipy.org`: scientific computing library.
[14] `http://matplotlib.sourceforge.net` : 2D plotting library.
[15] `http://www.pythonware.com/products/pil/` : imaging library.
[16] `http://www.hdfgroup.org/HDF5/`
[17] `http://www.pytables.org/` for hierarchical datasets format I/O.
[18] `http://ipython.org`

6.2 From 3D data to 2D projections

PyMSES provides a visualization module to compute 2D maps out of 3D data. Two different methods have been implemented in this module: ray-casting into the AMR grid and fft-convolution.

6.2.1 Ray-casting, Hilbert domain decomposition and minimal cubic paving

The first method is a standard ray-casting method. Althoug the use of this method has a high computational cost, PyMSES takes advantage of the grid-based AMR data structure to optimize the selection of intersecting rays with the AMR cells. The optimization is based on a *minimal cubic paving* of the Hilbert domain decomposition (see fig. 6.1) that summarize each CPU domain containing millions of AMR cells into a reduced number ($\sim 10 - 10^2$) of cubic blocks .

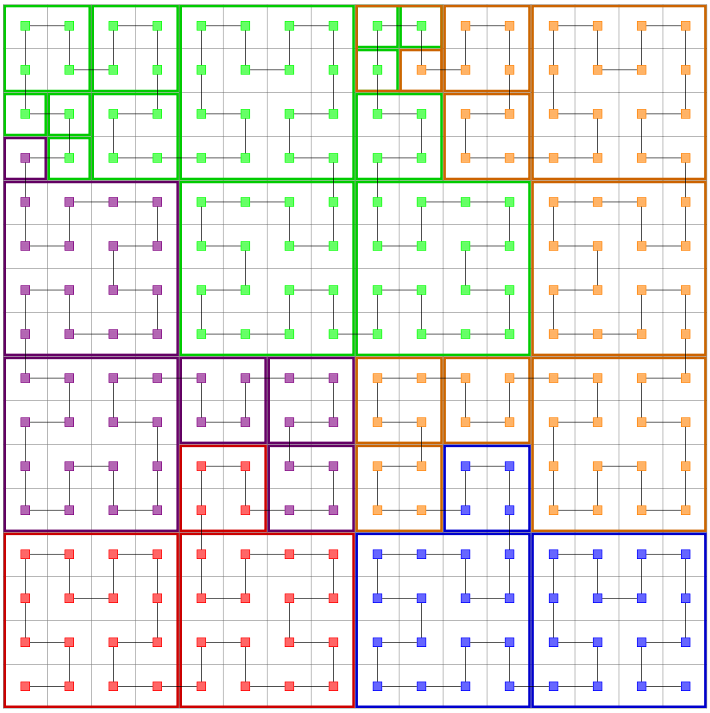

Figure 6.1: 2D Hilbert domain decomposition minimal cubic paving example. The 2D Hilbert domain decomposition of a 16X16 grid is the one of fig. 3.3. The large thick squares correspond to the minimal cubic paving of the domains: 256 cells or only 33 squares form a partition of the simulation domain.

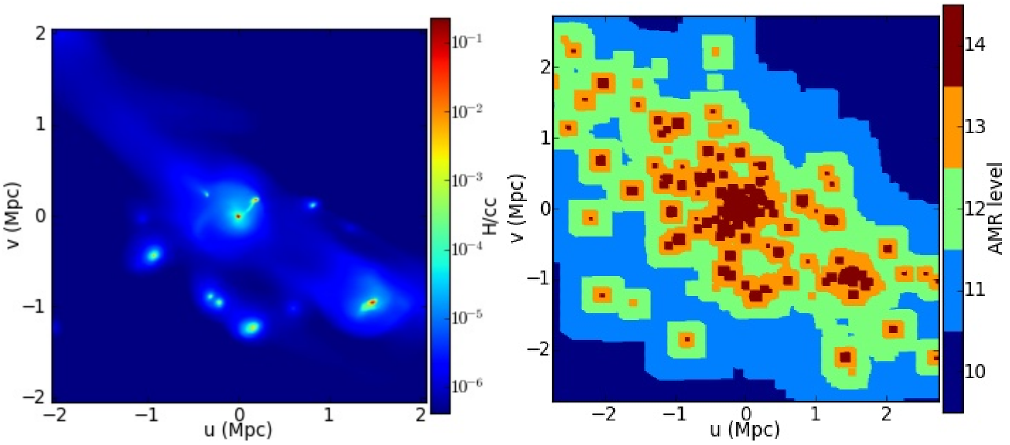

Figure 6.2: Examples of ray-casted maps created with the visualization module of PyMSES. (left) Mass-weighted gas density maps of a comological filament with galactic disks. (right) Maximum AMR level of refinement along the line-of-sight map.

6.2.2 FFT-convolution

The visualization module provides a faster projection method, often referred to as *splatter*. It provides a unified projection method for both AMR grid data and particle data and works on a level-by-level basis. First, it only requires straightforward 2D binnings of the particle/AMR cell distribution along the line-of-sight axis. In a second step, convolutions of the resulting maps by 2D gaussian convolution kernels ($\sigma \propto \Delta x_{\mathrm{AMR}}$) via FFT algorithm. Finally, all the level are stacked to obtain the projected map.

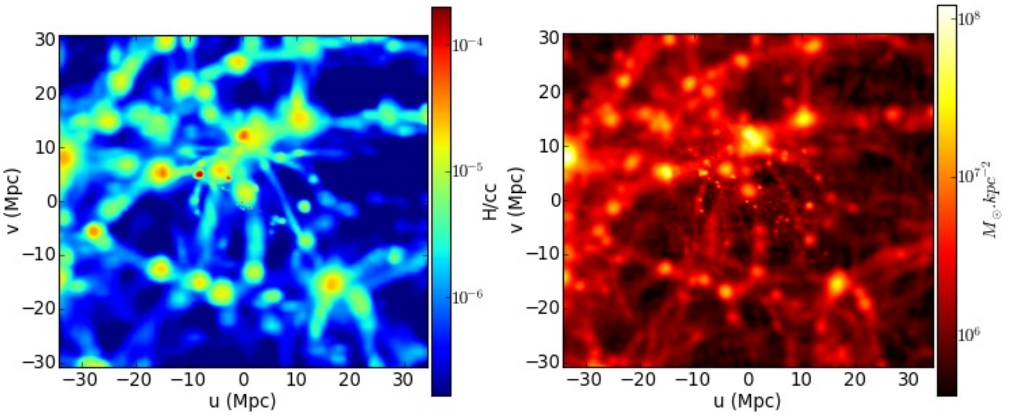

Figure 6.3: Examples of fft-convolved maps created with the visualization module of PyMSES. (left) Mass-weighted gas density (AMR) maps of a comological simulation. (right) Dark matter (particles) surface density map of the same region, showing the clusters and filaments.

6.2.3 The AMRViewer GUI

These projection algorithms have been plugged in a graphical user interface named AMRViewer. Among other functionalities, this interface allows the user to navigate through RAMSES data outputs, to dive into the AMR grid (zoom in/out) and visualize its content along any projection axis in a semi-interactive way. The user can also load/save view parameters from/to a *Camera* configuration file, explore the content of the maps via a magnifier tool and even perform some distance measurements on the maps.

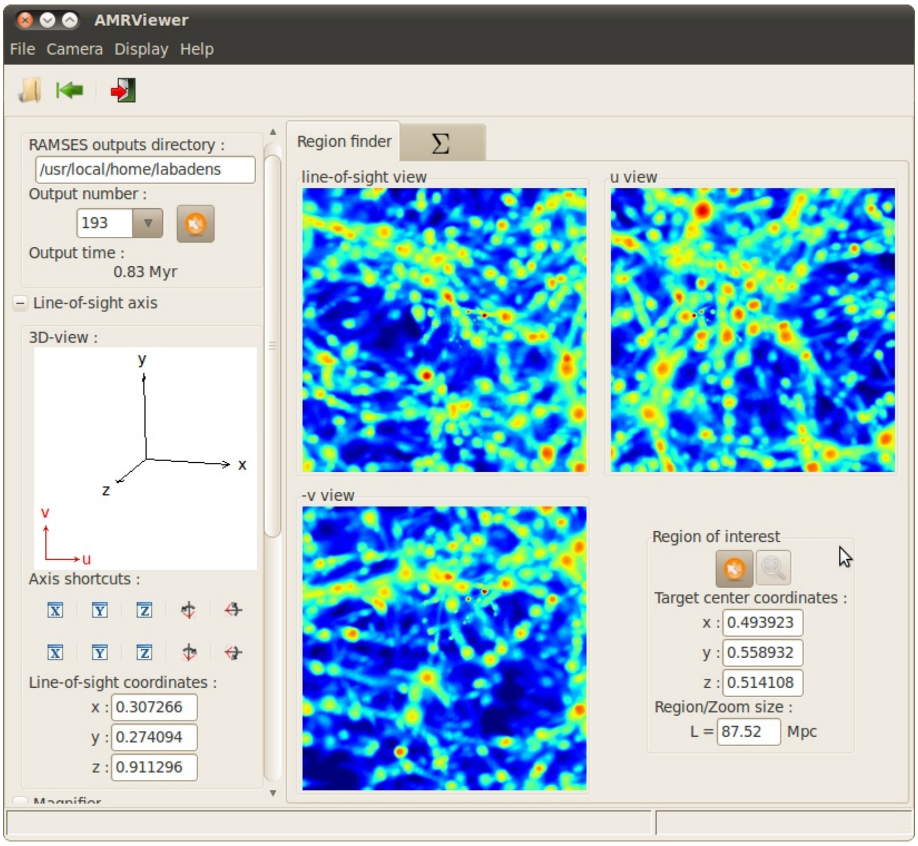

RAMSES outputs directory : /usr/local/home/labadens
Output number : 193
Output time : 0.83 Myr

Line-of-sight coordinates :
x : 0.307266
y : 0.274094
z : 0.911296

Target center coordinates :
x : 0.493923
y : 0.558932
z : 0.514108
Region/Zoom size :
L = 87.52 Mpc

Figure 6.4: AMRViewer graphical user interface for RAMSES simulation monitoring and data exploration.

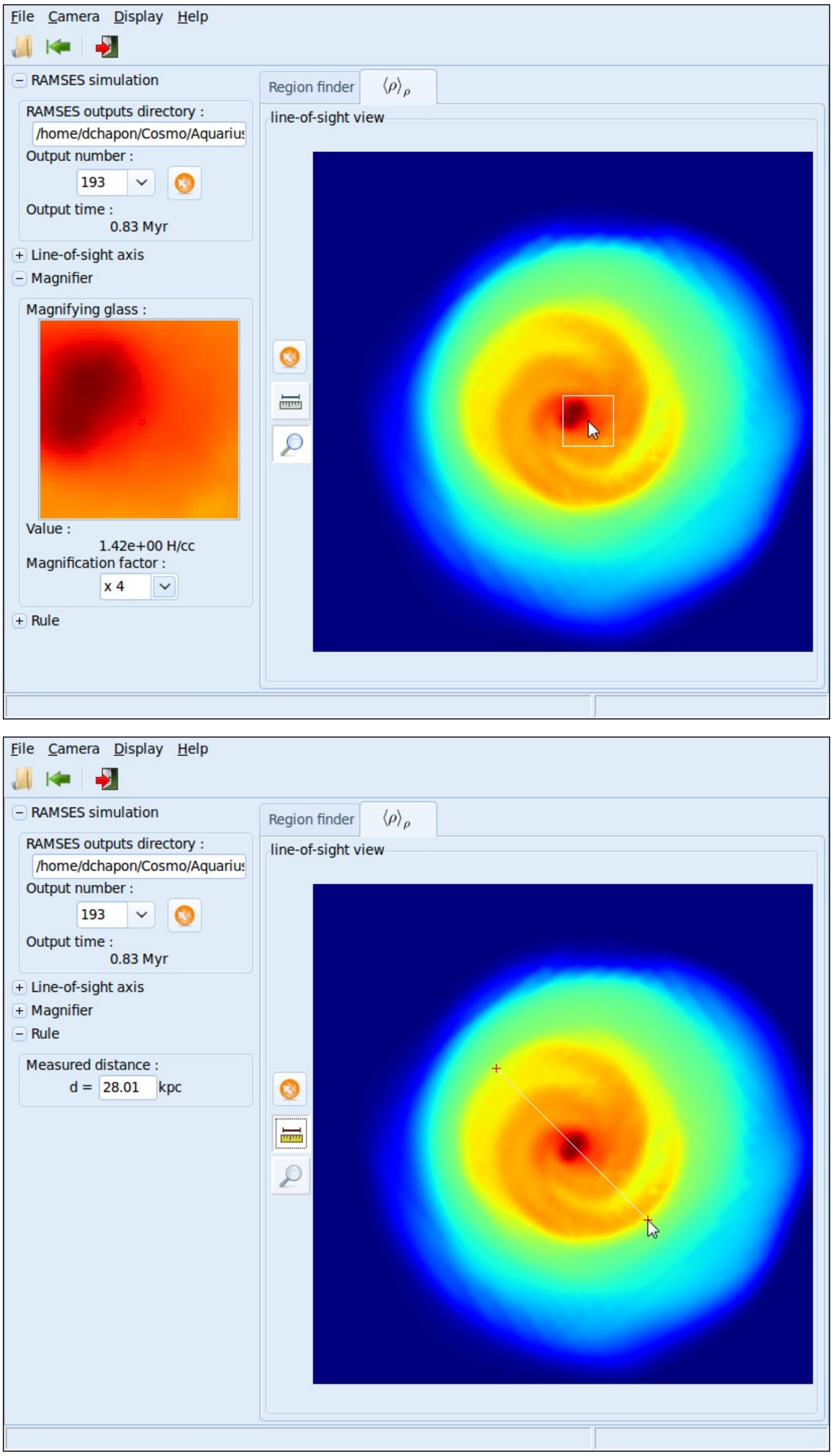

RAMSES outputs directory : /home/dchapon/Cosmo/Aquariu

Output number : 193

Output time : 0.83 Myr

Value : 1.42e+00 H/cc

Magnification factor : x 4

RAMSES outputs directory : /home/dchapon/Cosmo/Aquariu

Output number : 193

Output time : 0.83 Myr

Measured distance : d = 28.01 kpc

Figure 6.5: *Magnifier* (up) and *rule* tools (down) in the AMRViewer GUI.

6.3 I/O and visualization parallelization benchmark

The decomposition of the simulation domain into N_{cpu} CPU domains in `RAMSES` makes the parallelization of the post-processing algorithms quite straightforward. The post-processing of each CPU data can be performed by independant processes and the contribution of all CPU domains can be linearly added.

The performances of a MPI version of a ray-casting script has been tested on a fragmenting galactic gaseous disk dataset. The early results of this benchmark are shown in the fig. 6.6 and fig. 6.7. The parallelized ray-casting algorithm shows a quite good scaling, although some filesystem limitations and function overheads appeared to be responsible for the saturation towards high task numbers.

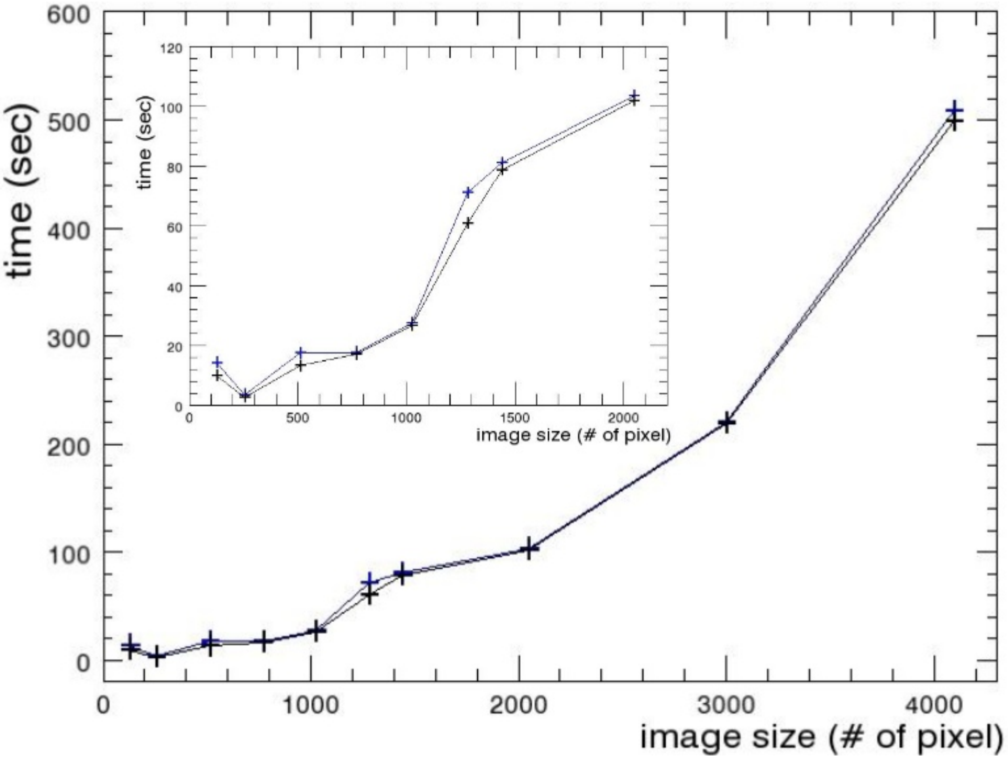

Figure 6.6: Performance benchmark of the parallel (MPI) ray-casting algorithm on 24 CPUs. Time in seconds vs. image size N. Note that the total number of rays is N^2.

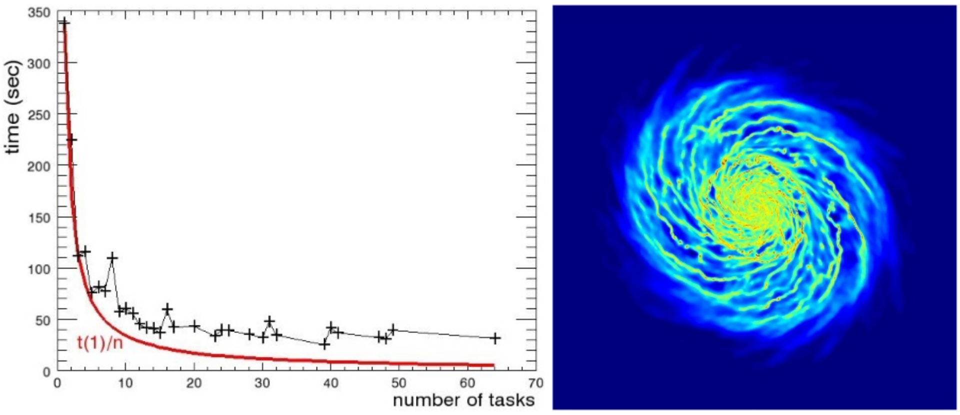

Figure 6.7: Performance benchmark of the parallel (MPI) ray-casting algorithm on a 1024x1024 image. (left) Time in seconds vs. process number. The scaling saturation toward high process number is possibly due to function overheads of filesystem I/O limitations. (right) Ray-casted gas density map of the fragmenting galactic disk.

6.4 Conclusion

The PyMSES module, developed in Python with some C core routines is very portable. It provides transparent `RAMSES` data access functionalities with a modularity that low-level Fortran90 standard routines desperately lacks and fill the need of a flexible, performant, unified data access toolbox. This user-friendly analysis toolbox is easy to interface with the user's own Python analysis modules and allows him to perform exploratory investigation without *effort surhumain*. Recent parallelization of the I/O and visualization algorithms is a smart orientation considering the increasing need of performant post-processing tools in astrophysics. The results of the performance benchmark are soon to appear in Labadens, Chapon, Pomarede, and Teyssier (2011). PyMSES is currently being used among the `RAMSES` community by $\sim$ 20 researchers and might even contribute to the wider use of `RAMSES` in the years to come.

Conclusion

Merger-driven star formation and the Antennæ galaxies

My numerical study of the Antennæ galaxy (NGC4038/39) collision leaded to a new scenario to explain the starbursting regime of merging galaxies (supposed ULIRGs). The pseudo-cooling equation-of-state thermodynamical model, providing a reasonable route of gas dissipation, enables the fragmentation of the gas disk and the increase of turbulence level in the ISM after the first pericenter. The merger-driven clustered star formation burst I observed in the high-resolution simulation is in good agreement with the ”starburst versus quiescent Kennicutt-Schmidt law” pointed out by observations. It gives weight to the argument that the observed ”starburst regime” is not due to a modification of the star formation efficiency but to an enrichment of the gas density PDF towards high densities caused by the fragmentation of the ISM into massive clouds, where star formation timescales are shorter and the integrated star formation is higher. This inhomogeneous star formation regime could not be resolved in previous numerical studies of interacting galaxies due to limited spatial resolutions and ”hot” thermodynamical models for the ISM.

Another important consequence of the merger-driven fragmentation of the ISM is the extended star formation. My high-resolution model of the Antennæ merger is still dominated by a strong gas inflow and a nuclear starburst, as observed in ULIRGs. However, the gas fragmentation results in a weaker gas inflow compared to a low-resolution model and the star formation is consequently more radially extended. This numerical evidence of extended star formation can explain why a number of observed interacting galaxies such as Arp140 or the Antennæ have SSCs forming at several kpc from their center.

SMBHs pairing in galaxy merger

I conducted the first high-resolution AMR simulation of a galaxy merger with SMBH particles to capture the small-scale hydrodynamical behaviour of the gas in the nuclear disk of the remnant galaxy. I adopted AGN-like polytropic ($\Gamma_\mathrm{d} = 7/5, 5/3$) equation-of-states for the nuclear gas leading to the formation of a hot nuclear disk with thickness ~ 60 pc ($\Gamma_\mathrm{d} = 7/5$), consistent with observed nuclear regions in ULIRGs.

In this nuclear disk, the sub-parsec resolution I adopted is sufficient to resolve the formation of a front shock and a trailing hydrodynamical wake excited by the SMBH. The wake, of size $\sim 2 - 3$ pc, exerts a gravitational drag on the black hole, cause of the black hole orbital decay. For the first time, I show that the efficiency of this gas-induced dynamical friction peaks when the black hole is in a nearly transsonic regime, in good agreement with early theoretical predictions while previous numerical studies argued it was overestimated. The dynamical friction is responsible for the SMBHs orbital decay from separation of ~ 100 pc falling down to a few parsecs in less than 10 Myr, in qualitatively good agreement with previous SPH calculations. After 10 Myr, the black hole binary hardens and we observe a transition from fast to slow orbital decay, due to the subsonic nature of the black hole velocity in the innermost 5 pc of the nuclear disk, where the black hole separation stalls around $2 - 3$ pc. As in the case of purely stellar backgrounds, I found no clear signs of sustained decay below parsec separation.

However, my thermodynamical model mimics the AGN feedback with a simple equation-of-state and doesn't take into account the highly inhomogeneous density structure of the ISM. What is more, star formation, supernovæ and AGN feedbacks, which are not enabled in this model, would likely change the density and thermal structure of the nuclear disk, key point in the black hole pairing process. Gas is the leading drag source down to parsec scales but stars might take over at smaller separations. Here, 3-body interactions with the stellar background can't be properly resolved with my limited particle resolution. Future calculations capable of capturing both a realistic multi-phase gaseous medium and the full stellar dynamical response including three-body interactions between the binary and the stars at small scales mark the necessary next frontier that will be needed to progress further in understanding the shrinking of SMBH binaries well below parsec scales.

Publications

Refereed publications

- Teyssier, R., **Chapon, D.** and Bournaud, F., *The driving mechanism of starbursts in galaxy mergers*, 2010, ApJL 720, pp. L149–L154.
- **Chapon, D.**, Mayer, L. and Teyssier, R., *Pairing and sinking of binary SMBHs in sub-pc resolution simulations of galaxy mergers*, 2011, MNRAS (submitted), Arxiv:1110.6086.
- Bournaud, F., **Chapon, D.**, Teyssier, R. and Powell, L. C., Elmegreen, B. G., Elmegreen, D. M., Duc, P., Contini, T., Epinat, B. and Shapiro, K. L., *Hydrodynamics of high-redshift galaxy collisions: from gas-rich disks to dispersion-dominated mergers and compact spheroids*, 2011, ApJ 730, pp. 4-+.
- Labadens, M., **Chapon, D.**, Pomarede, D. and Teyssier, R., *PyMSES, a RAMSES data analysis toolbox : I. I/O and visualization performance tests*, 2011, in prep.

Proceedings

- Powell, L. C., Bournaud, F., **Chapon, D.**, Devriendt, J., Slyz, A. and Teyssier, R., *Galactic star formation in parsec-scale resolution simulations*, 2011, proceedings of the IAU Symposium 270 : Computational Star Formation.
- Bournaud, F., Powell, L. C., **Chapon, D.** and Teyssier, R., *Star formation in galaxy mergers: ISM turbulence, dense gas excess, and scaling relations for disks and starbusts*, 2010, proceedings of the IAU Symposium 271 : Froms stars to galaxies.
- Powell, L. C., Bournaud, F., **Chapon, D.**, Devriendt, J., Slyz, A. and Teyssier, R., *The impact of ISM turbulence, clustered star formation and feedback on galaxy mass assembly through cold flows and mergers*, 2011, to appear in the proceedings of the IAU Symposium 277 : Tracing the ancestry of galaxies.

General public communication events & publications

Best of CEA 2010 *Intergalactic pile-up*.

CEA News *Cover page*, 11th issue, winter 2009.

Les défis du C.E.A. *Quand deux galaxies se rencontrent*, vol. 157, February 2011.

Ciel&Espace *Des flambées stellaires enfin conformes*, December 2010.

Science&Vie *Ils l'ont fait*, December 2010.

Pour la Science *Une simulation réaliste des flambées d'étoiles*, November 2010.

C.N.R.S. press release *Une simulation numérique pour expliquer les brutales naissances d'étoiles lors des fusions entre galaxies*.

C.E.A. press release *Le message des Antennes*.

Montparnasse station *Vous avez dit Univers ?* exhibit, November-December 2009.

Jardin du Trocadéro *Les mystères de l'Univers* exhibit, October 2009.

Bibliography

Agertz, O., Lake, G., Teyssier, R., Moore, B., Mayer, L., and Romeo, A. B. Large-scale galactic turbulence: can self-gravity drive the observed HI velocity dispersions? *MNRAS*, 392:294–308, 2009a.

Agertz, O., Teyssier, R., and Moore, B. Disc formation and the origin of clumpy galaxies at high redshift. *MNRAS*, 397:L64–L68, 2009b.

Agertz, O., et al. Fundamental differences between SPH and grid methods. *MNRAS*, 380:963–978, 2007.

Almgren, A., et al. MAESTRO, CASTRO, and SEDONA – Petascale Codes for Astrophysical Applications. *ArXiv*, 2010.

Arzoumanian, D., et al. Characterizing interstellar filaments with Herschel in IC 5146. *A&A*, 529:L6+, 2011.

Baldi, A., Raymond, J. C., Fabbiano, G., Zezas, A., Rots, A. H., Schweizer, F., King, A. R., and Ponman, T. J. Chemical Enrichment of the Complex Hot ISM of the Antennae Galaxies. II. Physical Properties of the Hot Gas and Supernova Feedback. *ApJ*, 636:158–171, 2006.

Barnes, J. and Hut, P. A hierarchical O(N log N) force-calculation algorithm. *Nature*, 324:446–449, 1986.

Barnes, J. E. Encounters of disk/halo galaxies. *ApJ*, 331:699–717, 1988.

Barnes, J. E. Transformations of galaxies. I - Mergers of equal-mass stellar disks. *ApJ*, 393:484–507, 1992.

Barnes, J. E. Shock-induced star formation in a model of the Mice. *MNRAS*, 350:798–808, 2004.

Barnes, J. E. and Hernquist, L. E. Fueling starburst galaxies with gas-rich mergers. *ApJ*, 370:L65–L68, 1991.

Basu, S. and Mouschovias, T. C. Magnetic braking, ambipolar diffusion, and the formation of cloud cores and protostars. 1: Axisymmetric solutions. *ApJ*, 432:720–741, 1994.

Bate, M. R., Bonnell, I. A., and Price, N. M. Modelling accretion in protobinary systems. *MNRAS*, 277:362–376, 1995.

Bate, M. R. and Burkert, A. Resolution requirements for smoothed particle hydrodynamics calculations with self-gravity. *MNRAS*, 288:1060–1072, 1997.

Begelman, M. C., Blandford, R. D., and Rees, M. J. Massive black hole binaries in active galactic nuclei. *Nature*, 287:307–309, 1980.

Bender, R. Velocity anisotropies and isophote shapes in elliptical galaxies. *A&A*, 193:L7–L10, 1988.

Bender, R., Doebereiner, S., and Moellenhoff, C. Isophote shapes of elliptical galaxies. I - The data. *A&AS*, 74:385–426, 1988.

Berczik, P., Merritt, D., and Spurzem, R. Long-Term Evolution of Massive Black Hole Binaries. II. Binary Evolution in Low-Density Galaxies. *ApJ*, 633:680–687, 2005.

Berger, M. J. and Oliger, J. Adaptive mesh refinement for hyperbolic partial differential equations. *J. Comp. Phys.*, 53:512, 1984.

Bergin, E. A. and Tafalla, M. Cold Dark Clouds: The Initial Conditions for Star Formation. *ARA&A*, 45:339–396, 2007.

Bigiel, F., Leroy, A., Walter, F., Brinks, E., de Blok, W. J. G., Madore, B., and Thornley, M. D. The Star Formation Law in Nearby Galaxies on Sub-Kpc Scales. *AJ*, 136:2846–2871, 2008.

Binney, J. and Tremaine, S. *Galactic Dynamics: Second Edition*. Princeton University Press, 2008.

Birnboim, Y. and Dekel, A. Virial shocks in galactic haloes? *MNRAS*, 345:349–364, 2003.

Block, D. L., Freeman, K. C., Puerari, I., Combes, F., Buta, R., Jarrett, T., and Worthey, G. The Hubble Tuning Fork Strikes A New Note. In D. L. Block, I. Puerari, K. C. Freeman, R. Groess, & E. K. Block , editor, *Penetrating Bars Through Masks of Cosmic Dust*, volume 319 of *Astrophysics and Space Science Library*, pages 15–+. 2004.

Block, D. L., Puerari, I., Elmegreen, B. G., and Bournaud, F. A Two-component Power Law Covering Nearly Four Orders of Magnitude in the Power Spectrum of Spitzer Far-infrared Emission from the Large Magellanic Cloud. *ApJ*, 718:L1–L6, 2010.

Blumenthal, G. R., Faber, S. M., Primack, J. R., and Rees, M. J. Formation of galaxies and large-scale structure with cold dark matter. *Nature*, 311:517–525, 1984.

Bois, M., et al. Formation of slowly rotating early-type galaxies via major mergers: a resolution study. *MNRAS*, 406:2405–2420, 2010.

Boissier, S., et al. Radial Variation of Attenuation and Star Formation in the Largest Late-Type Disks Observed with GALEX. *ApJS*, 173:524–537, 2007.

Bondi, H. and Hoyle, F. On the mechanism of accretion by stars. *MNRAS*, 104:273–+, 1944.

Bothwell, M. S., Kennicutt, R. C., and Lee, J. C. On the interstellar medium and star formation demographics of galaxies in the local universe. *MNRAS*, 400:154–167, 2009.

Bouché, N., et al. Dynamical Properties of z ˜ 2 Star-forming Galaxies and a Universal Star Formation Relation. *ApJ*, 671:303–309, 2007.

Bournaud, F. Star Formation and Structure Formation in Galaxy Interactions and Mergers. In B. Smith, J. Higdon, S. Higdon, & N. Bastian, editor, *Galaxy Wars: Stellar Populations and Star Formation in Interacting Galaxies*, volume 423 of *Astronomical Society of the Pacific Conference Series*, pages 177–+. 2010.

Bournaud, F. and Combes, F. Gas accretion on spiral galaxies: Bar formation and renewal. *A&A*, 392:83–102, 2002.

Bournaud, F., Combes, F., and Jog, C. J. Unequal-mass galaxy merger remnants: Spiral-like morphology but elliptical-like kinematics. *A&A*, 418:L27–L30, 2004.

Bournaud, F., Duc, P.-A., and Emsellem, E. High-resolution simulations of galaxy mergers: resolving globular cluster formation. *MNRAS*, 389:L8–L12, 2008.

Bournaud, F., Elmegreen, B. G., Teyssier, R., Block, D. L., and Puerari, I. ISM properties in hydrodynamic galaxy simulations: turbulence cascades, cloud formation, role of gravity and feedback. *MNRAS*, 409:1088–1099, 2010.

Bournaud, F., Jog, C. J., and Combes, F. Galaxy mergers with various mass ratios: Properties of remnants. *A&A*, 437:69–85, 2005.

Bournaud, F., Jog, C. J., and Combes, F. Multiple minor mergers: formation of elliptical galaxies and constraints for the growth of spiral disks. *A&A*, 476:1179–1190, 2007.

Bournaud, F., et al. Hydrodynamics of High-redshift Galaxy Collisions: From Gas-rich Disks to Dispersion-dominated Mergers and Compact Spheroids. *ApJ*, 730:4–+, 2011.

Brandl, B. R., et al. Deep Near-Infrared Imaging and Photometry of the Antennae Galaxies with WIRC. *ApJ*, 635:280–289, 2005.

Bushouse, H. A., Telesco, C. M., and Werner, M. W. The Distribution of Mid- and Far-Infrared Emission in 10 Interacting Galaxy Systems. *AJ*, 115:938–946, 1998.

Callegari, S., Kazantzidis, S., Mayer, L., Colpi, M., Bellovary, J. M., Quinn, T., and Wadsley, J. Growing Massive Black Hole Pairs in Minor Mergers of Disk Galaxies. *ApJ*, 729:85–+, 2011.

Callegari, S., Mayer, L., Kazantzidis, S., Colpi, M., Governato, F., Quinn, T., and Wadsley, J. Pairing of Supermassive Black Holes in Unequal-Mass Galaxy Mergers. *ApJ*, 696:L89–L92, 2009.

Cattaneo, A., et al. The role of black holes in galaxy formation and evolution. *Nature*, 460:213–219, 2009.

Chabrier, G. Galactic Stellar and Substellar Initial Mass Function. *PASP*, 115:763–795, 2003.

Chandrasekhar, S. Dynamical Friction. I. General Considerations: the Coefficient of Dynamical Friction. *ApJ*, 97:255–+, 1943.

Chandrasekhar, S. and Fermi, E. Problems of Gravitational Stability in the Presence of a Magnetic Field. *ApJ*, 118:116–+, 1953.

Chapon, D., Mayer, L., and Teyssier, R. Pairing and sinking of binary SMBHs in sub-pc resolution simulations of galaxy mergers. *Arxiv*, 1110.6086, 2011.

Clowe, D., Gonzalez, A., and Markevitch, M. Weak-Lensing Mass Reconstruction of the Interacting Cluster 1E 0657-558: Direct Evidence for the Existence of Dark Matter. *ApJ*, 604:596–603, 2004.

Colella, P. and Woodward, P. R. The Piecewise Parabolic Method (PPM) for Gas-Dynamical Simulations. *J. Comp. Phys.*, 54:174–201, 1984.

Colpi, M., Mayer, L., and Governato, F. Dynamical Friction and the Evolution of Satellites in Virialized Halos: The Theory of Linear Response. *ApJ*, 525:720–733, 1999.

Combes, F. Bar-driven Galaxy Evolution and Time-scales to Feed AGN. In F. Combes, G. A. Mamon, & V. Charmandaris, editor, *Dynamics of Galaxies: from the Early Universe to the Present*, volume 197 of *Astronomical Society of the Pacific Conference Series*, pages 15–+. 2000.

Corbelli, E. Dark matter and visible baryons in M33. *MNRAS*, 342:199–207, 2003.

Courant, C., Friedrichs, K., and Lewy, H. On the partial difference equations of mathematical physics. *IBM Journal*, pages 215–234, 1967.

Cox, T. J., Jonsson, P., Primack, J. R., and Somerville, R. S. Feedback in simulations of disc-galaxy major mergers. *MNRAS*, 373:1013–1038, 2006.

Cox, T. J., Jonsson, P., Somerville, R. S., Primack, J. R., and Dekel, A. The effect of galaxy mass ratio on merger-driven starbursts. *MNRAS*, 384:386–409, 2008.

Cuadra, J., Armitage, P. J., Alexander, R. D., and Begelman, M. C. Massive black hole binary mergers within subparsec scale gas discs. *MNRAS*, 393:1423–1432, 2009.

Cullen, H., Alexander, P., and Clemens, M. Gas in early-type galaxies: cross-fuelling in late-type-early-type pairs? *MNRAS*, 366:49–57, 2006.

Daddi, E., et al. Different Star Formation Laws for Disks Versus Starbursts at Low and High Redshifts. *ApJ*, 714:L118–L122, 2010a.

Daddi, E., et al. Very High Gas Fractions and Extended Gas Reservoirs in z = 1.5 Disk Galaxies. *ApJ*, 713:686–707, 2010b.

Davies, R. I., Müller Sánchez, F., Genzel, R., Tacconi, L. J., Hicks, E. K. S., Friedrich, S., and Sternberg, A. A Close Look at Star Formation around Active Galactic Nuclei. *ApJ*, 671:1388–1412, 2007.

de Avillez, M. A. and Breitschwerdt, D. The Generation and Dissipation of Interstellar Turbulence: Results from Large-Scale High-Resolution Simulations. *ApJ*, 665:L35–L38, 2007.

de Blok, W. J. G. The Core-Cusp Problem. *Advances in Astronomy*, 2010, 2010.

de Vaucouleurs, G. Recherches sur les Nebuleuses Extragalactiques. *Annales d'Astrophysique*, 11:247–+, 1948.

Dekel, A. and Birnboim, Y. Galaxy bimodality due to cold flows and shock heating. *MNRAS*, 368:2–20, 2006.

Dekel, A., et al. Cold streams in early massive hot haloes as the main mode of galaxy formation. *Nature*, 457:451–454, 2009.

Di Matteo, P., Bournaud, F., Martig, M., Combes, F., Melchior, A.-L., and Semelin, B. On the frequency, intensity, and duration of starburst episodes triggered by galaxy interactions and mergers. *A&A*, 492:31–49, 2008.

Diemand, J., Kuhlen, M., and Madau, P. Formation and Evolution of Galaxy Dark Matter Halos and Their Substructure. *ApJ*, 667:859–877, 2007.

Dobbs, C. L., Theis, C., Pringle, J. E., and Bate, M. R. Simulations of the grand design galaxy M51: a case study for analysing tidally induced spiral structure. *MNRAS*, 403:625–645, 2010.

Dotti, M., Colpi, M., and Haardt, F. Laser Interferometer Space Antenna double black holes: dynamics in gaseous nuclear discs. *MNRAS*, 367:103–112, 2006.

Dotti, M., Colpi, M., Haardt, F., and Mayer, L. Supermassive black hole binaries in gaseous and stellar circumnuclear discs: orbital dynamics and gas accretion. *MNRAS*, 379:956–962, 2007.

Downes, D. and Solomon, P. M. Rotating Nuclear Rings and Extreme Starbursts in Ultraluminous Galaxies. *ApJ*, 507:615–654, 1998.

Dubois, Y. and Teyssier, R. On the onset of galactic winds in quiescent star forming galaxies. *A&A*, 477:79–94, 2008.

Duc, P.-A., Brinks, E., Springel, V., Pichardo, B., Weilbacher, P., and Mirabel, I. F. Formation of a Tidal Dwarf Galaxy in the Interacting System Arp 245 (NGC 2992/93). *AJ*, 120:1238–1264, 2000.

Duc, P.-A., Brinks, E., Wink, J. E., and Mirabel, I. F. Gas segregation in the interacting system ARP 105. *A&A*, 326:537–553, 1997.

Einasto, J. Kinematics and dynamics of stellar systems. *Trudy Inst. Astroz. Alma-Ata*, 51:87, 1965.

Elbaz, D. and Cesarsky, C. J. A Fossil Record of Galaxy Encounters. *Science*, 300:270–274, 2003.

Elmegreen, B. G. Gravitational collapse in dust lanes and the appearance of spiral structure in galaxies. *ApJ*, 231:372–383, 1979.

Elmegreen, B. G. An effective Q parameter for two-fluid instabilities in spiral galaxies. *MNRAS*, 275:944–950, 1995.

Elmegreen, B. G. The Initial Stellar Mass Function from Random Sampling in a Turbulent Fractal Cloud. *ApJ*, 486:944–+, 1997.

Elmegreen, B. G. Star Formation from Galaxies to Globules. *ApJ*, 577:206–220, 2002.

Elmegreen, B. G., Kaufman, M., and Thomasson, M. An interaction model for the formation of dwarf galaxies and 10 exp 8 solar mass clouds in spiral disks. *ApJ*, 412:90–98, 1993.

Elmegreen, B. G. and Scalo, J. Interstellar Turbulence I: Observations and Processes. *ARA&A*, 42:211–273, 2004.

Elmegreen, B. G., et al. Hubble Space Telescope Observations of the Interacting Galaxies NGC 2207 and IC 2163. *AJ*, 120:630–644, 2000.

Elmegreen, D. M. and Elmegreen, B. G. Flocculent and grand design spiral structure in field, binary and group galaxies. *MNRAS*, 201:1021–1034, 1982.

Elmegreen, D. M., Kaufman, M., Brinks, E., Elmegreen, B. G., and Sundin, M. The Interaction between Spiral Galaxies IC 2163 and NGC 2207. I. Observations. *ApJ*, 453:100–+, 1995.

Emsellem, E., et al. The SAURON project - IX. A kinematic classification for early-type galaxies. *MNRAS*, 379:401–417, 2007.

Escala, A., Larson, R. B., Coppi, P. S., and Mardones, D. The Role of Gas in the Merging of Massive Black Holes in Galactic Nuclei. I. Black Hole Merging in a Spherical Gas Cloud. *ApJ*, 607(2):765–777, 2004.

Escala, A., Larson, R. B., Coppi, P. S., and Mardones, D. The Role of Gas in the Merging of Massive Black Holes in Galactic Nuclei. II. Black Hole Merging in a Nuclear Gas Disk. *ApJ*, 630:152–166, 2005.

Fabbiano, G., Zezas, A., and Murray, S. S. Chandra Observations of "The Antennae" Galaxies (NGC 4038/9). *ApJ*, 554:1035–1043, 2001.

Fakhouri, O., Ma, C.-P., and Boylan-Kolchin, M. The merger rates and mass assembly histories of dark matter haloes in the two Millennium simulations. *MNRAS*, 406:2267–2278, 2010.

Fall, S. M. and Efstathiou, G. Formation and rotation of disc galaxies with haloes. *MNRAS*, 193:189–206, 1980.

Ferrarese, L. and Ford, H. Supermassive Black Holes in Galactic Nuclei: Past, Present and Future Research. *Space Sci. Rev.*, 116:523–624, 2005.

Ferrarese, L. and Merritt, D. A Fundamental Relation between Supermassive Black Holes and Their Host Galaxies. *ApJ*, 539:L9–L12, 2000.

Ferrière, K. M. The interstellar environment of our galaxy. *Reviews of Modern Physics*, 73:1031–1066, 2001.

Förster Schreiber, N. M., et al. The SINS Survey: SINFONI Integral Field Spectroscopy of z ~ 2 Star-forming Galaxies. *ApJ*, 706:1364–1428, 2009.

Fromang, S., Hennebelle, P., and Teyssier, R. A high order Godunov scheme with constrained transport and adaptive mesh refinement for astrophysical magnetohydrodynamics. *A&A*, 457:371–384, 2006.

Fryxell, B., et al. FLASH: An Adaptive Mesh Hydrodynamics Code for Modeling Astrophysical Thermonuclear Flashes. *ApJS*, 131:273–334, 2000.

Galli, D. and Palla, F. The chemistry of the early Universe. *A&A*, 335:403–420, 1998.

Gao, Y. and Solomon, P. M. The Star Formation Rate and Dense Molecular Gas in Galaxies. *ApJ*, 606:271–290, 2004.

Genel, S., Genzel, R., Bouché, N., Naab, T., and Sternberg, A. The Halo Merger Rate in the Millennium Simulation and Implications for Observed Galaxy Merger Fractions. *ApJ*, 701:2002–2018, 2009.

Genzel, R., et al. A study of the gas-star formation relation over cosmic time. *MNRAS*, 407:2091–2108, 2010.

Gnat, O. and Sternberg, A. Time-dependent Ionization in Radiatively Cooling Gas. *ApJS*, 168:213–230, 2007.

Godunov, S. K. A Difference Scheme for Numerical Solution of Discontinuous Solution of Hydrodynamic Equations. *Math. Sbornik*, 47:271–306, 1959.

Goldreich, P. and Tremaine, S. The excitation of density waves at the Lindblad and corotation resonances by an external potential. *ApJ*, 233:857–871, 1979.

Goldreich, P. and Tremaine, S. The dynamics of planetary rings. *ARA&A*, 20:249–283, 1982.

Governato, F., et al. Bulgeless dwarf galaxies and dark matter cores from supernova-driven outflows. *Nature*, 463:203–206, 2010.

Guillet, T. *Baryons and structure formation*. Ph.D. thesis, 2010.

Guillet, T. and Teyssier, R. A simple multigrid scheme for solving the Poisson equation with arbitrary domain boundaries. *J. Comp. Phys.*, 230:4756–4771, 2011.

Haardt, F. and Madau, P. Radiative Transfer in a Clumpy Universe. II. The Ultraviolet Extragalactic Background. *ApJ*, 461:20–+, 1996.

Hernquist, L. An analytical model for spherical galaxies and bulges. *ApJ*, 356:359–364, 1990.

Hernquist, L. N-body realizations of compound galaxies. *ApJS*, 86:389–400, 1993.

Heyer, M. H. and Terebey, S. The Anatomy of the Perseus Spiral Arm: 12CO and IRAS Imaging Observations of the W3-W4-W5 Cloud Complex. *ApJ*, 502:265–+, 1998.

Hibbard, J. E., van der Hulst, J. M., Barnes, J. E., and Rich, R. M. High-Resolution H I Mapping of NGC 4038/39 ("The Antennae") and Its Tidal Dwarf Galaxy Candidates. *AJ*, 122:2969–2992, 2001.

Hibbard, J. E., et al. Ultraviolet Morphology and Star Formation in the Tidal Tails of NGC 4038/39. *ApJ*, 619:L87–L90, 2005.

Hilbert, D. Über die stetige Abbildung einer Linie auf ein Flachenstück. *Mathematische Annalen*, 38:459–460, 1891.

Hockney, R. W. and Eastwood, J. W. *Computer Simulation Using Particles*. 1981.

Hollenbach, D. and Salpeter, E. E. Surface Recombination of Hydrogen Molecules. *ApJ*, 163:155–+, 1971.

Hopkins, P. F., Hernquist, L., Cox, T. J., Di Matteo, T., Martini, P., Robertson, B., and Springel, V. Black Holes in Galaxy Mergers: Evolution of Quasars. *ApJ*, 630:705–715, 2005.

Hopkins, P. F., Somerville, R. S., Hernquist, L., Cox, T. J., Robertson, B., and Li, Y. The Relation between Quasar and Merging Galaxy Luminosity Functions and the Merger-driven Star Formation History of the Universe. *ApJ*, 652:864–888, 2006.

Hummel, E. and van der Hulst, J. M. NGC 4038/39: Interacting spiral galaxies with enhanced extended radio emission. *A&A*, 155:151–160, 1986.

Jaffe, A. H. and Backer, D. C. Gravitational Waves Probe the Coalescence Rate of Massive Black Hole Binaries. *ApJ*, 583:616–631, 2003.

Jeans, J. H. The Stability of a Spherical Nebula. *Royal Society of London Philosophical Transactions Series A*, 199:1–53, 1902.

Jesseit, R., Cappellari, M., Naab, T., Emsellem, E., and Burkert, A. Specific angular momentum of disc merger remnants and the λ_R-parameter. *MNRAS*, 397:1202–1214, 2009.

Jog, C. J. Local stability criterion for stars and gas in a galactic disc. *MNRAS*, 278:209–218, 1996.

Jog, C. J. and Solomon, P. M. A galactic disk as a two-fluid system - Consequences for the critical stellar velocity dispersion and the formation of condensations in the gas. *ApJ*, 276:127–134, 1984.

Jogee, S., et al. History of Galaxy Interactions and Their Impact on Star Formation Over the Last 7 Gyr from GEMS. *ApJ*, 697:1971–1992, 2009.

Karl, S. J., Naab, T., Johansson, P. H., Kotarba, H., Boily, C. M., Renaud, F., and Theis, C. One Moment in Time : Modeling Star Formation in the Antennae. *ApJ*, 715:L88–L93, 2010.

Karl, S. J., Naab, T., Johansson, P. H., Theis, C., and Boily, C. M. Towards an accurate model for the Antennae galaxies. *Astronomische Nachrichten*, 329:1042–+, 2008.

Katz, N. Dissipational galaxy formation. II - Effects of star formation. *ApJ*, 391:502–517, 1992.

Katz, N., Weinberg, D. H., and Hernquist, L. Cosmological Simulations with TreeSPH. *ApJS*, 105:19–+, 1996.

Kautsch, S. J., Grebel, E. K., Barazza, F. D., and Gallagher, J. S., III. A catalog of edge-on disk galaxies. From galaxies with a bulge to superthin galaxies. *A&A*, 445:765–778, 2006.

Kazantzidis, S., et al. The Fate of Supermassive Black Holes and the Evolution of the $M_{\mathrm{BH}} - \sigma$ Relation in Merging Galaxies: The Effect of Gaseous Dissipation. *ApJ*, 623:L67–L70, 2005.

Kennicutt, R. C., Jr. The star formation law in galactic disks. *ApJ*, 344:685–703, 1989.

Kennicutt, R. C., Jr. The Global Schmidt Law in Star-forming Galaxies. *ApJ*, 498:541–+, 1998.

Kereš, D., Katz, N., Fardal, M., Davé, R., and Weinberg, D. H. Galaxies in a simulated ΛCDM Universe - I. Cold mode and hot cores. *MNRAS*, 395:160–179, 2009.

Kereš, D., Katz, N., Weinberg, D. H., and Davé, R. How do galaxies get their gas? *MNRAS*, 363:2–28, 2005.

Khan, F. M., Just, A., and Merritt, D. Efficient Merger of Binary Supermassive Black Holes in Merging Galaxies. *ApJ*, 732:89–+, 2011.

Khokhlov, A. Fully Threaded Tree Algorithms for Adaptive Refinement Fluid Dynamics Simulations. *J. Comp. Phys.*, 143:519–543, 1998.

Kim, J.-h., Wise, J. H., and Abel, T. Galaxy Mergers with Adaptive Mesh Refinement: Star Formation and Hot Gas Outflow. *ApJ*, 694:L123–L127, 2009.

Klypin, A. A., Trujillo-Gomez, S., and Primack, J. Dark Matter Halos in the Standard Cosmological Model: Results from the Bolshoi Simulation. *ApJ*, 740:102–+, 2011.

Knierman, K. A. Tidal Tales of Minor Mergers: Star Formation in the Tidal Debris of Minor Mergers. In B. Smith, J. Higdon, S. Higdon, & N. Bastian, editor, *Galaxy Wars: Stellar Populations and Star Formation in Interacting Galaxies*, volume 423 of *Astronomical Society of the Pacific Conference Series*, pages 342–+. 2010.

Kormendy, J. and Bender, R. A Proposed Revision of the Hubble Sequence for Elliptical Galaxies. *ApJ*, 464:L119+, 1996.

Kravtsov, A. V., Klypin, A. A., and Khokhlov, A. M. Adaptive Refinement Tree: A new high-resolution N-body code for cosmological simulations. *ApJS*, 111:73–+, 1997.

Kroupa, P. On the variation of the initial mass function. *MNRAS*, 322:231–246, 2001.

Kuhlen, M., Diemand, J., Madau, P., and Zemp, M. The Via Lactea INCITE simulation: galactic dark matter substructure at high resolution. *Journal of Physics Conference Series*, 125(1):012008–+, 2008.

Labadens, M., Chapon, D., Pomarede, D., and Teyssier, R. PyMSES, a RAMSES data analysis toolbox : I. I/O and Visualization performance tests. *in prep.*, 2011.

Li, Y., Mac Low, M.-M., and Klessen, R. S. Formation of Globular Clusters in Galaxy Mergers. *ApJ*, 614:L29–L32, 2004.

Lin, C. C. and Shu, F. H. On the Spiral Structure of Disk Galaxies. *ApJ*, 140:646–+, 1964.

Lynden-Bell, D. Statistical mechanics of violent relaxation in stellar systems. *MNRAS*, 136:101–+, 1967.

Mac Low, M.-M. and Klessen, R. S. Control of star formation by supersonic turbulence. *Reviews of Modern Physics*, 76:125–194, 2004.

Machacek, M. E., Bryan, G. L., and Abel, T. Simulations of Pregalactic Structure Formation with Radiative Feedback. *ApJ*, 548:509–521, 2001.

Maller, A. H. and Dekel, A. Towards a resolution of the galactic spin crisis: mergers, feedback and spin segregation. *MNRAS*, 335:487–498, 2002.

Maller, A. H., Katz, N., Kereš, D., Davé, R., and Weinberg, D. H. Galaxy Merger Statistics and Inferred Bulge-to-Disk Ratios in Cosmological SPH Simulations. *ApJ*, 647:763–772, 2006.

Mamon, G. A. Are cluster ellipticals the products of mergers? *ApJ*, 401:L3–L6, 1992.

Manthey, E., Hüttemeister, S., Aalto, S., Horellou, C., and Bjerkeli, P. Stars and gas in the Medusa merger. *A&A*, 490:975–987, 2008.

Mayer, L. and Kazantzidis, S. Formation of Nuclear Disks and Supermassive Black Hole Binaries in Galaxy Mergers. *Mem. Soc. Astron. Italiana*, 79:1284–+, 2008.

Mayer, L., Kazantzidis, S., Madau, P., Colpi, M., Quinn, T., and Wadsley, J. Rapid Formation of Supermassive Black Hole Binaries in Galaxy Mergers with Gas. *Science*, 316:1874–, 2007.

McCray, R. and Snow, T. P., Jr. The violent interstellar medium. *ARA&A*, 17:213–240, 1979.

McKee, C. F. and Ostriker, E. C. Theory of Star Formation. *ARA&A*, 45:565–687, 2007.

McKee, C. F. and Ostriker, J. P. A theory of the interstellar medium - Three components regulated by supernova explosions in an inhomogeneous substrate. *ApJ*, 218:148–169, 1977.

Mengel, S., Lehnert, M. D., Thatte, N., and Genzel, R. Star-formation in NGC 4038/4039 from broad and narrow band photometry: cluster destruction? *A&A*, 443:41–60, 2005.

Mihos, J. C., Bothun, G. D., and Richstone, D. O. Modeling the Spatial Distribution of Star Formation in Interacting Disk Galaxies. *ApJ*, 418:82–+, 1993.

Mihos, J. C. and Hernquist, L. Gasdynamics and Starbursts in Major Mergers. *ApJ*, 464:641–+, 1996.

Milosavljević, M. and Merritt, D. Formation of Galactic Nuclei. *ApJ*, 563:34–62, 2001.

Moore, G. E. Cramming More Components Onto Integrated Circuits. *Electronics*, 38, 1965.

Mouschovias, T. C. Nonhomologous contraction and equilibria of self-gravitating, magnetic interstellar clouds embedded in an intercloud medium: Star formation. II - Results. *ApJ*, 207:141–158, 1976.

Naab, T. and Burkert, A. Statistical Properties of Collisionless Equal- and Unequal-Mass Merger Remnants of Disk Galaxies. *ApJ*, 597:893–906, 2003.

Naab, T., Johansson, P. H., and Ostriker, J. P. Minor Mergers and the Size Evolution of Elliptical Galaxies. *ApJ*, 699:L178–L182, 2009.

Naab, T., Johansson, P. H., Ostriker, J. P., and Efstathiou, G. Formation of Early-Type Galaxies from Cosmological Initial Conditions. *ApJ*, 658:710–720, 2007.

Navarro, J. F., Frenk, C. S., and White, S. D. M. A Universal Density Profile from Hierarchical Clustering. *ApJ*, 490:493–+, 1997.

Navarro, J. F., et al. The inner structure of ΛCDM haloes - III. Universality and asymptotic slopes. *MNRAS*, 349:1039–1051, 2004.

Navarro, J. F., et al. The diversity and similarity of simulated cold dark matter haloes. *MNRAS*, 402:21–34, 2010.

Nesvadba, N. P. H., Lehnert, M. D., De Breuck, C., Gilbert, A. M., and van Breugel, W. Evidence for powerful AGN winds at high redshift: dynamics of galactic outflows in radio galaxies during the "Quasar Era". *A&A*, 491:407–424, 2008.

Ocvirk, P., Pichon, C., and Teyssier, R. Bimodal gas accretion in the Horizon-MareNostrum galaxy formation simulation. *MNRAS*, 390:1326–1338, 2008.

Oh, S. H., Kim, W.-T., Lee, H. M., and Kim, J. Physical Properties of Tidal Features in Interacting Disk Galaxies. *ApJ*, 683:94–113, 2008.

O'Shea, B. W., Bryan, G., Bordner, J., Norman, M. L., Abel, T., Harkness, R., and Kritsuk, A. Introducing Enzo, an AMR Cosmology Application. *ArXiv*, 2004.

Ostriker, E. C. Dynamical Friction in a Gaseous Medium. *ApJ*, 513(1):252–258, 1999.

Ostriker, J. The Equilibrium of Polytropic and Isothermal Cylinders. *ApJ*, 140:1056–+, 1964.

Padoan, P., Nordlund, Å., Kritsuk, A. G., Norman, M. L., and Li, P. S. Two Regimes of Turbulent Fragmentation and the Stellar Initial Mass Function from Primordial to Present-Day Star Formation. *ApJ*, 661:972–981, 2007.

Patton, D. R., et al. Dynamically Close Galaxy Pairs and Merger Rate Evolution in the CNOC2 Redshift Survey. *ApJ*, 565:208–222, 2002.

Peano, G. Sur une courbe, qui remplit une aire plane. *Mathematische Annalen*, 36:157–160, 1890.

Perlmutter, S., et al. Measurements of Omega and Lambda from 42 High-Redshift Supernovae. *ApJ*, 517:565–586, 1999.

Powell, L. C., Bournaud, F., Chapon, D., Devriendt, J., Slyz, A., and Teyssier, R. Galactic star formation in parsec-scale resolution simulations. In J. Alves, B. G. Elmegreen, J. M. Girart, & V. Trimble, editor, *IAU Symposium*, volume 270 of *IAU Symposium*, pages 487–490. 2011a.

Powell, L. C., Bournaud, F., Chapon, D., Devriendt, J., Slyz, A., and Teyssier, R. The impact of ISM turbulence, clustered star formation and feedback on galaxy mass assembly through cold flows and mergers. *ArXiv*, 2011b.

Preto, M. and Amaro-Seoane, P. On Strong Mass Segregation Around a Massive Black Hole: Implications for Lower-Frequency Gravitational-Wave Astrophysics. *ApJ*, 708:L42–L46, 2010.

Rafikov, R. R. The local axisymmetric instability criterion in a thin, rotating, multicomponent disc. *MNRAS*, 323:445–452, 2001.

Rasera, Y. and Teyssier, R. The history of the baryon budget. Cosmic logistics in a hierarchical universe. *A&A*, 445:1–27, 2006.

Reeves, J. N., O'Brien, P. T., and Ward, M. J. A Massive X-Ray Outflow from the Quasar PDS 456. *ApJ*, 593:L65–L68, 2003.

Renaud, F. *Dynamics of the Tidal Fields and Formation of Star Clusters in Galaxy Mergers*. Ph.D. thesis, PhD Thesis, 281 pages, 121 figures, 2010, 2010.

Renaud, F., Boily, C. M., Fleck, J., Naab, T., and Theis, C. Star cluster survival and compressive tides in Antennae-like mergers. *MNRAS*, 391:L98–L102, 2008.

Riess, A. G., et al. Observational Evidence from Supernovae for an Accelerating Universe and a Cosmological Constant. *AJ*, 116:1009–1038, 1998.

Robaina, A. R., et al. Less Than 10 Percent of Star Formation in z ˜ 0.6 Massive Galaxies is Triggered by Major Interactions. *ApJ*, 704:324–340, 2009.

Robertson, B. E. and Kravtsov, A. V. Molecular Hydrogen and Global Star Formation Relations in Galaxies. *ApJ*, 680:1083–1111, 2008.

Rubin, V. C., Ford, W. K., Jr., and D'Odorico, S. Emission-Line Intensities and Radial Velocities in the Interacting Galaxies NGC 4038-4039. *ApJ*, 160:801–+, 1970.

Rubin, V. C., Thonnard, N., and Ford, W. K., Jr. Extended rotation curves of high-luminosity spiral galaxies. IV - Systematic dynamical properties, SA through SC. *ApJ*, 225:L107–L111, 1978.

Ruffert, M. Three-dimensional hydrodynamic Bondi-Hoyle accretion. V. Specific heat ratio 1.01, nearly isothermal flow. *A&A*, 311:817–832, 1996.

Saitoh, T. R., Daisaka, H., Kokubo, E., Makino, J., Okamoto, T., Tomisaka, K., Wada, K., and Yoshida, N. Toward First-Principle Simulations of Galaxy Formation: II. Shock-Induced Starburst at a Collision Interface during the First Encounter of Interacting Galaxies. *PASJ*, 61:481–, 2009.

Salpeter, E. E. The Luminosity Function and Stellar Evolution. *ApJ*, 121:161–+, 1955.

Sánchez-Salcedo, F. J. and Brandenburg, A. Dynamical friction of bodies orbiting in a gaseous sphere. *MNRAS*, 322:67–78, 2001.

Sanders, D. B. and Mirabel, I. F. Luminous Infrared Galaxies. *ARA&A*, 34:749–+, 1996.

Saviane, I., Hibbard, J. E., and Rich, R. M. The Stellar Content of the Southern Tail of NGC 4038/4039 and a Revised Distance. *AJ*, 127:660–678, 2004.

Schaye, J. and Dalla Vecchia, C. On the relation between the Schmidt and Kennicutt-Schmidt star formation laws and its implications for numerical simulations. *MNRAS*, 383:1210–1222, 2008.

Schmidt, M. The Rate of Star Formation. *ApJ*, 129:243–+, 1959.

Schweizer, F., et al. a New Distance to the Antennae Galaxies (ngc 4038/39) Based on the Type ia Supernova 2007sr. *AJ*, 136:1482–1489, 2008.

Scoville, N. Z. and Solomon, P. M. Radiative Transfer, Excitation, and Cooling of Molecular Emission Lines (co and Cs). *ApJ*, 187:L67+, 1974.

Sesana, A., Haardt, F., Madau, P., and Volonteri, M. The Gravitational Wave Signal from Massive Black Hole Binaries and Its Contribution to the LISA Data Stream. *ApJ*, 623:23–30, 2005.

Sesana, A., Volonteri, M., and Haardt, F. LISA detection of massive black hole binaries: imprint of seed populations and extreme recoils. *Classical and Quantum Gravity*, 26(9):094033–+, 2009.

Shull, J. M. and Beckwith, S. Interstellar molecular hydrogen. *ARA&A*, 20:163–190, 1982.

Spaans, M. and Silk, J. The Polytropic Equation of State of Interstellar Gas Clouds. *ApJ*, 538(1):115, 2000.

Spergel, D. N., et al. Three-Year Wilkinson Microwave Anisotropy Probe (WMAP) Observations: Implications for Cosmology. *ApJS*, 170:377–408, 2007.

Spitzer, L., Jr. Theories of the hot interstellar gas. *ARA&A*, 28:71–101, 1990.

Springel, V. The cosmological simulation code GADGET-2. *MNRAS*, 364:1105–1134, 2005.

Springel, V. E pur si muove: Galilean-invariant cosmological hydrodynamical simulations on a moving mesh. *MNRAS*, 401:791–851, 2010.

Springel, V., Frenk, C. S., and White, S. D. M. The large-scale structure of the Universe. *Nature*, 440:1137–1144, 2006.

Springel, V. and Hernquist, L. Cosmological smoothed particle hydrodynamics simulations: a hybrid multiphase model for star formation. *MNRAS*, 339:289–311, 2003.

Springel, V., et al. Simulations of the formation, evolution and clustering of galaxies and quasars. *Nature*, 435:629–636, 2005.

Springel, V., et al. The Aquarius Project: the subhaloes of galactic haloes. *MNRAS*, 391:1685–1711, 2008.

Stadel, J., Potter, D., Moore, B., Diemand, J., Madau, P., Zemp, M., Kuhlen, M., and Quilis, V. Quantifying the heart of darkness with GHALO - a multibillion particle simulation of a galactic halo. *MNRAS*, 398:L21–L25, 2009.

Stewart, K. R., Bullock, J. S., Wechsler, R. H., Maller, A. H., and Zentner, A. R. Merger Histories of Galaxy Halos and Implications for Disk Survival. *ApJ*, 683:597–610, 2008.

Struck, C., Kaufman, M., Brinks, E., Thomasson, M., Elmegreen, B. G., and Elmegreen, D. M. The grazing encounter between IC 2163 and NGC 2207: pushing the limits of observational modelling. *MNRAS*, 364:69–90, 2005.

Tacconi, L. J., et al. High molecular gas fractions in normal massive star-forming galaxies in the young Universe. *Nature*, 463:781–784, 2010.

Tasker, E. J. and Bryan, G. L. Simulating Star Formation and Feedback in Galactic Disk Models. *ApJ*, 641:878–890, 2006.

Tasker, E. J. and Tan, J. C. Star Formation in Disk Galaxies. I. Formation and Evolution of Giant Molecular Clouds via Gravitational Instability and Cloud Collisions. *ApJ*, 700:358–375, 2009.

Teyssier, R. Cosmological hydrodynamics with adaptive mesh refinement. a new high resolution code called ramses. *A&A*, 385:337–364, 2002.

Teyssier, R., Chapon, D., and Bournaud, F. The Driving Mechanism of Starbursts in Galaxy Mergers. *ApJ*, 720:L149–L154, 2010.

Teyssier, R., et al. Full-sky weak-lensing simulation with 70 billion particles. *A&A*, 497:335–341, 2009.

Toomre, A. On the gravitational stability of a disk of stars. *ApJ*, 139:1217–1238, 1964.

Toomre, A. Mergers and Some Consequences. In B. M. Tinsley & R. B. Larson, editor, *Evolution of Galaxies and Stellar Populations*, pages 401–+. 1977.

Toomre, A. What amplifies the spirals. In S. M. Fall & D. Lynden-Bell, editor, *Structure and Evolution of Normal Galaxies*, pages 111–136. 1981.

Toomre, A. and Toomre, J. Galactic Bridges and Tails. *ApJ*, 178:623–666, 1972.

Toth, G. and Ostriker, J. P. Galactic disks, infall, and the global value of Omega. *ApJ*, 389:5–26, 1992.

Tremaine, S., et al. The Slope of the Black Hole Mass versus Velocity Dispersion Correlation. *ApJ*, 574:740–753, 2002.

Truelove, J. K., Klein, R. I., McKee, C. F., Holliman, J. H., II, Howell, L. H., and Greenough, J. A. The Jeans Condition: A New Constraint on Spatial Resolution in Simulations of Isothermal Self-gravitational Hydrodynamics. *ApJ*, 489:L179+, 1997.

Turk, M. J., Smith, B. D., Oishi, J. S., Skory, S., Skillman, S. W., Abel, T., and Norman, M. L. yt: A Multi-code Analysis Toolkit for Astrophysical Simulation Data. *ApJS*, 192:9–+, 2011.

van Leer, B. Towards the ultimate conservative difference scheme. V - A second-order sequel to Godunov's method. *J. Comp. Phys.*, 32:101–136, 1979.

Vandervoort, P. O. Resonant Stellar Orbits in Spiral Galaxies. II. a General Epicyclic Theory. *ApJ*, 201:50–62, 1975.

Vecchio, A. LISA observations of rapidly spinning massive black hole binary systems. *Phys. Rev. D*, 70(4):042001–+, 2004.

Volonteri, M., Haardt, F., and Gültekin, K. Compact massive objects in Virgo galaxies: the black hole population. *MNRAS*, 384:1387–1392, 2008.

Wada, K. and Norman, C. A. Numerical Models of the Multiphase Interstellar Matter with Stellar Energy Feedback on a Galactic Scale. *ApJ*, 547:172–186, 2001.

Wada, K. and Norman, C. A. Density Structure of the Interstellar Medium and the Star Formation Rate in Galactic Disks. *ApJ*, 660:276, 2007.

Wadsley, J. W., Stadel, J., and Quinn, T. Gasoline: a flexible, parallel implementation of TreeSPH. *New Astronomy*, 9:137–158, 2004.

Wang, Z., et al. The Off-Nuclear Starbursts in NGC 4038/4039 (The Antennae Galaxies). *ApJS*, 154:193–198, 2004.

Weidner, C., Kroupa, P., and Larsen, S. S. Implications for the formation of star clusters from extragalactic star formation rates. *MNRAS*, 350:1503–1510, 2004.

Wetzstein, M., Naab, T., and Burkert, A. Do dwarf galaxies form in tidal tails? *MNRAS*, 375:805–820, 2007.

White, S. D. M. Angular momentum growth in protogalaxies. *ApJ*, 286:38–41, 1984.

White, S. D. M. and Rees, M. J. Core condensation in heavy halos - A two-stage theory for galaxy formation and clustering. *MNRAS*, 183:341–358, 1978.

Whitmore, B. C., Chandar, R., and Fall, S. M. Star Cluster Demographics. I. A General Framework and Application to the Antennae Galaxies. *AJ*, 133:1067–1084, 2007.

Whitmore, B. C. and Schweizer, F. Hubble space telescope observations of young star clusters in NGC-4038/4039, 'the antennae' galaxies. *AJ*, 109:960–980, 1995.

Whitmore, B. C., Zhang, Q., Leitherer, C., Fall, S. M., Schweizer, F., and Miller, B. W. The Luminosity Function of Young Star Clusters in "the Antennae" Galaxies (NGC 4038-4039). *AJ*, 118:1551–1576, 1999.

Wolfire, M. G., Hollenbach, D., McKee, C. F., Tielens, A. G. G. M., and Bakes, E. L. O. The neutral atomic phases of the interstellar medium. *ApJ*, 443:152–168, 1995.

Yang, C.-C., Gruendl, R. A., Chu, Y.-H., Mac Low, M.-M., and Fukui, Y. Large-Scale Gravitational Instability and Star Formation in the Large Magellanic Cloud. *ApJ*, 671:374–379, 2007.

Yepes, G., Kates, R., Khokhlov, A., and Klypin, A. Hydrodynamical simulations of galaxy formation: effects of supernova feedback. *MNRAS*, 284:235–256, 1997.

Zezas, A. and Fabbiano, G. Chandra Observations of "The Antennae" Galaxies (NGC 4038/4039). IV. The X-Ray Source Luminosity Function and the Nature of Ultraluminous X-Ray Sources. *ApJ*, 577:726–737, 2002.

Zhang, Q., Fall, S. M., and Whitmore, B. C. A Multiwavelength Study of the Young Star Clusters and Interstellar Medium in the Antennae Galaxies. *ApJ*, 561:727–750, 2001.

Ziegler, U. Self-gravitational adaptive mesh magnetohydrodynamics with the NIRVANA code. *A&A*, 435:385–395, 2005.

Zwicky, F. Die Rotverschiebung von extragalaktischen Nebeln. *Helvetica Physica Acta*, 6:110–127, 1933.